Cell

Enhanced safety and efficacy of protease-regulated CAR-T cell receptors

Graphical abstract

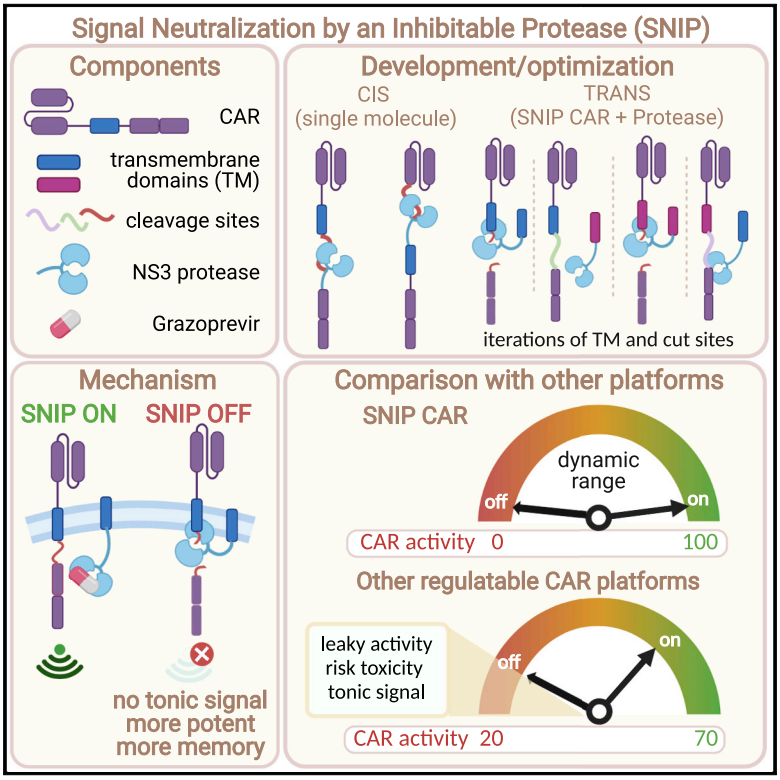

Highlights

- SNIP CARs are tightly regulated by an FDA-approved protease inhibitor
- SNIP CARs provide a safety switch and are more potent than constitutive CARs
- PK modulation of drug levels enhances CAR potency through cyclic rest
- Reduced drug dosing can prevent on-target off-tumor toxicity

Authors

Louai Labanieh, Robbie G. Majzner, Dorota Klysz, ..., Michael Z. Lin, Jennifer R. Cochran, Crystal L. Mackall

Correspondence

cmackall@stanford.edu

In brief

SNIP is a drug-regulated CAR platform that utilizes an FDA-approved small molecule to enable remote control and a generalizable molecular architecture that does not perturb CAR function.

Labanieh et al., 2022, Cell *185*, 1–19
May 12, 2022 © 2022 The Authors. Published by Elsevier Inc.
https://doi.org/10.1016/j.cell.2022.03.041

CellPress

Please cite this article in press as: Labanieh et al., Enhanced safety and efficacy of protease-regulated CAR-T cell receptors, Cell (2022), https://doi.org/10.1016/j.cell.2022.03.041

Cell

CellPress
OPEN ACCESS

Article

Enhanced safety and efficacy of protease-regulated CAR-T cell receptors

Louai Labanieh,[1,2] Robbie G. Majzner,[2,3,4] Dorota Klysz,[2] Elena Sotillo,[2] Chris J. Fisher,[2] José G. Vilches-Moure,[5] Kaithlen Zen B. Pacheco,[2] Meena Malipatlolla,[2] Peng Xu,[2] Jessica H. Hui,[2] Tara Murty,[2,6,7] Johanna Theruvath,[2,3] Nishant Mehta,[1] Sean A. Yamada-Hunter,[2] Evan W. Weber,[2,15,16] Sabine Heitzeneder,[2] Kevin R. Parker,[8] Ansuman T. Satpathy,[9] Howard Y. Chang,[8,10] Michael Z. Lin,[1,11,12] Jennifer R. Cochran,[1,4,13] and Crystal L. Mackall[2,3,4,14,17,*]

[1]Department of Bioengineering, Stanford University, Stanford, CA 94305, USA
[2]Center for Cancer Cell Therapy, Stanford Cancer Institute, Stanford University School of Medicine, Stanford, CA 94305, USA
[3]Department of Pediatrics, Stanford University School of Medicine, Stanford, CA 94305, USA
[4]Stanford Cancer Institute, Stanford University School of Medicine, Stanford, CA 94305, USA
[5]Department of Comparative Medicine, School of Medicine, Stanford University, Stanford, CA 94305, USA
[6]Medical Scientist Training Program, Stanford University School of Medicine, Stanford, CA 94305, USA
[7]Biophysics Program, Stanford University School of Medicine, Stanford, CA 94305, USA
[8]Center for Personal Dynamic Regulomes, Stanford University School of Medicine, Stanford, CA 94305, USA
[9]Department of Pathology, Stanford University, Stanford, CA 94305, USA
[10]Howard Hughes Medical Institute, Stanford University, Stanford, CA 94305, USA
[11]Department of Neurobiology, Stanford University, Stanford, CA 94305, USA
[12]Department of Chemical and Systems Biology, Stanford University School of Medicine, Stanford, CA 94305, USA
[13]Department of Chemical Engineering, Stanford University, Stanford, CA 94305, USA
[14]Department of Medicine, Stanford University School of Medicine, Stanford, CA 94305, USA
[15]Present address: Center for Childhood Cancer Research, The Children's Hospital of Philadelphia, Philadelphia, PA 19104, USA
[16]Present address: Department of Pediatrics, University of Pennsylvania, Philadelphia, PA 19104, USA
[17]Lead contact
*Correspondence: cmackall@stanford.edu
https://doi.org/10.1016/j.cell.2022.03.041

SUMMARY

Regulatable CAR platforms could circumvent toxicities associated with CAR-T therapy, but existing systems have shortcomings including leakiness and attenuated activity. Here, we present SNIP CARs, a protease-based platform for regulating CAR activity using an FDA-approved small molecule. Design iterations yielded CAR-T cells that manifest full functional capacity with drug and no leaky activity in the absence of drug. In numerous models, SNIP CAR-T cells were more potent than constitutive CAR-T cells and showed diminished T cell exhaustion and greater stemness. In a ROR1-based CAR lethality model, drug cessation following toxicity onset reversed toxicity, thereby credentialing the platform as a safety switch. In the same model, reduced drug dosing opened a therapeutic window that resulted in tumor eradication in the absence of toxicity. SNIP CARs enable remote tuning of CAR activity, which provides solutions to safety and efficacy barriers that are currently limiting progress in using CAR-T cells to treat solid tumors.

INTRODUCTION

Chimeric antigen receptor (CAR) T cell therapy has demonstrated unprecedented therapeutic activity in relapsed and refractory B cell malignancies (Ali et al., 2016; Brudno et al., 2018; Fry et al., 2018; Jacoby et al., 2019; Lee et al., 2015; Majzner and Mackall, 2019; Maude et al., 2018; Neelapu et al., 2017a; Raje et al., 2019; Schuster et al., 2017, 2019; Wang et al., 2020). Despite these promising results, therapy-related severe adverse events such as cytokine release syndrome (CRS) and neurotoxicity are common and can be fatal (Benjamin et al., 2020; Brudno and Kochenderfer, 2019; Gust et al., 2017; Neelapu et al., 2018; Sheth and Gauthier, 2020; Schmidts et al., 2021). Moreover, CAR-T cell therapy in solid tumors has yielded only limited success. This relates in part to challenges posed by a lack of tumor-specific cell surface antigens and shared expression of candidate solid tumor targets on vital normal tissues, which heightens the risk of on-target off-tumor toxicity (Gross and Eshhar, 2016; Majzner and Mackall, 2019; Neelapu et al., 2018; Schmidts et al., 2021), as already observed with CAIX (Lamers et al., 2013) and CEACAM5-targeting CARs (Thistlethwaite et al., 2017). Numerous strategies are being investigated to bolster the potency of CAR-T cells for solid tumors (Fucà et al., 2020; Hong et al., 2020; Labanieh et al., 2018; Schmidts and Maus, 2018),

This is an open access article under the CC BY-NC-ND license (http://creativecommons.org/licenses/by-nc-nd/4.0/).

Please cite this article in press as: Labanieh et al., Enhanced safety and efficacy of protease-regulated CAR-T cell receptors, Cell (2022), https://doi.org/10.1016/j.cell.2022.03.041

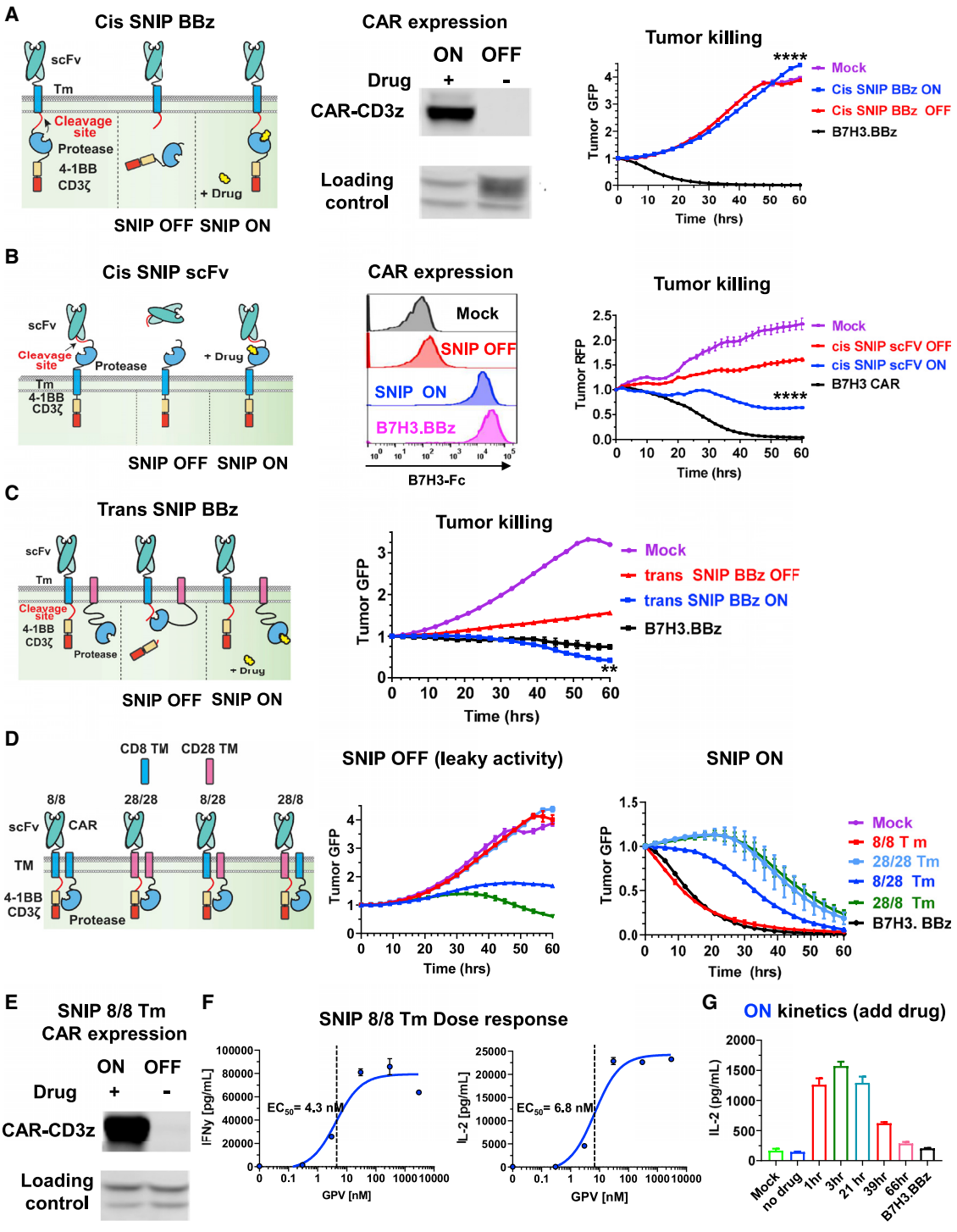

Figure 1. The optimized SNIP design, *trans* SNIP BBz, confers robust control over CAR-T cytotoxicity

(A) Schematic illustration of the *cis* SNIP BBz system (left). CAR-CD3ζ immunoblots of protein lysates from anti-B7H3 *cis* SNIP BBz CAR-T cells ± 3 μM GPV (middle). Cytotoxicity of day 10 anti-B7H3 *cis* SNIP BBz CAR-T cells (right).

(B) Schematic illustration of the *cis* SNIP scFv system (left), flow cytometry of surface B7H3 CAR (middle), and tumor killing (right).

(C) Schematic illustration of the *trans* SNIP BBz system (left) and tumor killing (right).

(D) Schematic of various combinations of CD8α and CD28 Tm for the CAR and protease modules (left). Tumor killing in the absence (SNIP OFF, middle) or presence (SNIP ON, right) of GPV.

(E) CD3ζ immunoblots of the 8/8 Tm configuration.

(legend continued on next page)

Please cite this article in press as: Labanieh et al., Enhanced safety and efficacy of protease-regulated CAR-T cell receptors, Cell (2022), https://doi.org/10.1016/j.cell.2022.03.041

including increasing sensitivity to antigen (Majzner et al., 2020), inducing exhaustion resistance (Lynn et al., 2019), disrupting inhibitory genes (Jung et al., 2018; Ren and Zhao, 2017; Ren et al., 2017; Zhang et al., 2017b), and providing signals that amplify expansion and/or T cell persistence (Adachi et al., 2018; DeRenzo and Gottschalk, 2019; Hurton et al., 2016; Kagoya et al., 2018; Shum et al., 2017; Wang et al., 2019). Although these strategies may prove useful in amplifying the antitumor response, they may also increase risk of toxicity, highlighting the need for next-generation CAR systems with built-in safety features. Suicide switches may diminish risk but abrogate the potential for antitumor effects, and in some settings, they are inefficient (Diaconu et al., 2017; Murty et al., 2020; Paszkiewicz et al., 2016; Philip et al., 2014; Di Stasi et al., 2011).

CAR-T cells are self-amplifying and demonstrate high patient-to-patient variability in expansion and activity (Milone and Bhoj, 2018; Mueller et al., 2018; Stein et al., 2019). Therefore, constitutive CAR-T cell platforms provide limited opportunity to control dosing and activity of these potent immune effectors following the onset of toxicity. Traditional drugs such as small molecules have well-defined pharmacokinetics (PKs), and dosing can be individually tuned to provide a therapeutic window (TW). Drug-regulatable CAR platforms, whereby the activity of CAR-T cells is conditional and can be controlled remotely by an administered drug, provide a potentially attractive safety feature for controlling CAR-T functionality without permanently ablating the cells. Such platforms could also potentially allow tuning of the activity of the CAR-T cells to avoid toxicity. However, previously reported drug-regulatable systems have been limited by poor dynamic range, residual ''leaky'' activity in the OFF state, reduced expression of CAR on the cell surface, the use of immunosuppressive drugs for CAR control, and/or diminished potency compared with constitutive CARs (Giordano-Attianese et al., 2020; Jan et al., 2021; Juillerat et al., 2019; Leung et al., 2019; Richman et al., 2020; Sakemura et al., 2016; Salzer et al., 2020; Wu et al., 2015; Zajc et al., 2020).

Here, we report the engineering and development of a high-performance drug-regulatable system termed signal neutralization by an inhibitable protease (SNIP) that is regulated by an FDA-approved small molecule with favorable PK in humans. The platform has no leaky activity and outperforms constitutive CARs in multiple orthotopic solid tumor models. We show that SNIP CAR-T cells provide a reliable safety switch since lethal toxicity can be prevented by stopping drug following the onset of toxicity. SNIP CAR-T cells also demonstrate enhanced efficacy in numerous models associated with more functional, less exhausted, and higher levels of memory CAR-T cells than those treated with constitutive CAR-T cells. Further, in an on-target off-tumor toxicity mouse model, reduced drug dosing tunes SNIP CAR-T cells to fall within a TW that clears tumor cells expressing high levels of antigen while sparing healthy tissue expressing lower levels of the antigen.

RESULTS

Development and optimization of the SNIP architecture

We sought to develop a high-performance CAR platform regulated by an FDA-approved small molecule. Building on promising results using hepatitis C virus (HCV) NS3 protease (NS3p) and protease inhibitors to regulate diverse proteins (Chung et al., 2015; Jacobs et al., 2018; Tague et al., 2018), we sought to coexpress NS3p and an NS3p cleavage site (CS) between CAR functional domains and thereby cleave CARs at baseline rendering them inactive (OFF state). Exposure to grazoprevir (GPV), an NS3p inhibitor, would prevent cleavage and retain the functional CAR (ON state). We first integrated the CS and protease between the CD8α transmembrane (Tm) and intracellular signaling domains (4-1BB.CD3ζ) in a B7H3-targeting CAR (Figure 1A [left]; *cis* SNIP BBz) (Majzner et al., 2019), which endowed robust GPV-regulated control of CAR cleavage in primary human T cells, but no detectable antitumor activity and reduced surface expression in the ON state (Figures 1A and S1A). Next, the CS and NS3p were integrated between the single-chain variable fragment (scFv) and the CD8α Tm domain (Figure 1B [left]; *cis* SNIP scFv), yielding proteolytic control of the CAR with a wide dynamic range (Figures 1B [middle] and S1B) but diminished antitumor activity in the ON state, potentially due to perturbation of the optimal spacer length between CAR-antigen interactions in the immunological synapse (Figure 1B [right]; Guest et al., 2005; Hudecek et al., 2013).

In the third design, we minimized modification to the CAR by incorporating only a CS between the Tm and signaling domains and delivering a membrane-bound NS3p in *trans* with a CD28 Tm (Figure 1C [left]; *trans* SNIP BBz). T cells expressing the *trans* SNIP B7H3 CAR manifested high cytotoxic activity in the ON state, similar to a constitutive B7H3.BBz CAR (Figure 1C [right]). However, significant leaky activity was observed in the OFF state, likely due to incomplete CAR cleavage at baseline. We next constructed *trans* SNIP systems with various combinations of CD8α or CD28 Tm domains (Figure 1D [left]) and found that matched CD8α or CD28 Tm domains (i.e., 8/8 and 28/28, CAR Tm/protease Tm) yielded more complete SNIP CAR cleavage compared with mismatched Tm configurations (Figure S1C). Further, a matched Tm design reduced residual leaky activity in the OFF state (Figures 1D [middle] and S1C), likely due to homodimerization enhancing proximity of the protease to the cut site (Fujiwara et al., 2020; Hennecke and Cosson, 1993). Expression of membrane-bound protease in the SNIP system did not compromise CAR expression (Figure S1D). The 8/8 Tm version had a wide dynamic range of control (Figure 1E) and an unperturbed surface expression (Figures S1D and S1E) and mediated

(F) Cytokine production of SNIP 8/8 CAR-T cells after coculture with 143B cells treated with various concentrations of GPV.
(G) Cytokine secretion of SNIP CAR-T cells against N6-B7H3 cells incubated in 3 μM GPV for the indicated amount of time prior to the coculture. Mock, no drug, and B7H3.BBz are shared controls and duplicated between the ON and OFF kinetics in Figure S1F.
In (B), B7H3.BBz and mock are shared controls for CAR expression and are duplicated in Figure S1A. Data are mean ± SEM of triplicate wells. In (A)–(C), statistical significance was computed at the final time point by unpaired two-tailed t tests, $^{**}p \leq 0.01$, $^{****}p \leq 0.0001$. In (A)–(G), reproducible in three independent experiments with different donors. Data containing error bars are reported as mean ± SEM.
See also Figure S1.

Please cite this article in press as: Labanieh et al., Enhanced safety and efficacy of protease-regulated CAR-T cell receptors, Cell (2022), https://doi.org/10.1016/j.cell.2022.03.041

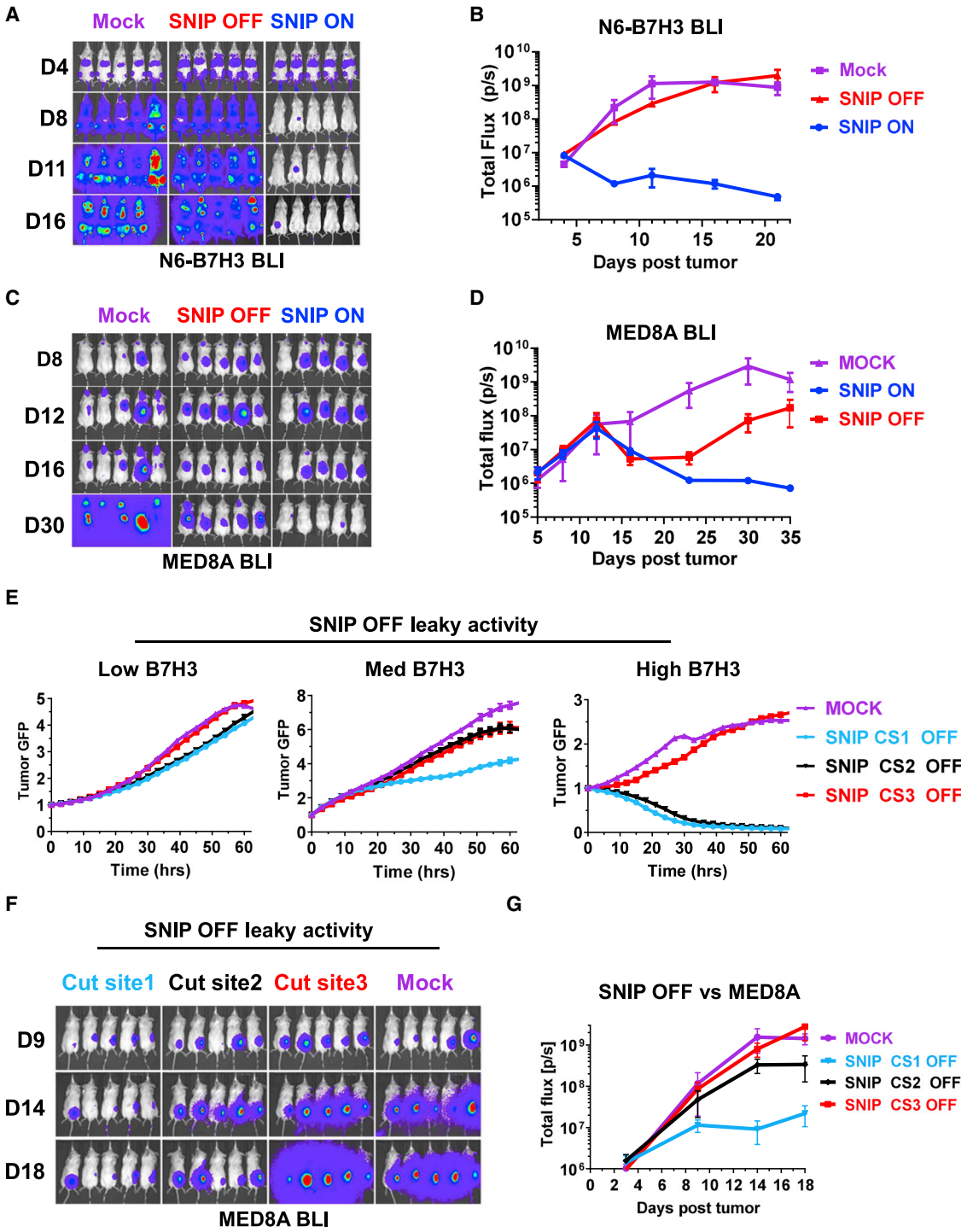

Figure 2. Leaky cytotoxic activity is driven by high antigen density on target lines and ameliorated by substituting cleavage sites with high catalytic activity

(A and B) Tumor BLI of mice inoculated with Nalm6-B7H3 leukemia cells and were then treated with B7H3.BBz CAR or mock T cells 4 days later. SNIP-treated mice were given 50 mg/kg GPV and 25 mg/kg ritonavir (RTV) (SNIP ON) or vehicle control (SNIP OFF) 3 times per day by oral gavage. RTV is a pharmacokinetic enhancer of GPV.

(C and D) Tumor BLI of mice inoculated with MED8A cells in the right flank and cerebellum and were then treated with B7H3.BBz CAR or mock T cells 5 days later.

(E) Cytotoxic activity of SNIP B7H3.BBz bearing different cleavage sites (CSs) against GFP-labeled tumor cells in the absence of GPV (SNIP OFF). Data are mean ± SEM of triplicate wells.

(legend continued on next page)

Please cite this article in press as: Labanieh et al., Enhanced safety and efficacy of protease-regulated CAR-T cell receptors, Cell (2022), https://doi.org/10.1016/j.cell.2022.03.041

more potent antitumor activity than the 28/28 TM in the ON state (Figure 1D [right]). We used the *trans* SNIP architecture to generate SNIP CARs for other tumor antigens by swapping out the scFv domain. For the remainder of this report, all 4-1BB costimulated SNIP CARs are in the 8/8 configuration, and all CD28 costimulated SNIP CARs are in the 28/28 configuration.

We stimulated SNIP B7H3 CAR-T cells with 143B osteosarcoma cells and various GPV concentrations and observed a dose-responsive relationship between GPV and IFNγ and IL-2 secretion (Figure 1F), with a GPV EC50 for IFNγ of 4.3 ± 1.4 nM and for IL-2 of 6.8 ± 1.3 nM, below the 24 h postdose concentration (C_{24}) achieved with 100 mg GPV dosing regimens in humans (Caro et al., 2017). Cytokine secretion by SNIP B7H3 CAR-T cells displayed rapid ON and OFF kinetics (Figures 1G and S1F), and strikingly, SNIP B7H3 CAR-T cells secreted more IL-2 than B7H3.BBz CAR-T cells when preincubated with GPV for short periods (<24 h) (Figure 1G); however, prolonged exposure to GPV led to a progressive drop off in IL-2 secretion reaching similar levels as constitutive B7H3.BBz CARs by 39 h, likely from tonic CAR signaling in the ON state that limits effector capacity (Long et al., 2015; Weber et al., 2020). We previously found that IL-2 secretion serves as a good discriminator of CAR-T efficacy (Spiegel et al., 2021). SNIP B7H3 cytotoxicity could also be controlled *in vivo*, as bioluminescence imaging (BLI) of Nalm6-B7H3 leukemia cells revealed clearance of tumor in the GPV-treated SNIP ON group, but not in the SNIP OFF group (Figures 2A and 2B).

Overcoming leaky activity in response to high antigen density targets through cleavage site optimization

To assess activity of SNIP B7H3 CAR-T cells *in vivo* against a solid tumor, we engrafted MED8A medulloblastoma cells subcutaneously in the flank and the cerebellum of NSG (NOD–SCID Il2rg-null) mice simultaneously, then administered 5 × 10^6 SNIP or mock T cells. The SNIP ON group cleared the tumor, but we observed antitumor activity in the SNIP OFF group (Figures 2C and 2D), consistent with leakiness in the system, as previously reported with regulatable systems (Juillerat et al., 2019; Leung et al., 2019; Richman et al., 2020; Sakemura et al., 2016; Salzer et al., 2020). Leakiness increased with higher antigen density (Figures S2A and S2B), and we hypothesized that it reflected incomplete CAR cleavage in the OFF state, which could potentially be ameliorated by enhancing formation of the protease-CS complex and catalytic turnover. Thus, we designed SNIP variants incorporating CSs with greater catalytic efficiency (cut site 2 and cut site 3) and compared them with the standard CS (cut site 1). Tumor coculture experiments confirmed that receptors incorporating catalytically enhanced SNIP cut site 3 showed no leaky activity, even against tumor lines expressing very high levels of B7H3 (Figures 2E and S2A; >370,000 molecules/cell) and equivalent cytotoxic activity in the ON state (Figure S2C). Temporal responsiveness and wide dynamic range of the SNIP system is illustrated by undetectable full-length CAR in the absence of drug with the two efficient CSs (CS2 and CS3) and full expression of CAR in the ON state compared with a dead protease control (dNS3), even following as little as 24 h exposure to GPV (Figure S2D). We compared performance of the SNIP platform with a B7H3.BBz CAR regulated using destabilization domain (DD) technology, incorporating a drug-dependent dihydrofolate reductase (DHFR) degron fused to the C terminus of the CAR (Iwamoto et al., 2010; Weber et al., 2021). The B7H3.BBz DD displayed leaky residual expression in the OFF state and diminished CAR expression in the ON state (1 μM trimethoprim [TMP]), leading to a narrower dynamic range of expression compared with SNIP. Finally, we confirmed reduced leakiness in the catalytically enhanced variants, with SNIP cut site 3 displaying no detectable leaky activity in the OFF state in the MED8A *in vivo* model (Figures 2F and 2G).

SNIP CAR-T cells have enhanced efficacy in solid tumor models compared with constitutive CARs

We next compared efficacy of optimized SNIP CARs with constitutive CARs in orthotopic solid tumor models. NSG mice were inoculated with 1 × 10^6 CHLA255 neuroblastoma cells by renal capsule injection and were then treated with 10 × 10^6 SNIP or constitutive GD2.BBz CAR-T cells 7 days later (Figure 3A). The SNIP GD2 CAR-T cells rapidly cured the mice of CHLA255 tumor in the ON state, whereas constitutive GD2.BBz CAR-T cells exerted only modest antitumor activity (Figures 3B and 3C). Similarly, in an orthotopic MG63.3 osteosarcoma model, we observed enhanced antitumor efficacy and more rapid tumor clearance with SNIP HER2 versus constitutive HER2.BBz CAR-T cells (Figures S3A–S3C), results that were confirmed in the more aggressive 143B osteosarcoma model (Figures 3D and 3E).

To test if SNIP CAR-T cells are functional in the central nervous system (CNS) tumors, we implanted MED8A medulloblastoma in the cerebellum of NSG mice and were then treated with 3 × 10^6 SNIP or constitutive B7H3.BBz CAR-T cells (Figure 3F). Remarkably, SNIP B7H3.BBz CAR-T cells outperformed constitutive B7H3.BBz CAR-T cells in this difficult-to-treat CNS tumor model (Figures 3G, 3H, and S3D–S3F), suggesting that adequate GPV levels may be achieved in the setting of brain tumors and/or that the kinetics of T cell trafficking between the CNS and the periphery enables sufficient SNIP ON activity, even if local GPV levels are limiting. To assess the mechanism responsible for enhanced SNIP CAR efficacy in this model, we undertook T cell imaging using an Antares bioluminescence reporter (Chu et al., 2016; Su et al., 2020), which revealed greater persistence of SNIP ON CAR-T cells in the CNS and the periphery (Figures S3G–S3I) compared with the constitutive CARs. We also observed persistence of SNIP OFF CAR-T cells that could be due to homeostatic T cell expansion (Mackall et al., 1997; Onoe et al., 2010) and onset of xenogeneic graft-versus-host disease (GVHD) (Ali et al., 2012; Kamiya et al., 2018; Mount et al., 2018). *Ex vivo* stimulation with plate bound B7H3-Fc of

(F and G) Tumor BLI of mice inoculated with MED8A cells in the right flank and were then treated with B7H3.BBz or mock T cells on day 5. GPV was not administered to mice (SNIP OFF).

In (A)–(D), (F), and (G), experiments were reproducible in two independent experiments with separate donors. Data are mean ± SEM.

See also Figure S2.

Please cite this article in press as: Labanieh et al., Enhanced safety and efficacy of protease-regulated CAR-T cell receptors, Cell (2022), https://doi.org/10.1016/j.cell.2022.03.041

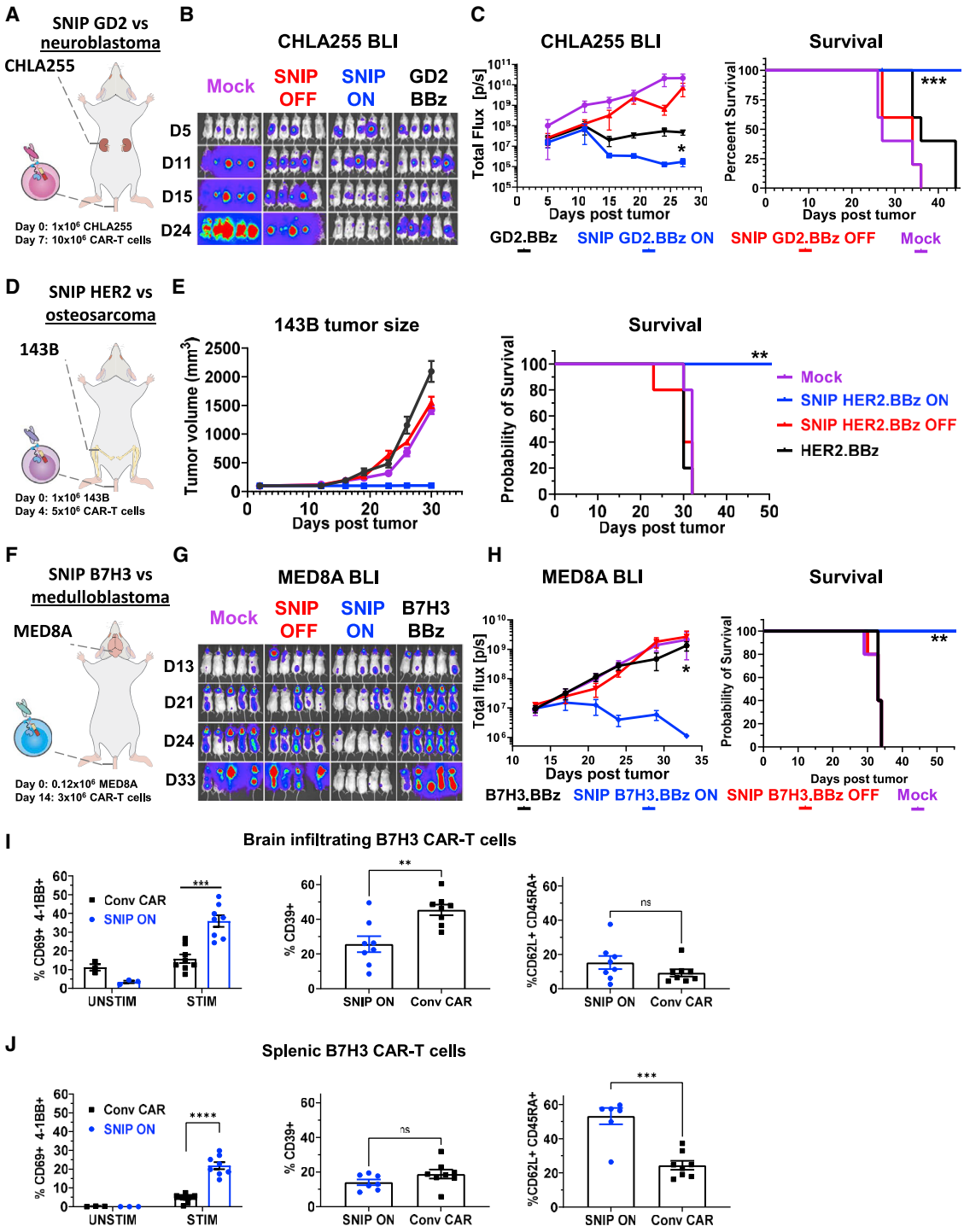

Figure 3. SNIP CAR-T cells display enhanced antitumor efficacy in orthotopic solid tumor models

(A) Schematic of the CHLA255 neuroblastoma kidney capsule tumor model using GD2-specific CARs.

(B) Tumor progression of CHLA255 by BLI.

(C) Quantification of BLI (left) and survival curves of mice in the CHLA255 neuroblastoma model (right).

(D) Schematic of the 143B osteosarcoma tumor model using HER2-specific CARs.

(E) Tumor progression in the 143B osteosarcoma was monitored by tumor volume measurements (left) and survival curves in the 143B model (right).

(F) Schematic of the MED8A medulloblastoma brain tumor model using B7H3-specific CARs.

(G) Tumor progression of MED8A BLI.

(legend continued on next page)

Please cite this article in press as: Labanieh et al., Enhanced safety and efficacy of protease-regulated CAR-T cell receptors, Cell (2022), https://doi.org/10.1016/j.cell.2022.03.041

CAR-T cells harvested from brains and spleens 10 days after T cell infusion demonstrated greater activation of brain infiltrating SNIP CAR-T cells, whereas constitutive B7H3 CAR-T cells had increased basal levels of activation, limited response to antigen stimulation, and increased levels of the exhaustion marker CD39 (Figure 3I). We also observed enhanced functionality and increased stem cell memory subsets ($CD62L^+CD45RA^+$) of splenic SNIP versus constitutive CAR-T cells (Figure 3J). SNIP CD19.BBz CAR-T cells also showed equivalent antitumor efficacy against a Nalm6 leukemia model (Figures S3J–S3L).

SNIP CAR-T cells are phenotypically and transcriptionally distinct and functionally superior to constitutive CAR-T cells

To better understand the basis for the superior potency of SNIP versus constitutive CARs, we conducted mass cytometry of HER2, GD2, and B7H3.BBz SNIP versus constitutive CAR-T cells after the 10-day CAR-T cell transduction and expansion process. Constitutive CAR-T cells manifested increased levels of effector-/exhaustion-associated proteins, whereas SNIP CAR-T cells cultured in the absence of GPV (SNIP OFF)-expressed markers associated with stemness, similar to mock untransduced controls (Figures 4A and S4A). Bulk RNA sequencing (RNA-seq), differential expression (Figure S4B), and gene set enrichment analysis (GSEA) revealed that constitutive CARs showed a significant enrichment of genes upregulated in effector versus memory T cells (Wherry et al., 2007) and associated with T cell exhaustion (Good et al., 2021), whereas SNIP CAR-T cells demonstrated increased levels of genes upregulated in nonexhausted CD19.BBz CAR-T cells (Lynn et al., 2019; Figure S4C).

Tumor-infiltrating lymphocytes (TILs) and splenic T cells from mice engrafted with 143B osteosarcomas and treated with SNIP ON versus constitutive HER2.BBz CAR-T cells (Figure 4B) were compared. Splenic SNIP CAR-T cells were present at a higher frequency (Figure 4C), contained a larger fraction of stem cell memory subsets (Figures 4D and S4D), maintained a normal $CD4^+$ to $CD8^+$ ratio (Figure S4E), and were more responsive than constitutive CAR-T cells upon antigen stimulation *ex vivo* (Figures 4E and S4F). Similarly, TILs from SNIP CAR-T-treated mice expressed lower levels of the exhaustion marker CD39 than those treated with constitutive CAR-T cells (Figure 4F).

Single-cell RNA sequencing (scRNA-seq) analysis, dimensionality reduction, and clustering on TILs harvested from 143B engrafted mice (Figures 5A–5C) confirmed more TILs in SNIP compared with constitutive HER2.BBz-treated mice with several clusters nearly exclusively comprising SNIP CAR-T cells. Within these unique clusters were $CD4^+$ cells that expressed genes associated with memory markers (TCF7 and IL7R) and $CD8^+$ cells that expressed high levels of cytotoxic genes (GZMB, GNLY, and NKG7) (Figures 5D, 5E, and S5A). A similar number of SNIP and constitutive CAR-T cells were in G2M and S phase; however, SNIP cells also formed a large pool in G1 phase, which was substantially lower in the constitutive group (Figures S5B and S5C). Together, these data demonstrate that SNIP CAR-T cells manifest diminished exhaustion features prior to adoptive transfer, undergo greater expansion following adoptive transfer, and simultaneously generate stem-like populations as well as effector subsets *in vivo* that mediate significantly enhanced potency against solid tumors.

To investigate whether enhanced functionality of SNIP CARs is due to a "resting" effect when cultured in the OFF state or due to specific attributes of the molecular architecture, we created a dead protease SNIP (dNS3) control by mutating the active site serine of NS3p to an alanine, which abolishes proteolytic activity (Lai et al., 2000). T cell phenotype and function, downstream phosphorylation, and tonic signaling of constitutive B7H3.BBz CAR, SNIP CARs exposed to GPV for short (SNIP ON 24 h) and long (SNIP ON 144 h) periods, and relevant controls were measured. SNIP B7H3 CAR-T cells grown in the absence of GPV until 24 h prior to tumor coculture (SNIP CS2 ON 24 h) displayed the fastest tumor killing kinetics (Figure S5D). We derived a tumor-killing kinetic parameter, T_{Kill50}, that is the time point at which the tumor GFP level reaches less than 50% of the initial value. On average, the rested SNIP CAR-T cells (ON 24 h) killed tumor cells ~40% faster than conventional, dNS3, or SNIP ON 144 h CAR-T cells. These findings demonstrate enhanced functionality of SNIP cells manufactured in the OFF state and is consistent with previous work demonstrating that transient "rest" of CAR-T cells enhances their functionality through epigenetic remodeling (Weber et al., 2021) and another study demonstrating reduced tonic signaling and greater potency when the CAR was targeted to the T cell receptor alpha constant (TRAC) locus (Eyquem et al., 2017). Phenotypic analysis of D10 *in vitro* CAR-T cells confirmed reduced exhaustion markers on SNIP OFF and mock T cells relative to controls (Figure S5E). We also observed a small but significant increase of $CD62L^+$ $CD45RA^+$ subsets in SNIP dNS3 and SNIP ON 144 h, compared with conventional B7H3.BBz CAR-T cells. However, the most dramatic increase was seen in the SNIP OFF and mock T cells.

Stimulation with B7H3-Fc induced similar levels of phosphorylated CAR-CD3ζ signal (pCD3ζ) for SNIP ON and constitutive groups; however, rested SNIP (ON 24 h) CAR-T cells expressed higher levels of early activation markers and phosphorylation of downstream signaling molecules than nonrested and constitutive controls in response to stimulation (Figure S5F). Expression of activation markers and phosphorylation of downstream signaling molecules induced by tonic signaling was similar across SNIP ON and constitutive controls (Figure S5G). GPV had no direct effect on T cell function or tumor cell proliferation

(H) Quantification of MED8A medulloblastoma BLI (left), and survival curves of mice in the MED8A medulloblastoma model (right).
(I and J) Expression of surface markers on SNIP or conventional B7H3.BBz CAR-T cells harvested from (I) spleens and (J) brains 10 days after treatment in the medulloblastoma model shown in Figure S3D–S3I (n = 8 mice per group). Data are mean ± SEM of n = 8 mice. p values were determined by unpaired two-tailed t tests, ns $p > 0.05$, $^{**}p \leq 0.01$, $^{***}p \leq 0.001$, $^{****}p \leq 0.0001$.
In (C), (E), and (H), tumor quantification data are mean ± SEM of n = 5 mice in each group. p values were determined by unpaired two-tailed t tests. Survival curves were compared by the log-rank Mantel-Cox test, $^{**}p \leq 0.01$, $^{***}p \leq 0.001$. Reproducible in two independent experiments with different donors.
See also Figure S3.

Please cite this article in press as: Labanieh et al., Enhanced safety and efficacy of protease-regulated CAR-T cell receptors, Cell (2022), https://doi.org/10.1016/j.cell.2022.03.041

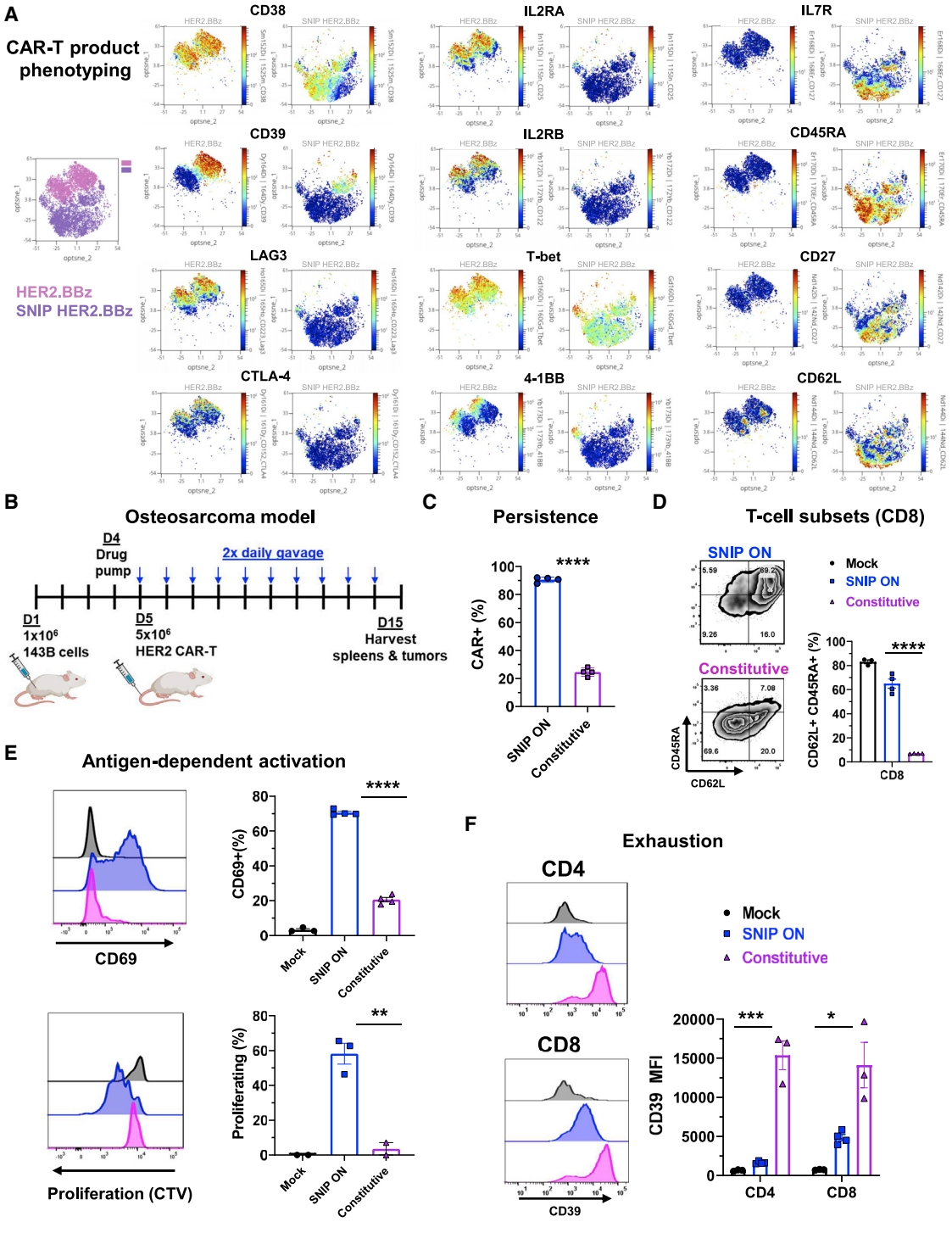

Figure 4. SNIP CAR-T cells in culture and isolated from treated mice are less exhausted, develop larger fractions of T_{SCM} subsets, and are more responsive to *ex vivo* stimulation than constitutive CAR-T cells

(A) Mass cytometry analysis of levels of expression of exhaustion, activation, and T_{SCM}-associated markers on $CD8^+$ constitutive HER2.BBz and SNIP HER2.BBz CAR-T cells after the 10-day manufacturing period.

(B) Schematic of the 143B osteosarcoma model.

(C) Persistence of SNIP CAR-T cells as measured by frequency of CAR^+ cells gated on live $CD45^+$ cells from spleens of treated mice.

(D) Representative flow plots showing surface expression of CD45RA and CD62L on splenic $CD8^+$ HER2 CAR-T cells (left) and quantification of T_{SCM} subsets on splenic CAR-T cells (right).

(legend continued on next page)

Please cite this article in press as: Labanieh et al., Enhanced safety and efficacy of protease-regulated CAR-T cell receptors, Cell (2022), https://doi.org/10.1016/j.cell.2022.03.041

(Figure S5H). Taken together, the phenotypic, signaling, and functional data provide evidence that cleavage of the signaling domains in the SNIP system ablates CAR tonic signaling, leading to reduced levels of exhaustion and greater stemness in the OFF state. When rested SNIP CAR-T cells are turned ON with GPV for limited periods, they have a greater capacity to transduce CAR proximal signaling into downstream pathways and faster tumor-killing kinetics than conventional, dNS3, and always ON SNIP CAR-T cells, although this effect is ablated when SNIP CARs are exposed to full dose drug for 144 h.

Development and characterization of a fatal on-target off-tumor ROR1 CAR toxicity model

We next sought to test if the SNIP system could provide a safety switch in the event of CAR-mediated on-target toxicity. Previous work has shown that ROR1(R11).BBz-CAR-T cells induce lethal on-target off-tumor toxicity in NSG mice preconditioned with radiation (Srivastava et al., 2019). To avoid potential confounding factors associated with irradiation, we constructed ROR1 CARs based on the clone F antibody (ROR1(F)) with CD28 or 4-1BB signaling domains (Figure S6A [top]; Nathwani et al., 2019). Staining of ROR1(F).28z CAR-T cells with ROR1-Fc confirmed cross-reactivity to human and mouse ROR1 (Figure S6B). Nontumor-bearing mice treated with ROR1(F).28z CAR-T cells developed severe toxicity without radiation, as indicated by rapid weight loss and death within 11 days after CAR treatment (Figure S6A [middle and bottom]), consistent with the strong signal strength of CD28-costimulated CARs (Majzner et al., 2020; Salter et al., 2018).

To identify sites of on-target off-tumor activity associated with ROR1(F).28z CAR-T cell toxicity, we constructed a T cell activation reporter by placing the highly sensitive luciferase, Antares, downstream of NF-κB response elements (Figure 6A; Chu et al., 2016; Su et al., 2020). BLI of ROR1(F).28z CAR-T cells co-transduced with a constitutive firefly luciferase and the NF-κB-Antares reporter, which enabled simultaneous tracking of total and activated T cells, revealed similar total T cell signal from ROR1(F).28z and control CD19.28z CAR-T cell-treated mice (Figure 6B [right panel]), but activated T cells were only detected in ROR1(F).28z-treated mice (Figure 6B [left panel]). *Ex vivo* Antares BLI of organs harvested 48 h after T cell administration identified the lungs, spleen, and kidney as predominant sites of activated ROR1(F).28z CAR-T cells (Figure 6C). Immunohistochemistry (IHC) staining confirmed infiltration of ROR1(F).28z T cells in the lungs, around vessels and bronchioles with accompanying perivascular edema (Figure 6D), and human and mouse scRNA-seq data identified the lungs as the most prominent site of ROR1 expression (Figures S6C and S6D), including alveolar type I cells, alveolar type II cells, fibroblasts, pericytes, smooth muscle cells, and mesothelial stromal cells (Figure S6C). Together, these data credential the ROR1(F).28z-CAR as inducing lethal on-target toxicity targeting the mouse lung and suggest that NF-κB-based reporters can potentially distinguish cognate antigen driven activation from homeostatic proliferation *in vivo*.

Cessation of drug dosing reverses toxicity and modulation of drug dosing open a therapeutic window for SNIP ROR1(F).28z CAR-T cells

To test whether cessation of drug dosing could reverse SNIP CAR toxicity, we treated nontumor-bearing mice with 10×10^6 SNIP ROR1(F).28z, constitutive ROR1(F).28z, or mock T cells. SNIP groups were treated for 2 days with either 50 mg/kg GPV and 25 mg/kg ritonavir (RTV) 3× per day (SNIP ON rescue) or vehicle control (SNIP OFF) and monitored for weight loss (Figure 6E). Mice treated with constitutive CAR-T cells developed rapid toxicity that was lethal within 4 days after treatment (Figure 6F). Mice treated with SNIP and continuous high GPV dosing also developed rapid lethal toxicity (Figure S7A); however, cessation of GPV at day 2 reversed the toxicity, as evidenced by a rebound in weight (Figure 6F).

We hypothesized that bioactivity of SNIP ROR1(F).28z CAR-T cells could be tuned by modulating GPV dosing to enable targeting of tumor cells expressing high levels of antigen while sparing healthy tissue with lower antigen expression. To model the impact of SNIP CAR-T tuning on antigen density thresholds *in vitro*, we cultured single-cell clones of Nalm6-ROR1 leukemia stably expressing various levels of surface ROR1 (Figure S7B) with SNIP ROR1(F).28z CAR-T cells at varying GPV concentrations. We observed some antigen densities, wherein the highest dose of GPV induced plateaued cytokine production, but at lower GPV doses, we observed antigen density induced gradations in cytokine production (Figure 7A), consistent with GPV mediated analog tuning of antigen density thresholds that could open TWs for shared antigens (Figure S7C). To test this hypothesis *in vivo*, we inoculated mice with Nalm6-ROR1 tumor cells and then administered a reduced dosing strategy of 25 mg/kg GPV and 2.5 mg/kg RTV, given only once per day as a TW regimen (SNIP ON_{TW}). SNIP ROR1(F).28z mice treated with the SNIP ON_{TW} regimen did not develop weight loss and maintained robust antitumor activity that led to complete cures and significant survival advantage (Figures 7B–7D). Mice treated with constitutive ROR1(F).28z had tumor regression but died shortly after T cell administration due to on-target off-tumor toxicity in the lungs and liver, which was noticeably milder in animals treated with SNIP ROR1(F).28z ON_{TW} CAR-T cells (Figures 7E and S7Di–S7Dviii).

SNIP outperforms other drug-regulatable CAR systems in mouse models of safety and efficacy

We tested the ability of dasatinib, an inhibitor of TCR and CAR signaling, to achieve safety control in the ROR1 toxicity model (Weber et al., 2019, 2021). Mice treated with conventional ROR1(F).28z CAR-T cells experienced 100% lethality within 8 days and treatment with 50 mg/kg dasatinib twice per day delayed toxicity and provided small but significant survival

(E) Splenic CAR-T cells were stimulated with plate bound HER2 then analyzed for CD69 expression (top) and proliferation (bottom).
(F) Surface expression of the exhaustion marker CD39 on CAR^+ TILs. In (C)–(F), bar graph data are mean of individual mice ± SEM of each group. p values were determined by unpaired two-tailed t tests, *$p \leq 0.05$, **$p \leq 0.01$, ***$p \leq 0.001$, ****$p \leq 0.0001$
See also Figures S4 and S5.

Please cite this article in press as: Labanieh et al., Enhanced safety and efficacy of protease-regulated CAR-T cell receptors, Cell (2022), https://doi.org/10.1016/j.cell.2022.03.041

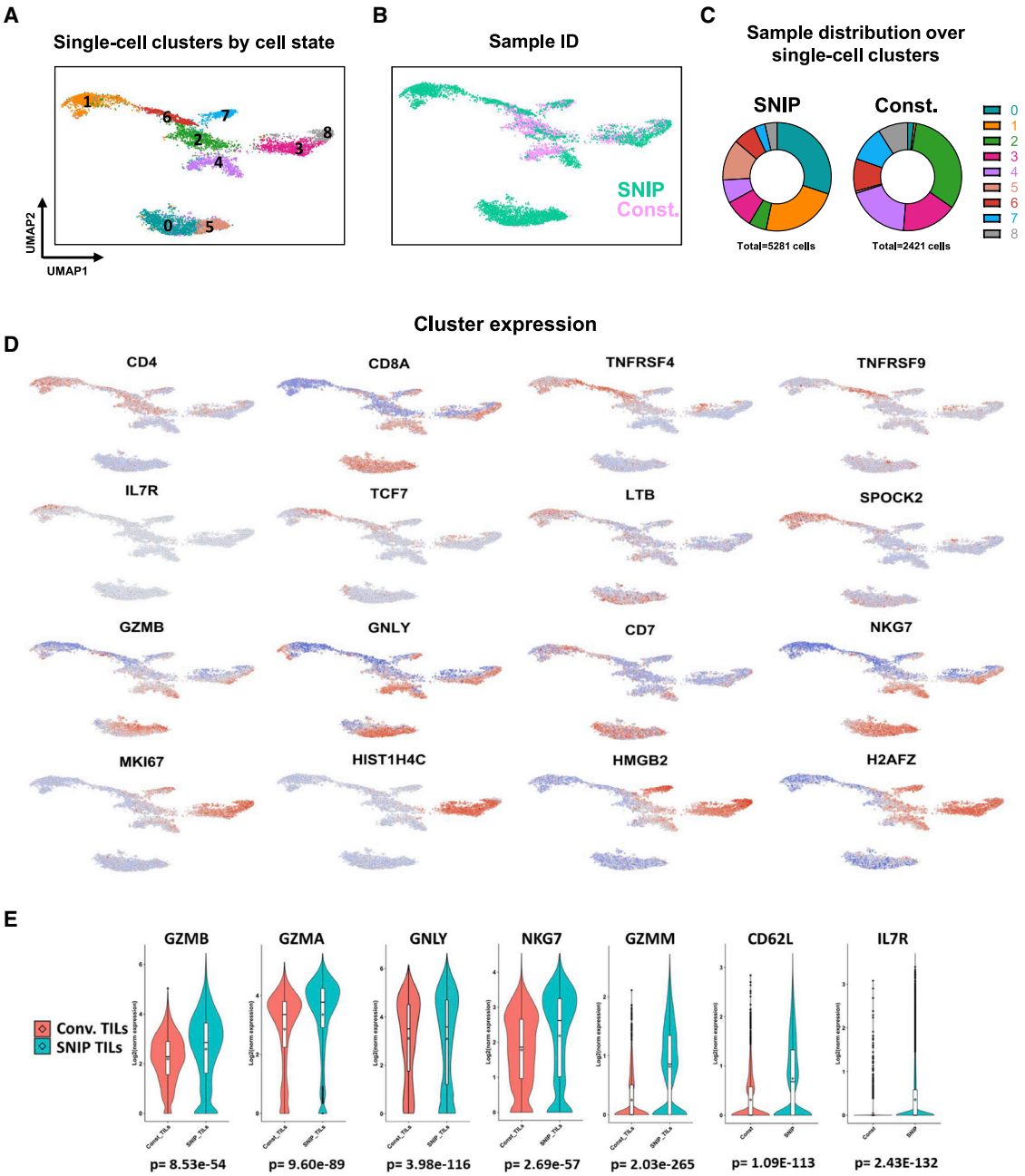

Figure 5. scRNA-seq analysis identifies unique subsets in SNIP CAR TILs that include CD4$^+$ memory cells and CD8$^+$ cells with high expression of cytotoxic genes

HER2.BBz CAR TILs were harvested from mice in the 143B osteosarcoma model 10 days after T cell administration.

(A–C) Uniform manifold approximation and projection (UMAP) dimensionality reduction and clustering of CAR TILs by transcriptomic states.

(D) Select gene expression features in UMAP analysis.

(E) Violin plots showing the distribution of expression of cytotoxic and memory associated markers. p values are indicated below each plot and were determined by unpaired two-tailed Mann-Whitney U test.

See also Figure S5.

benefit; however, mice ultimately succumbed to the toxicity of the ROR1(F).28z CAR-T cells. In contrast, mice treated with SNIP CAR-T cells and TW drug dosing (25 mg/kg GPV and 2.5 mg/kg RTV once per day) demonstrated antitumor activity and survival benefit, with greater antitumor activity against ROR1$_{Med}$ than ROR1$_{Low}$ tumor cells (Figures S7E and S7F). We also compared SNIP performance with the CARs incorporating a DD in this aggressive toxicity model. Immunoblotting

Please cite this article in press as: Labanieh et al., Enhanced safety and efficacy of protease-regulated CAR-T cell receptors, Cell (2022), https://doi.org/10.1016/j.cell.2022.03.041

CellPress
OPEN ACCESS

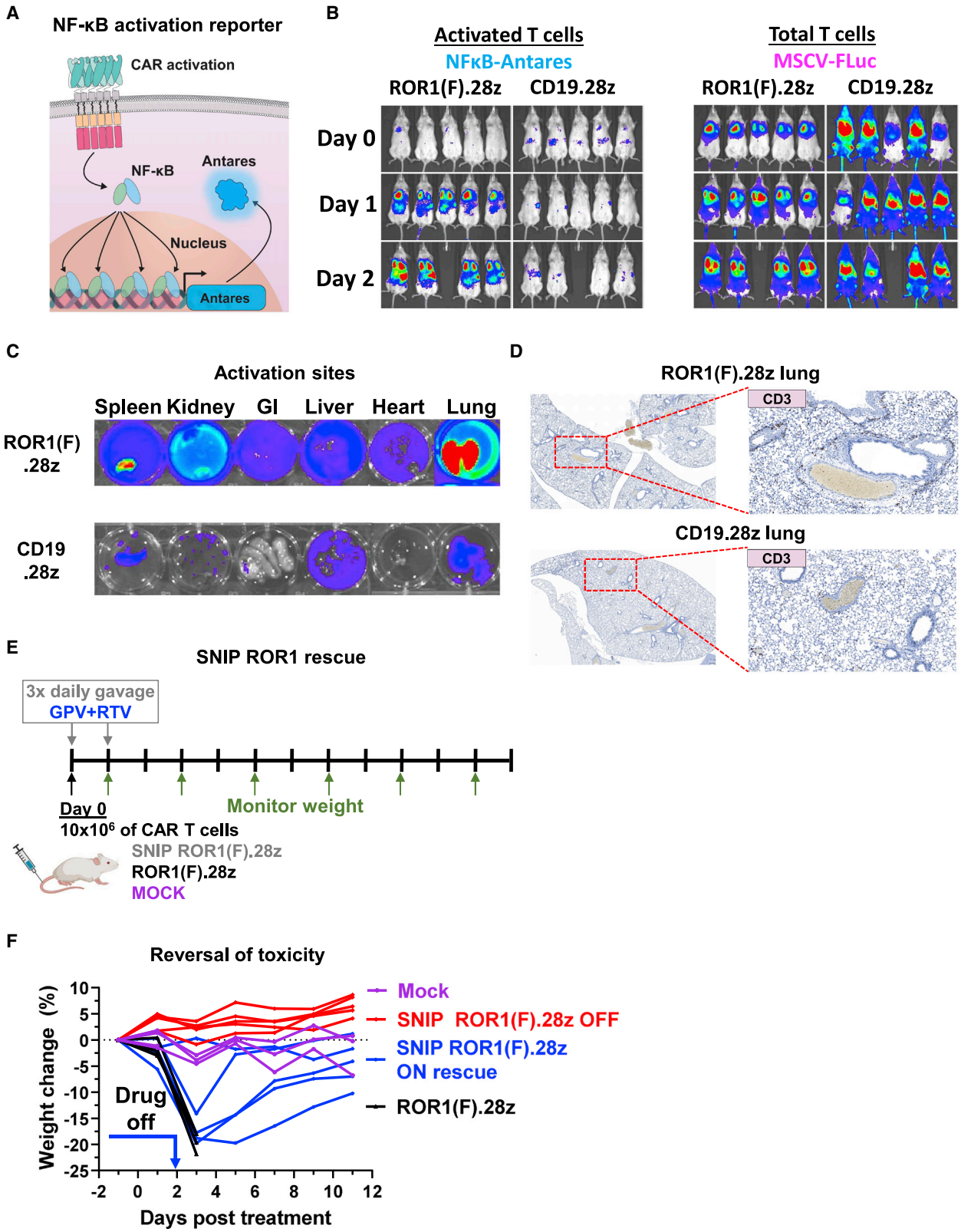

(legend on next page)

Please cite this article in press as: Labanieh et al., Enhanced safety and efficacy of protease-regulated CAR-T cell receptors, Cell (2022), https://doi.org/10.1016/j.cell.2022.03.041

of CD3ζ revealed a leaky expression of the DD-regulated CAR in the OFF state and diminished expression in the ON state compared with a conventional CAR control, leading to a narrower dynamic range compared with SNIP regulated CARs (Figure S2D). *In vivo*, animals receiving ROR1(F).28z DD CAR OFF experienced toxicity similar to constitutive ROR1(F).28z CAR, whereas SNIP OFF and mock-treated mice showed no signs of toxicity (Figures S7G and S7H). ROR1 DD-treated mice were thin, weak, hunched, scruffy, and hyperventilating, whereas the SNIP ROR1-treated mice appeared healthy (Videos S1 and S2). The NF-κB-Antares reporter confirmed Antares induction in ROR1 DD OFF but not SNIP OFF CAR-T cells stimulated with ROR1+ tumor cells *in vitro* (Figure S7I) and due to on-target, off-tumor toxicity *in vivo* (Figure S7J).

We utilized the HER2 143B model to mechanistically compare *in vivo* functionality of SNIP to two other drug-regulated systems. We rested cells using (1) a DD HER2.BBz CAR manufactured in the absence of TMP, (2) a SNIP HER2.BBz CAR manufactured in the absence of GPV, and (3) the constitutive HER2.BBz CAR manufactured with dasatinib (Weber et al., 2021). Constitutive, dasatinib-rested constitutive, and dNS3-treated mice had no benefit relative to the mock control. In contrast, both SNIP- and DD HER2-treated mice dosed with GPV or TMP, respectively, had dramatically enhanced *in vivo* benefit (Figures S7K and S7L). Flow cytometry of preinfusion T cells showed an incomplete recovery of memory subsets in dasatinib-treated HER2.BBz, whereas SNIP OFF and DD OFF cells displayed a memory phenotype similar to mock T cells (Figure S7M), consistent with incomplete cessation of CAR signaling with dasatinib compared with the other systems. Another possible factor contributing to the differential *in vivo* response between the dasatinib-rested versus the SNIP/DD groups is that the latter could experience oscillatory CAR signaling arising from variability in GPV or TMP levels associated with normal PK, thereby delaying exhaustion and promoting long-term functionality.

DISCUSSION

Remarkable antitumor effects of CAR-T therapies in B cell malignancies have been offset by high rates of CRS and neurotoxicity, which can be fatal. Moreover, as the field strives to improve the therapeutic efficacy of CAR-T cells against solid tumors, particularly with untested target antigens and with CAR-T cells engineered for enhanced potency, the risks of on-target toxicity pose a major barrier to progress. Synthetic biology could provide solutions to these challenges, but current drug-regulated platforms have limitations including leaky activity, which risks toxicity even in the OFF state, and diminished potency in the ON state, and some employ immunosuppressive drugs as regulators (Giordano-Attianese et al., 2020; Jan et al., 2021; Juillerat et al., 2019; Leung et al., 2019; Richman et al., 2020; Sakemura et al., 2016; Salzer et al., 2020; Wu et al., 2015; Zajc et al., 2020). Adapter-CARs could enable control of T cell activity and specificity (Cho et al., 2018; Darowski et al., 2019; Rodgers et al., 2016; Tamada et al., 2012); however, these platforms have not yet been demonstrated clinically to mitigate toxicity or enhance efficacy. Further, the majority of these platforms utilize protein-based adapters, which require significant expense and time to develop, credential, and produce for clinical use and may have limited penetration into tumor tissue and the CNS. Here, we developed SNIP, an optimized, protease-based, drug-regulated platform for remote control of CAR-T cell effector activity that demonstrates enhanced potency compared with constitutive CARs and has been engineered to be completely devoid of leaky activity.

T cell exhaustion is a major factor limiting clinical efficacy of CAR-T cells. Many CARs manifest tonic signaling during *in vitro* manufacturing, leading to early exhaustion that limits potency (Eyquem et al., 2017; Long et al., 2015; Lynn et al., 2019), and exposure to high tumor burdens also induces exhaustion in the absence of tonic signaling (Long et al., 2015). We have previously demonstrated that transient cessation of CAR signaling can enhance functionality by preventing and reversing hallmark phenotypic, functional, transcriptomic, and epigenetic feature of exhaustion (Weber et al., 2021). Eyquem et al. previously demonstrated that targeting a CAR to the TRAC locus resulted in optimal expression kinetics, reduced tonic signaling, and greater antitumor efficacy (Eyquem et al., 2017). Consistent with this paradigm, SNIP CAR-T cells grown in the absence of drug (OFF) manifest transcriptional and proteomic profiles distinct from constitutive CARs, associated with greater stemness, diminished exhaustion, and increased responsiveness to *ex vivo* antigen stimulation (Figures 3I, 3J, and 4). These results provide clear evidence that SNIP CARs are biologically distinct and more potent than constitutive CARs, which we posit results from variability in GPV levels associated with normal PK that oscillate CAR signaling, thereby preventing exhaustion and improving CAR-T cell function (Weber et al., 2020). In this study, we demonstrate that the SNIP platform enhances CAR-T functionality through a resting effect, and we have focused on 4-1BB costimulated CARs that are lead clinical candidates. However, tonic signaling CARs bearing CD28 endodomains

Figure 6. ROR1(F).28z CAR-T cells are rapidly activated in vivo in non-tumor bearing mice and SNIP ROR1(F).28z CAR-T toxicity is reversed after drug withdrawal

(A) Schematic of the NF-κB Antares reporter for imaging activation of T cells *in vivo*.

(B) Nontumor-bearing NSG mice were treated with 10×10^6 ROR1(F).28z CAR or CD19.28z CAR-T cells by tail vein injection. Activation of T cells was monitored daily by BLI using the NF-κB-Antares reporter (left). BLI of total T cells using the constitutive MSCV-Fluc reporter (right).

(C) Two days after T cell administration, mouse organs were explanted and probed for the presence of activated T cells using the NF-κB-Antares reporter system.

(D) $CD3^+$ infiltrates in mouse lungs identified by IHC analysis.

(E) Schematic of the SNIP toxicity rescue model. Nontumor-bearing NSG mice were engrafted with 10×10^6 ROR1(F).28z CAR, SNIP ROR1(F).28z CAR, or mock T cells. Mice in the SNIP group were administered 50 mg/kg GPV and 25 mg/kg RTV by oral gavage 3 times per day for the first 2 days (SNIP ON) or vehicle control (SNIP OFF). Treatment-related toxicity was monitored by weight change.

(F) SNIP ROR1(F).28z toxicity, as measured by weight change, is reversed after cessation of drug treatment (ON rescue).

See also Figure S6.

Please cite this article in press as: Labanieh et al., Enhanced safety and efficacy of protease-regulated CAR-T cell receptors, Cell (2022), https://doi.org/10.1016/j.cell.2022.03.041

CellPress
OPEN ACCESS

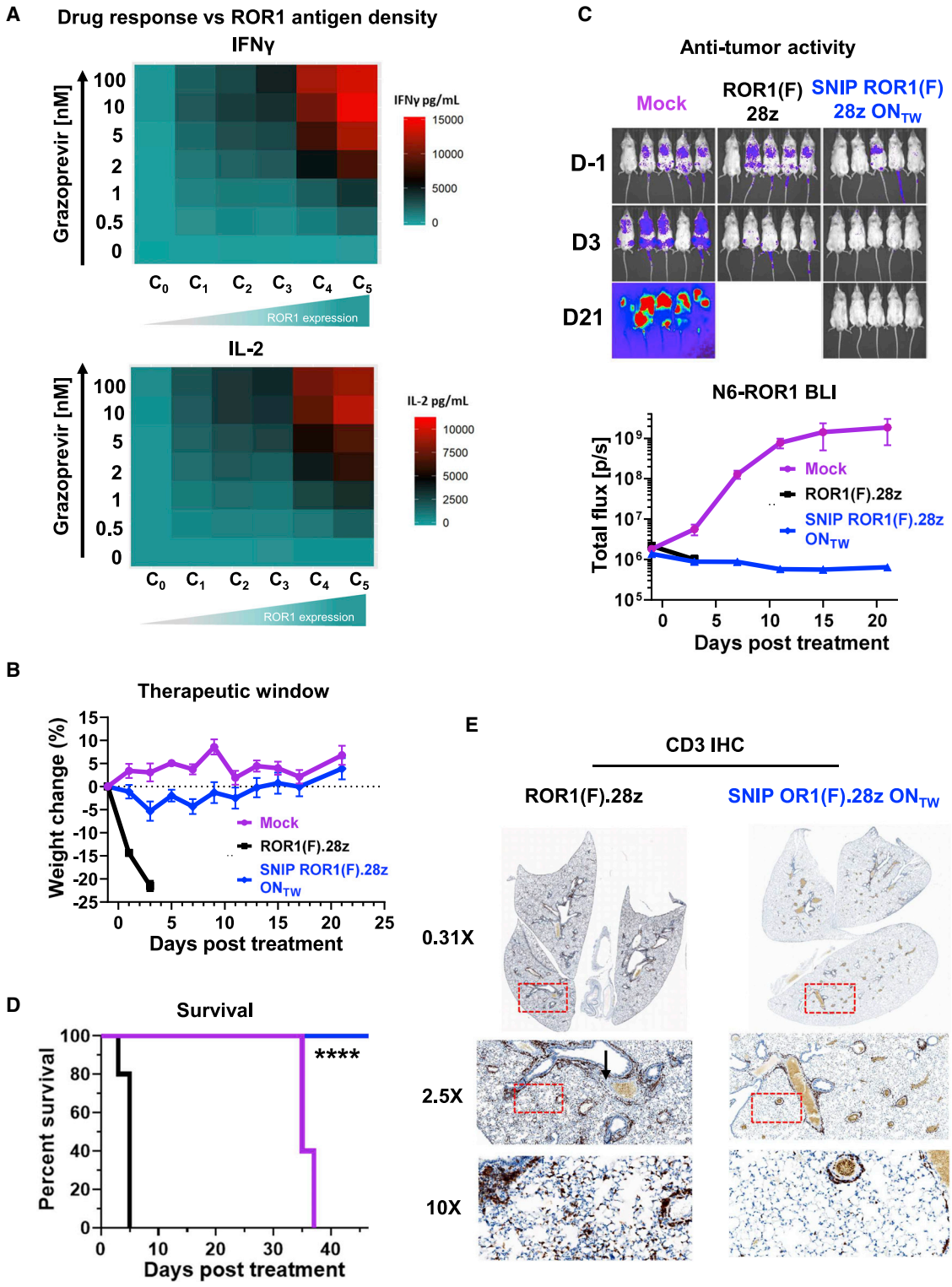

Figure 7. Modified drug dosing opens a therapeutic window for SNIP ROR1(F).28z CAR-T cells resulting in potent antitumor efficacy without toxicity

(A) IFNγ and IL-2 secretion from SNIP ROR1(F).28z CAR-T cells cocultured with various ROR1-expressing lines (see Figure S7B) in the presence of various concentrations of GPV.

(legend continued on next page)

Please cite this article in press as: Labanieh et al., Enhanced safety and efficacy of protease-regulated CAR-T cell receptors, Cell (2022), https://doi.org/10.1016/j.cell.2022.03.041

often manifest higher degrees of exhaustion than 4-1BB CARs and would likely receive even greater benefit from rest. We demonstrated that SNIP serves as a bona fide safety switch in a ROR1 on-target off-tumor toxicity model (Figures 6E and 6F) and that the activity of SNIP ROR1 CARs can be tuned to fall within a TW by modulating the dose and frequency of GPV leading to 100% survival (Figures 7B–7E).

In a real-world setting, predicting the dose necessary to deliver a TW for individual patients could prove challenging due to interpatient variability in tumor burden, antigen expression, drug PK, and T cell potency. A detailed trial design for first-in-human testing of SNIP CARs is beyond the scope of this manuscript, but we envision a cautious cell and small molecule dose escalation strategy with careful toxicity monitoring and the option for individualized modulation of small molecule dosing based upon clinical endpoints. Using Bayesian adaptive study designs that are commonly employed in early phase trials and an experienced clinical team, we are confident that the approach would be feasible (Chow, 2014; Fan et al., 2020). The tunability of SNIP CAR-T cell functionality demonstrated here could create a new paradigm for CAR-T therapy, whereby higher T cell doses could be safely administered, which could ultimately improve patient responses, but activity could be titrated by drug dosing to avoid toxicity associated with rapid immune responses and high levels of proinflammatory cytokines, particularly in patients with high tumor burden. Clinical studies will be needed to establish the degree of tunability achievable in humans, particularly considering the longer half-life of GPV in humans compared with mice.

GPV has several features that make it a promising candidate for clinical use. It is (1) an FDA-approved drug, (2) a cell-permeable molecule that should penetrate well into tumor tissue, and (3) can be maintained at sufficiently high plasma concentrations with well-tolerated chronic-dosing regimens (Caro et al., 2017; Rockstroh et al., 2015). GPV has been reported to have poor blood–brain barrier (BBB) permeability (FDA, 2016). However, SNIP B7H3 CAR-T cells demonstrated enhanced antitumor activity in CNS tumor models compared with constitutive B7H3 CAR-T cells (Figures 3F–3H). Further studies are required to determine if SNIP CAR-T cells serve as vehicles that transport GPV into the CNS or if the kinetics of CAR-T cell trafficking between the CNS and the periphery allow for sufficient SNIP ON activity even if local GPV levels are limiting. It is also possible that GPV is able to cross due to increased BBB permeability in CNS tumor models.

Immunogenicity of the HCV-derived NS3p is a theoretical limitation of the SNIP system. However, it remains unclear if immunogenicity is a significant obstacle to CAR-T therapy in lymphodepleted patients, as the six highly-active FDA-approved CAR constructs to date utilize potentially immunogenic nonhuman scFvs. Furthermore, NS3p, which comprises the N-terminal domain (186 amino acids) of HCV NS3, is minimally immunogenic for T cell epitopes (Erickson et al., 2001; Meyer-Olson et al., 2004; Schulze zur Wiesch et al., 2005; Zhang et al., 2017a). If immune responses were induced, computational approach could be used to engineer NS3p variants to further reduce the potential for MHC-loaded peptides (Desai and Kulkarni-Kale, 2014; Ogishi and Yotsuyanagi, 2019; Peters et al., 2020). The high degree of mutational plasticity of NS3p suggests that it would be amenable to such an approach (López-Labrador et al., 2008; Söderholm and Sällberg, 2006; Vallet et al., 2011).

In summary, we have introduced SNIP, a high-performance drug-regulated CAR platform that utilizes an FDA-approved small molecule to enable remote control and a generalizable molecular architecture that does not perturb CAR function. We demonstrated efficacy and safety of SNIP in ten different mouse models including four orthotopic solid tumor models targeting three different antigens and enhanced potency and safety of SNIP CARs compared with constitutive CARs. These studies provide foundational work poised for clinical translation to improve the safety, efficacy, and broader dissemination of CAR-T therapy.

Limitations of the study

Although we have demonstrated enhanced efficacy of SNIP CAR-T cells in NSG mice, immunogenicity of the virally derived NS3p could lead to limited T cell persistence and diminished activity. In addition, long-term functionality of SNIP CAR-T cells could not be assessed due to limitations of xenograft models for adoptively transferred T cell experiments (i.e., development of GVHD). Clinical studies are needed to assess the long-term functionality and immunogenicity of SNIP CAR-T cells. Moreover, GPV dosing strategies may not translate clinically owing to differences in PK of GPV between mice and humans and will need to be determined in clinical trials.

STAR★METHODS

Detailed methods are provided in the online version of this paper and include the following:

- KEY RESOURCES TABLE
- RESOURCE AVAILABILITY
  - Lead contact
  - Materials availability
  - Data and code availability
- EXPERIEMENTAL MODEL AND SUBJECT DETAILS
  - Cell lines

(B) 1 × 10^6 Nalm6-ROR1 leukemia cells, corresponding to the C5 cell line in Figure S7B, were engrafted in NSG mice by tail vein injection. 10 × 10^6 SNIP ROR1(F).28z CAR, constitutive ROR1(F).28z CAR, or mock T cells were administered by tail vein injection at day 1 post-tumor engraftment and an additional dose at day 7 for the SNIP and mock groups. Mice in the SNIP ROR1(F).28z ON_{TW} group were given 25 mg/kg doses of GPV and 2.5mg/kg RTV by oral gavage once per day. Treatment-related toxicities were monitored by weight change. Data are mean ± SEM.

(C) Tumor progression was monitored by BLI of Nalm6-ROR1 leukemia cells. Data are mean ± SEM.

(D) Survival curves of mice shown in (C). Survival curves were compared by the log-rank Mantel-Cox test, ****$p \leq 0.0001$.

(E) CD3 immunohistochemical staining of lungs from mice treated with ROR1(F).28z CAR-T cells (left) or SNIP ROR1(F).28z ON_{TW} CAR-T cells (right). Dashed rectangles indicate inset field of view. Black arrow in 2.5× micrograph indicates edematous region surrounding a blood vessel. See also Figure S7.

Please cite this article in press as: Labanieh et al., Enhanced safety and efficacy of protease-regulated CAR-T cell receptors, Cell (2022), https://doi.org/10.1016/j.cell.2022.03.041

SUPPLEMENTAL INFORMATION

Supplemental information can be found online at https://doi.org/10.1016/j.cell.2022.03.041.

ACKNOWLEDGMENTS

This work was supported by the National Institutes of Health (NIH) U54 CA232568-01 (to C.L.M. and E.W.W.), a St Baldrick's/Stand Up 2 Cancer Pediatric Dream Team Translational Cancer Research Grant (to C.L.M.), and NIH DP2 CA272092 (to R.G.M.). Stand Up 2 Cancer is a program of the Entertainment Industry Foundation administered by the American Association for Cancer Research. C.L.M., R.G.M., H.Y.C., A.T.S., E.W.W., and L.L. are members of the Parker Institute for Cancer Immunotherapy, which supports the Stanford University Cancer Immunotherapy Program. The work was also supported by a research grant from Lyell Immunopharma (to C.L.M.) and the Virginia and D.K. Ludwig Fund for Cancer Research (to C.L.M.). This work was supported by U01CA260852 (to A.T.S.) and a Technology Impact Award from the Cancer Research Institute (to A.T.S.). L.L. was supported by a Siebel Scholars Fellowship, Stanford Graduate Fellowship, and a National Science Foundation Graduate Research Fellowship (DGE-1656518). J.T. is supported by German Cancer Aid (Deutsche Krebshilfe) grant no. P-91650709. The authors acknowledge Elias Godoy and the Stanford Veterinary Service Center for mouse necropsy and Stanford Animal Histology Services (AHS) for histology sample processing. The authors thank Jing Huang for technical assistance with mouse experiments. H.Y.C. is an investigator of the Howard Hughes Medical Institute.

AUTHOR CONTRIBUTIONS

L.L., R.G.M., and C.L.M. conceived the idea of the study and designed experiments. L.L., R.G.M., D.K., E.S., J.G.V.-M., K.Z.B.P., J.H.H., M.M., P.X., T.M., J.T., N.M., S.A.Y.-H., C.J.F., and S.H. performed experiments and acquired data. L.L., R.G.M., D.K., E.S., J.G.V.-M., E.W.W., K.R.P., A.T.S., H.Y.C., and C.L.M. analyzed data and interpreted results. M.Z.L. advised on the design of SNIP. C.L.M. and J.R.C. supervised the work. L.L., R.G.M., E.S., J.R.C., and C.L.M. wrote the manuscript with feedback from all authors.

DECLARATION OF INTERESTS

L.L., R.G.M., M.Z.L., and C.L.M. are coinventors on a patent related to this work. C.L.M. is a cofounder of Lyell Immunopharma, Syncopation Life Sciences, and Link Cell Therapies, which are developing CAR-based therapies, and consults for Lyell, NeoImmune Tech, Apricity, Nektar, Immatics, Ensoma, Mammoth, Glaxo Smith Kline, and Bristol Myers Squibb. L.L., R.G.M., E.S., and E.W.W. are consultants for and hold equity in Lyell Immunopharma. L.L. is a cofounder of, consults for, and holds equity in Syncopation Life Sciences. R.G.M. is a cofounder of, consults for, and holds equity in Syncopation Life Sciences and Link Cell Therapies. R.G.M. is a consultant for Illumina Radiopharmaceuticals, NKarta, ImmunAI, Arovella Therapeutics, Zai Lab, and Aptorum Group. R.G.M. serves on the Data and Safety Monitoring Board for Fate Therapeutics. J.T. is a consultant for Dorian Therapeutics. E.W.W. consults for and holds equity in VISTAN Health. A.T.S. is a founder of Immunai and Cartography Biosciences and receives research funding from Arsenal Biosciences, Allogene Therapeutics, and 10x Genomics. K.R.P. is a cofounder and employee of Cartography Biosciences. H.Y.C. is a cofounder of Accent Therapeutics, Boundless Bio, and Cartography Biosciences and is an advisor to 10x Genomics, Arsenal Biosciences, and Spring Discovery. J.R.C. is a cofounder and equity holder of Trapeze Therapeutics, Combangio, and Virsti Therapeutics; he has financial interests in Aravive, Xyence Therapeutics, and Syncopation Life Sciences; and he is a member of the Board of Directors of Ligand Pharmaceuticals and Revel Pharmaceuticals. S.A.Y.-H. is a consultant for Trapeze Therapeutics and Xyence Therapeutics.

INCLUSION AND DIVERSITY

We worked to ensure diversity in experimental samples through the selection of the cell lines. We worked to ensure diversity in experimental samples through the selection of the genomic datasets. One or more of the authors of this paper self-identifies as an underrepresented ethnic minority in science. One or more of the authors of this paper self-identifies as a member of the LGBTQ+ community.

Received: January 13, 2021
Revised: January 4, 2022
Accepted: March 29, 2022
Published: April 27, 2022

REFERENCES

Adachi, K., Kano, Y., Nagai, T., Okuyama, N., Sakoda, Y., and Tamada, K. (2018). IL-7 and CCL19 expression in CAR-T cells improves immune cell infiltration and CAR-T cell survival in the tumor. Nat. Biotechnol. *36*, 346–351.

Ali, N., Flutter, B., Sanchez Rodriguez, R., Sharif-Paghaleh, E., Barber, L.D., Lombardi, G., and Nestle, F.O. (2012). Xenogeneic graft-versus-host-disease in NOD-scid IL-2Rγnull mice display a T-effector memory phenotype. PLoS One *7*, e44219.

Ali, S.A., Shi, V., Maric, I., Wang, M., Stroncek, D.F., Rose, J.J., Brudno, J.N., Stetler-Stevenson, M., Feldman, S.A., Hansen, B.G., et al. (2016). T cells expressing an anti-B-cell maturation antigen chimeric antigen receptor cause remissions of multiple myeloma. Blood *128*, 1688–1700.

Belkina, A.C., Ciccolella, C.O., Anno, R., Halpert, R., Spidlen, J., and Snyder-Cappione, J.E. (2019). Automated optimized parameters for T-distributed stochastic neighbor embedding improve visualization and analysis of large datasets. Nat. Commun. *10*, 5415.

Benjamin, R., Graham, C., Yallop, D., Jozwik, A., Mirci-Danicar, O.C., Lucchini, G., Pinner, D., Jain, N., Kantarjian, H., Boissel, N., et al. (2020). Genome-edited, donor-derived allogeneic anti-CD19 chimeric antigen receptor T cells in paediatric and adult B-cell acute lymphoblastic leukaemia: results of two phase 1 studies. Lancet *396*, 1885–1894.

Brudno, J.N., and Kochenderfer, J.N. (2019). Recent advances in CAR T-cell toxicity: mechanisms, manifestations and management. Blood Rev. *34*, 45–55.

Please cite this article in press as: Labanieh et al., Enhanced safety and efficacy of protease-regulated CAR-T cell receptors, Cell (2022), https://doi.org/10.1016/j.cell.2022.03.041

Brudno, J.N., Maric, I., Hartman, S.D., Rose, J.J., Wang, M., Lam, N., Stetler-Stevenson, M., Salem, D., Yuan, C., Pavletic, S., et al. (2018). T cells genetically modified to express an anti–B-cell maturation antigen chimeric antigen receptor cause remissions of poor-prognosis relapsed multiple myeloma. J. Clin. Oncol. *36*, 2267–2280.

Caro, L., Wenning, L., Guo, Z., Fraser, I.P., Fandozzi, C., Talaty, J., Panebianco, D., Ho, M., Uemura, N., Reitmann, C., et al. (2017). Effect of hepatic impairment on the pharmacokinetics of Grazoprevir, a hepatitis C virus protease inhibitor. Antimicrob. Agents Chemother. *61*, e00813, e00817.

Cho, J.H., Collins, J.J., and Wong, W.W. (2018). Universal chimeric antigen receptors for multiplexed and logical control of T cell responses. Cell *173*, 1426–1438.e11.

Chow, S.C. (2014). Adaptive clinical trial design. Annu. Rev. Med. *65*, 405–415.

Chu, J., Oh, Y., Sens, A., Ataie, N., Dana, H., Macklin, J.J., Laviv, T., Welf, E.S., Dean, K.M., Zhang, F., et al. (2016). A bright cyan-excitable orange fluorescent protein facilitates dual-emission microscopy and enhances bioluminescence imaging in vivo. Nat. Biotechnol. *34*, 760–767.

Chung, H.K., Jacobs, C.L., Huo, Y., Yang, J., Krumm, S.A., Plemper, R.K., Tsien, R.Y., and Lin, M.Z. (2015). Tunable and reversible drug control of protein production via a self-excising degron. Nat. Chem. Biol. *11*, 713–720.

Darowski, D., Kobold, S., Jost, C., and Klein, C. (2019). Combining the best of two worlds: highly flexible chimeric antigen receptor adaptor molecules (CAR-adaptors) for the recruitment of chimeric antigen receptor T cells. mAbs *11*, 621–631.

DeRenzo, C., and Gottschalk, S. (2019). Genetic modification strategies to enhance CAR T cell persistence for patients with solid tumors. Front. Immunol. *10*, 218.

Desai, D.V., and Kulkarni-Kale, U. (2014). T-cell epitope prediction methods: an overview. Methods Mol. Biol. *1184*, 333–364.

Di Stasi, A., Tey, S.K., Dotti, G., Fujita, Y., Kennedy-Nasser, A., Martinez, C., Straathof, K., Liu, E., Durett, A.G., Grilley, B., et al. (2011). Inducible apoptosis as a safety switch for adoptive cell therapy. N. Engl. J. Med. *365*, 1673–1683.

Diaconu, I., Ballard, B., Zhang, M., Chen, Y., West, J., Dotti, G., and Savoldo, B. (2017). Inducible caspase-9 selectively modulates the toxicities of CD19-specific chimeric antigen receptor-modified T cells. Mol. Ther. *25*, 580–592.

Erickson, A.L., Kimura, Y., Igarashi, S., Eichelberger, J., Houghton, M., Sidney, J., McKinney, D., Sette, A., Hughes, A.L., and Walker, C.M. (2001). The outcome of hepatitis C virus infection is predicted by escape mutations in epitopes targeted by cytotoxic T lymphocytes. Immunity *15*, 883–895.

Eyquem, J., Mansilla-Soto, J., Giavridis, T., van der Stegen, S.J.C., Hamieh, M., Cunanan, K.M., Odak, A., Gönen, M., and Sadelain, M. (2017). Targeting a CAR to the TRAC locus with CRISPR/Cas9 enhances tumour rejection. Nature *543*, 113–117.

Fan, S., Lee, B.L., and Lu, Y. (2020). A curve free Bayesian decision-theoretic design for phase Ia/Ib trials considering both safety and efficacy outcomes. Stat. Biosci. *12*, 146–166.

FDA (2016). Zepatier: pharmacology review(s) (U.S. Food and Drug Administration). https://www.accessdata.fda.gov/drugsatfda_docs/nda/2016/208261Orig1s000PharmR.pdf.

Feng, H.P., Caro, L., Fandozzi, C., Chu, X., Guo, Z., Talaty, J., Panebianco, D., Dunnington, K., Du, L., Hanley, W.D., et al. (2019). Pharmacokinetic interactions between the hepatitis C virus inhibitors elbasvir and grazoprevir and HIV protease inhibitors ritonavir, atazanavir, lopinavir, and Darunavir in healthy volunteers. Antimicrob. Agents Chemother. *63*, e02142, e02118.

Finck, R., Simonds, E.F., Jager, A., Krishnaswamy, S., Sachs, K., Fantl, W., Pe'er, D., Nolan, G.P., and Bendall, S.C. (2013). Normalization of mass cytometry data with bead standards. Cytometry A *83*, 483–494.

Fry, T.J., Shah, N.N., Orentas, R.J., Stetler-Stevenson, M., Yuan, C.M., Ramakrishna, S., Wolters, P., Martin, S., Delbrook, C., Yates, B., et al. (2018). CD22-targeted CAR T cells induce remission in B-ALL that is naive or resistant to CD19-targeted CAR immunotherapy. Nat. Med. *24*, 20–28.

Fucà, G., Reppel, L., Landoni, E., Savoldo, B., and Dotti, G. (2020). Enhancing chimeric antigen receptor T-cell efficacy in solid tumors. Clin. Cancer Res. *26*, 2444–2451.

Fujiwara, K., Tsunei, A., Kusabuka, H., Ogaki, E., Tachibana, M., and Okada, N. (2020). Hinge and transmembrane domains of chimeric antigen receptor regulate receptor expression and signaling threshold. Cells *9*, 1182.

Giordano-Attianese, G., Gainza, P., Gray-Gaillard, E., Cribioli, E., Shui, S., Kim, S., Kwak, M.J., Vollers, S., Corria Osorio, A.D.J., Reichenbach, P., et al. (2020). A computationally designed chimeric antigen receptor provides a small-molecule safety switch for T-cell therapy. Nat. Biotechnol. *38*, 426–432.

Good, C.R., Aznar, M.A., Kuramitsu, S., Samareh, P., Agarwal, S., Donahue, G., Ishiyama, K., Wellhausen, N., Rennels, A.K., Ma, Y., et al. (2021). An NK-like CAR T cell transition in CAR T cell dysfunction. Cell *184*, 6081–6100.e26.

Gross, G., and Eshhar, Z. (2016). Therapeutic potential of T cell chimeric antigen receptors (CARs) in cancer treatment: counteracting off-tumor toxicities for safe CAR T cell therapy. Annu. Rev. Pharmacol. Toxicol. *56*, 59–83.

Guest, R.D., Hawkins, R.E., Kirillova, N., Cheadle, E.J., Arnold, J., O'Neill, A., Irlam, J., Chester, K.A., Kemshead, J.T., Shaw, D.M., et al. (2005). The role of extracellular spacer regions in the optimal design of chimeric immune receptors: evaluation of four different scFvs and antigens. J. Immunother. *28*, 203–211.

Gust, J., Hay, K.A., Hanafi, L.-A., Li, D., Myerson, D., Gonzalez-Cuyar, L.F., Yeung, C., Liles, W.C., Wurfel, M., Lopez, J.A., et al. (2017). Endothelial activation and blood–brain barrier disruption in neurotoxicity after adoptive immunotherapy with CD19 CAR-T cells. Cancer Discov. *7*, 1404–1419.

Hafemeister, C., and Satija, R. (2019). Normalization and variance stabilization of single-cell RNA-seq data using regularized negative binomial regression. Genome Biol. *20*, 296.

Hennecke, S., and Cosson, P. (1993). Role of transmembrane domains in assembly and intracellular transport of the CD8 molecule. J. Biol. Chem. *268*, 26607–26612.

Hong, M., Clubb, J.D., and Chen, Y.Y. (2020). Engineering CAR-T cells for next-generation cancer therapy. Cancer Cell *38*, 473–488.

Hudecek, M., Lupo-Stanghellini, M.T., Kosasih, P.L., Sommermeyer, D., Jensen, M.C., Rader, C., and Riddell, S.R. (2013). Receptor affinity and extracellular domain modifications affect tumor recognition by ROR1-specific chimeric antigen receptor T cells. Clin. Cancer Res. *19*, 3153–3164.

Hughes, M.S., Yu, Y.Y.L., Dudley, M.E., Zheng, Z., Robbins, P.F., Li, Y., Wunderlich, J., Hawley, R.G., Moayeri, M., Rosenberg, S.A., and Morgan, R.A. (2005). Transfer of a TCR gene derived from a patient with a marked antitumor response conveys highly active T-cell effector functions. Hum. Gene Ther. *16*, 457–472.

Hurton, L.V., Singh, H., Najjar, A.M., Switzer, K.C., Mi, T., Maiti, S., Olivares, S., Rabinovich, B., Huls, H., Forget, M.A., et al. (2016). Tethered IL-15 augments antitumor activity and promotes a stem-cell memory subset in tumor-specific T cells. Proc. Natl. Acad. Sci. USA *113*, E7788–E7797.

Iwamoto, M., Björklund, T., Lundberg, C., Kirik, D., and Wandless, T.J. (2010). A general chemical method to regulate protein stability in the mammalian central nervous system. Chem. Biol. *17*, 981–988.

Jacobs, C.L., Badiee, R.K., and Lin, M.Z. (2018). StaPLs: versatile genetically encoded modules for engineering drug-inducible proteins. Nat. Methods *15*, 523–526.

Jacoby, E., Shahani, S.A., and Shah, N.N. (2019). Updates on CAR T-cell therapy in B-cell malignancies. Immunol. Rev. *290*, 39–59.

Jan, M., Scarfò, I., Larson, R.C., Walker, A., Schmidts, A., Guirguis, A.A., Gasser, J.A., Słabicki, M., Bouffard, A.A., Castano, A.P., et al. (2021). Reversible ON- and OFF-switch chimeric antigen receptors controlled by lenalidomide. Sci. Transl. Med. *13*, eabb6295.

Jena, B., Maiti, S., Huls, H., Singh, H., Lee, D.A., Champlin, R.E., and Cooper, L.J.N. (2013). Chimeric antigen receptor (CAR)-specific monoclonal antibody to detect CD19-specific T cells in clinical trials. PLoS One *8*, e57838.

Juillerat, A., Tkach, D., Busser, B.W., Temburni, S., Valton, J., Duclert, A., Poirot, L., Depil, S., and Duchateau, P. (2019). Modulation of chimeric antigen

Please cite this article in press as: Labanieh et al., Enhanced safety and efficacy of protease-regulated CAR-T cell receptors, Cell (2022), https://doi.org/10.1016/j.cell.2022.03.041

receptor surface expression by a small molecule switch. BMC Biotechnol. *19*, 44.

Jung, I.Y., Kim, Y.Y., Yu, H.S., Lee, M., Kim, S., and Lee, J. (2018). CRISPR/Cas9-mediated knockout of DGK improves antitumor activities of human T cells. Cancer Res. *78*, 4692–4703.

Kagoya, Y., Tanaka, S., Guo, T., Anczurowski, M., Wang, C.H., Saso, K., Butler, M.O., Minden, M.D., and Hirano, N. (2018). A novel chimeric antigen receptor containing a JAK-STAT signaling domain mediates superior antitumor effects. Nat. Med. *24*, 352–359.

Kamiya, T., Wong, D., Png, Y.T., and Campana, D. (2018). A novel method to generate T-cell receptor-deficient chimeric antigen receptor T cells. Blood Adv. *2*, 517–528.

Labanieh, L., Majzner, R.G., and Mackall, C.L. (2018). Programming CAR-T cells to kill cancer. Nat. Biomed. Eng. *2*, 377–391.

Lai, V.C.H., Zhong, W., Skelton, A., Ingravallo, P., Vassilev, V., Donis, R.O., Hong, Z., and Lau, J.Y.N. (2000). Generation and characterization of a hepatitis C virus NS3 protease-dependent bovine viral diarrhea virus. J. Virol. *74*, 6339–6347.

Lamers, C.H.J., Sleijfer, S., Van Steenbergen, S., Van Elzakker, P., Van Krimpen, B., Groot, C., Vulto, A., Den Bakker, M., Oosterwijk, E., Debets, R., and Gratama, J.W. (2013). Treatment of metastatic renal cell carcinoma with CAIX CAR-engineered T cells: clinical evaluation and management of on-target toxicity. Mol. Ther. *21*, 904–912.

Lee, D.W., Kochenderfer, J.N., Stetler-Stevenson, M., Cui, Y.K., Delbrook, C., Feldman, S.A., Fry, T.J., Orentas, R., Sabatino, M., Shah, N.N., et al. (2015). T cells expressing CD19 chimeric antigen receptors for acute lymphoblastic leukaemia in children and young adults: a phase 1 dose-escalation trial. Lancet *385*, 517–528.

Leung, W.H., Gay, J., Martin, U., Garrett, T.E., Horton, H.M., Certo, M.T., Blazar, B.R., Morgan, R.A., Gregory, P.D., Jarjour, J., and Astrakhan, A. (2019). Sensitive and adaptable pharmacological control of CAR T cells through extracellular receptor dimerization. JCI Insight *5*, e124430.

Long, A.H., Haso, W.M., Shern, J.F., Wanhainen, K.M., Murgai, M., Ingaramo, M., Smith, J.P., Walker, A.J., Kohler, M.E., Venkateshwara, V.R., et al. (2015). 4-1BB costimulation ameliorates T cell exhaustion induced by tonic signaling of chimeric antigen receptors. Nat. Med. *21*, 581–590.

López-Labrador, F.X., Moya, A., and Gonzàlez-Candelas, F. (2008). Mapping natural polymorphisms of hepatitis C virus NS3/4A protease and antiviral resistance to inhibitors in worldwide isolates. Antivir. Ther. *13*, 481–494.

Lynn, R.C., Weber, E.W., Sotillo, E., Gennert, D., Xu, P., Good, Z., Anbunathan, H., Lattin, J., Jones, R., Tieu, V., et al. (2019). C-Jun overexpression in CAR T cells induces exhaustion resistance. Nature *576*, 293–300.

Mackall, C.L., Hakim, F.T., and Gress, R.E. (1997). Restoration of T-cell homeostasis after T-cell depletion. Semin. Immunol. *9*, 339–346.

MacParland, S.A., Liu, J.C., Ma, X.Z., Innes, B.T., Bartczak, A.M., Gage, B.K., Manuel, J., Khuu, N., Echeverri, J., Linares, I., et al. (2018). Single cell RNA sequencing of human liver reveals distinct intrahepatic macrophage populations. Nat. Commun. *9*, 4383.

Madissoon, E., Wilbrey-Clark, A., Miragaia, R.J., Saeb-Parsy, K., Mahbubani, K.T., Georgakopoulos, N., Harding, P., Polanski, K., Huang, N., Nowicki-Osuch, K., et al. (2019). ScRNA-seq assessment of the human lung, spleen, and esophagus tissue stability after cold preservation. Genome Biol *21*, 1.

Majzner, R.G., and Mackall, C.L. (2019). Clinical lessons learned from the first leg of the CAR T cell journey. Nat. Med. *25*, 1341–1355.

Majzner, R.G., Rietberg, S.P., Sotillo, E., Dong, R., Vachharajani, V.T., Labanieh, L., Myklebust, J.H., Kadapakkam, M., Weber, E.W., Tousley, A.M., et al. (2020). Tuning the antigen density requirement for car T-cell activity. Cancer Discov. *10*, 702–723.

Majzner, R.G., Theruvath, J.L., Nellan, A., Heitzeneder, S., Cui, Y., Mount, C.W., Rietberg, S.P., Linde, M.H., Xu, P., Rota, C., et al. (2019). CAR T cells targeting B7-H3, a pan-cancer antigen, demonstrate potent preclinical activity against pediatric solid tumors and brain tumors. Clin. Cancer Res. *25*, 2560–2574.

Maude, S.L., Laetsch, T.W., Buechner, J., Rives, S.A., Boyer, M., Bittencourt, H., Bader, P., Verneris, M.R., Stefanski, H.E., Myers, G.D., et al. (2018). Tisagenlecleucel in children and young adults with B-cell lymphoblastic leukemia. N. Engl. J. Med. *378*, 439–448.

Mei, H.E., Leipold, M.D., Schulz, A.R., Chester, C., and Maecker, H.T. (2015). Barcoding of live human peripheral blood mononuclear cells for multiplexed mass cytometry. J. Immunol. *194*, 2022–2031.

Meyer-Olson, D., Shoukry, N.H., Brady, K.W., Kim, H., Olson, D.P., Hartman, K., Shintani, A.K., Walker, C.M., and Kalams, S.A. (2004). Limited T cell receptor diversity of HCV-specific T cell responses is associated with CTL escape. J. Exp. Med. *200*, 307–319.

Milone, M.C., and Bhoj, V.G. (2018). The pharmacology of T cell therapies. Mol. Ther. Methods Clin. Dev. *8*, 210–221.

Mootha, V.K., Lindgren, C.M., Eriksson, K.F., Subramanian, A., Sihag, S., Lehar, J., Puigserver, P., Carlsson, E., Ridderstråle, M., Laurila, E., et al. (2003). PGC-1alpha-responsive genes involved in oxidative phosphorylation are coordinately downregulated in human diabetes. Nat. Genet. *34*, 267–273.

Mount, C.W., Majzner, R.G., Sundaresh, S., Arnold, E.P., Kadapakkam, M., Haile, S., Labanieh, L., Hulleman, E., Woo, P.J., Rietberg, S.P., et al. (2018). Potent antitumor efficacy of anti-GD2 CAR T cells in H3-K27M+ diffuse midline gliomas-K27M+ diffuse midline gliomas letter. Nat. Med. *24*, 572–579.

Mueller, K.T., Waldron, E., Grupp, S.A., Levine, J.E., Laetsch, T.W., Pulsipher, M.A., Boyer, M.W., August, K.J., Hamilton, J., Awasthi, R., et al. (2018). Clinical Pharmacology of Tisagenlecleucel in B-cell acute lymphoblastic leukemia. Clin. Cancer Res. *24*, 6175–6184.

Murty, S., Labanieh, L., Murty, T., Gowrishankar, G., Haywood, T., Alam, I.S., Beinat, C., Robinson, E., Aalipour, A., Klysz, D.D., et al. (2020). PET reporter gene imaging and ganciclovir-mediated ablation of chimeric antigen receptor T cells in solid tumors. Cancer Res. *80*, 4731–4740.

Nathwani, A., Satyen, G., and Della Peruta, M. (2019). WO 2019/008378 Al - ROR1 CAR T-cells (WIPO). https://patentscope.wipo.int/search/en/detail.jsf?docId=WO2019008378.

Neelapu, S.S., Locke, F.L., Bartlett, N.L., Lekakis, L.J., Miklos, D.B., Jacobson, C.A., Braunschweig, I., Oluwole, O.O., Siddiqi, T., Lin, Y., et al. (2017a). Axicabtagene Ciloleucel CAR T-cell therapy in refractory large B-cell lymphoma. N. Engl. J. Med. *377*, 2531–2544.

Neelapu, S.S., Tummala, S., Kebriaei, P., Wierda, W., Gutierrez, C., Locke, F.L., Komanduri, K.V., Lin, Y., Jain, N., Daver, N., et al. (2018). Chimeric antigen receptor T-cell therapy—assessment and management of toxicities. Nat. Rev. Clin. Oncol. *15*, 47–62.

Ogishi, M., and Yotsuyanagi, H. (2019). Quantitative prediction of the landscape of T cell epitope immunogenicity in sequence space. Front. Immunol. *10*, 827.

Onoe, T., Kalscheuer, H., Chittenden, M., Zhao, G., Yang, Y.-G., and Sykes, M. (2010). Homeostatic expansion and phenotypic conversion of human T cells depend on peripheral interactions with APCs. J. Immunol. *184*, 6756–6765.

Paszkiewicz, P.J., Fräßle, S.P., Srivastava, S., Sommermeyer, D., Hudecek, M., Drexler, I., Sadelain, M., Liu, L., Jensen, M.C., Riddell, S.R., and Busch, D.H. (2016). Targeted antibody-mediated depletion of murine CD19 CAR T cells permanently reverses B cell aplasia. J. Clin. Invest. *126*, 4262–4272.

Patro, R., Duggal, G., Love, M.I., Irizarry, R.A., and Kingsford, C. (2017). Salmon provides fast and bias-aware quantification of transcript expression. Nat. Methods *14*, 417–419.

Peters, B., Nielsen, M., and Sette, A. (2020). T cell epitope predictions. Annu. Rev. Immunol. *38*, 123–145.

Philip, B., Kokalaki, E., Mekkaoui, L., Thomas, S., Straathof, K., Flutter, B., Marin, V., Marafioti, T., Chakraverty, R., Linch, D., et al. (2014). A highly compact epitope-based marker/suicide gene for easier and safer T-cell therapy. Blood *124*, 1277–1287.

Raje, N., Berdeja, J., Lin, Y., Siegel, D., Jagannath, S., Madduri, D., Liedtke, M., Rosenblatt, J., Maus, M.V., Turka, A., et al. (2019). Anti-BCMA CAR T-cell therapy bb2121 in relapsed or refractory multiple myeloma. N. Engl. J. Med. *380*, 1726–1737.

Please cite this article in press as: Labanieh et al., Enhanced safety and efficacy of protease-regulated CAR-T cell receptors, Cell (2022), https://doi.org/10.1016/j.cell.2022.03.041

Raredon, M.S.B., Adams, T.S., Suhail, Y., Schupp, J.C., Poli, S., Neumark, N., Leiby, K.L., Greaney, A.M., Yuan, Y., Horien, C., et al. (2019). Single-cell connectomic analysis of adult mammalian lungs. Sci. Adv. *5*, eaaw3851.

Ren, J., Zhang, X., Liu, X., Fang, C., Jiang, S., June, C.H., and Zhao, Y. (2017). A versatile system for rapid multiplex genome-edited CAR T cell generation. Oncotarget *8*, 17002–17011.

Ren, J., and Zhao, Y. (2017). Advancing chimeric antigen receptor T cell therapy with CRISPR/Cas9. Protein Cell *8*, 634–643.

Richman, S.A., Wang, L.C., Moon, E.K., Khire, U.R., Albelda, S.M., and Milone, M.C. (2020). Ligand-induced degradation of a CAR permits reversible remote control of CAR T cell activity *in vitro* and *in vivo*. Mol. Ther. *28*, 1600–1613.

Rockstroh, J.K., Nelson, M., Katlama, C., Lalezari, J., Mallolas, J., Bloch, M., Matthews, G.V., Saag, M.S., Zamor, P.J., Orkin, C., et al. (2015). Efficacy and safety of grazoprevir (MK-5172) and elbasvir (MK-8742) in patients with hepatitis C virus and HIV co-infection (C-EDGE CO-INFECTION): A non-randomised, open-label trial. Lancet HIV *2*, e319–e327.

Rodgers, D.T., Mazagova, M., Hampton, E.N., Cao, Y., Ramadoss, N.S., Hardy, I.R., Schulman, A., Du, J., Wang, F., Singer, O., et al. (2016). Switch-mediated activation and retargeting of CAR-T cells for B-cell malignancies. Proc. Natl. Acad. Sci. USA *113*, E459–E468.

Sakemura, R., Terakura, S., Watanabe, K., Julamanee, J., Takagi, E., Miyao, K., Koyama, D., Goto, T., Hanajiri, R., Nishida, T., et al. (2016). A tet-on inducible system for controlling CD19-chimeric antigen receptor expression upon drug administration. Cancer Immunol. Res. *4*, 658–668.

Salter, A.I., Ivey, R.G., Kennedy, J.J., Voillet, V., Rajan, A., Alderman, E.J., Voytovich, U.J., Lin, C., Sommermeyer, D., Liu, L., et al. (2018). Phosphoproteomic analysis of chimeric antigen receptor signaling reveals kinetic and quantitative differences that affect cell function. Sci. Signal. *11*, eaat6753.

Salzer, B., Schueller, C.M., Zajc, C.U., Peters, T., Schoeber, M.A., Kovacic, B., Buri, M.C., Lobner, E., Dushek, O., Huppa, J.B., et al. (2020). Engineering AvidCARs for combinatorial antigen recognition and reversible control of CAR function. Nat. Commun. *11*, 4166.

Schmidts, A., and Maus, M.V. (2018). Making CAR T cells a solid option for solid tumors. Front. Immunol. *9*, 2593.

Schmidts, A., Wehrli, M., and Maus, M.V. (2021). Toward better understanding and management of CAR-T cell-associated toxicity. Annu. Rev. Med. *72*, 365–382.

Schulze Zur Wiesch, J., Lauer, G.M., Day, C.L., Kim, A.Y., Ouchi, K., Duncan, J.E., Wurcel, A.G., Timm, J., Jones, A.M., Mothe, B., et al. (2005). Broad repertoire of the CD4 + Th cell response in spontaneously controlled hepatitis C virus infection includes dominant and highly promiscuous epitopes. J. Immunol. *175*, 3603–3613.

Schuster, S.J., Bishop, M.R., Tam, C.S., Waller, E.K., Borchmann, P., McGuirk, J.P., Jäger, U., Jaglowski, S., Andreadis, C., Westin, J.R., et al. (2019). Tisagenlecleucel in adult relapsed or refractory diffuse large B-cell lymphoma. N. Engl. J. Med. *380*, 45–56.

Schuster, S.J., Svoboda, J., Chong, E.A., Nasta, S.D., Mato, A.R., Anak, Ö., Brogdon, J.L., Pruteanu-Malinici, I., Bhoj, V., Landsburg, D., et al. (2017). Chimeric antigen receptor T cells in refractory B-cell lymphomas. N. Engl. J. Med. *377*, 2545–2554.

Sen, G., Chakraborty, M., Foon, K.A., Reisfeld, R.A., and Bhattacharya-Chatterjee, M.B. (1998). Induction of IgG antibodies by an anti-idiotype antibody mimicking disialoganglioside GD2. J. Immunother. *21*, 75–83.

Shaner, N.C., Lambert, G.G., Chammas, A., Ni, Y., Cranfill, P.J., Baird, M.A., Sell, B.R., Allen, J.R., Day, R.N., Israelsson, M., et al. (2013). A bright monomeric green fluorescent protein derived from Branchiostoma lanceolatum. Nat. Methods *10*, 407–409.

Sheth, S.V., and Gauthier, J. (2020). Taming the beast: CRS and ICANS after CAR T-cell therapy for ALL. Bone Marrow Transplant. *56*, 552–566.

Shum, T., Omer, B., Tashiro, H., Kruse, R.L., Wagner, D.L., Parikh, K., Yi, Z., Sauer, T., Liu, D., Parihar, R., et al. (2017). Constitutive signaling from an engineered IL-7 receptor promotes durable tumor elimination by tumor redirected T-cells. Cancer Discov. *7*, 1238–1247.

Söderholm, J., and Sällberg, M. (2006). A complete mutational fitness map of the hepatitis C virus nonstructural 3 protease: relation to recognition by cytotoxic T lymphocytes. J. Infect. Dis. *194*, 1724–1728.

Spiegel, J.Y., Patel, S., Muffly, L., Hossain, N.M., Oak, J., Baird, J.H., Frank, M.J., Shiraz, P., Sahaf, B., Craig, J., et al. (2021). CAR T cells with dual targeting of CD19 and CD22 in adult patients with recurrent or refractory B cell malignancies: a phase 1 trial. Nat. Med. *27*, 1419–1431.

Srivastava, S., Salter, A.I., Liggitt, D., Yechan-Gunja, S., Sarvothama, M., Cooper, K., Smythe, K.S., Dudakov, J.A., Pierce, R.H., Rader, C., et al. (2019). Logic-gated ROR1 chimeric antigen receptor expression rescues T cell-mediated toxicity to normal tissues and enables selective tumor targeting. Cancer Cell *35*, 489–503.e8.

Stein, A.M., Grupp, S.A., Levine, J.E., Laetsch, T.W., Pulsipher, M.A., Boyer, M.W., August, K.J., Levine, B.L., Tomassian, L., Shah, S., et al. (2019). Tisagenlecleucel model-based cellular kinetic analysis of chimeric antigen receptor–T cells. CPT Pharmacometrics Syst. Pharmacol. *8*, 285–295.

Stewart, B.J., Ferdinand, J.R., Young, M.D., Mitchell, T.J., Loudon, K.W., Riding, A.M., Richoz, N., Frazer, G.L., Staniforth, J.U.L., Vieira Braga, F.A.V., et al. (2019). Spatiotemporal immune zonation of the human kidney. Science *365*, 1461–1466.

Su, Y., Walker, J.R., Park, Y., Smith, T.P., Liu, L.X., Hall, M.P., Labanieh, L., Hurst, R., Wang, D.C., Encell, L.P., et al. (2020). Novel NanoLuc substrates enable bright two-population bioluminescence imaging in animals. Nat. Methods *17*, 852–860.

Subramanian, A., Tamayo, P., Mootha, V.K., Mukherjee, S., Ebert, B.L., Gillette, M.A., Paulovich, A., Pomeroy, S.L., Golub, T.R., Lander, E.S., et al. (2005). Gene set enrichment analysis: a knowledge-based approach for interpreting genome-wide expression profiles. Proc. Natl. Acad. Sci. USA *102*, 15545–15550.

Tabula Muris Consortium; Overall Coordination; Logistical Coordination; Organ Collection and Processing; Library Preparation and Sequencing; Computational Data Analysis; Cell Type Annotation; Writing Group; Supplemental Text Writing Group; Principal investigators (2018). Single-cell transcriptomics of 20 mouse organs creates a Tabula Muris. Nature *562*, 367–372.

Tague, E.P., Dotson, H.L., Tunney, S.N., Sloas, D.C., and Ngo, J.T. (2018). Chemogenetic control of gene expression and cell signaling with antiviral drugs. Nat. Methods *15*, 519–522.

Tamada, K., Geng, D., Sakoda, Y., Bansal, N., Srivastava, R., Li, Z., and Davila, E. (2012). Redirecting gene-modified T cells toward various cancer types using tagged antibodies. Clin. Cancer Res. *18*, 6436–6445.

Thistlethwaite, F.C., Gilham, D.E., Guest, R.D., Rothwell, D.G., Pillai, M., Burt, D.J., Byatte, A.J., Kirillova, N., Valle, J.W., Sharma, S.K., et al. (2017). The clinical efficacy of first-generation carcinoembryonic antigen (CEACAM5)-specific CAR T cells is limited by poor persistence and transient pre-conditioning-dependent respiratory toxicity. Cancer Immunol. Immunother. *66*, 1425–1436.

Tirosh, I., Izar, B., Prakadan, S.M., Wadsworth, M.H., Treacy, D., Trombetta, J.J., Rotem, A., Rodman, C., Lian, C., Murphy, G., et al. (2016). Dissecting the multicellular ecosystem of metastatic melanoma by single-cell RNA-seq. Science *352*, 189–196.

Travaglini, K.J., Nabhan, A.N., Penland, L., Sinha, R., Gillich, A., Sit, R.V., Chang, S., Conley, S.D., Mori, Y., Seita, J., et al. (2020). A molecular cell atlas of the human lung from single-cell RNA sequencing. Nature *587*, 619–625.

Vallet, S., Viron, F., Henquell, C., Le Guillou-Guillemette, H., Lagathu, G., Abravanel, F., Trimoulet, P., Soussan, P., Schvoerer, E., Rosenberg, A., et al. (2011). NS3 protease polymorphism and natural resistance to protease inhibitors in French patients infected with HCV genotypes 1–5. Antivir. Ther. *16*, 1093–1102.

Wang, M., Munoz, J., Goy, A., Locke, F.L., Jacobson, C.A., Hill, B.T., Timmerman, J.M., Holmes, H., Jaglowski, S., Flinn, I.W., et al. (2020). KTE-X19 CAR T-cell therapy in relapsed or refractory mantle-cell lymphoma. N. Engl. J. Med. *382*, 1331–1342.

Please cite this article in press as: Labanieh et al., Enhanced safety and efficacy of protease-regulated CAR-T cell receptors, Cell (2022), https://doi.org/10.1016/j.cell.2022.03.041

Wang, Y., Jiang, H., Luo, H., Sun, Y., Shi, B., Sun, R., and Li, Z. (2019). An IL-4/21 inverted cytokine receptor improving CAR-T cell potency in immunosuppressive solid-tumor microenvironment. Front. Immunol. *10*, 1691.

Weber, E.W., Lynn, R.C., Parker, K.R., Anbunathan, H., Lattin, J., Sotillo, E., Good, Z., Malipatlolla, M., Xu, P., Vandris, P., et al. (2020). Transient "rest" induces functional reinvigoration and epigenetic remodeling in exhausted CAR-T cells. Preprint at bioRxiv. https://doi.org/10.1101/2020.01.26.920496.

Weber, E.W., Lynn, R.C., Sotillo, E., Lattin, J., Xu, P., and Mackall, C.L. (2019). Pharmacologic control of CAR-T cell function using dasatinib. Blood Adv *3*, 711–717.

Weber, E.W., Parker, K.R., Sotillo, E., Lynn, R.C., Anbunathan, H., Lattin, J., Good, Z., Belk, J.A., Daniel, B., Klysz, D., et al. (2021). Transient rest restores functionality in exhausted CAR-T cells through epigenetic remodeling. Science *372*, eaba1786.

Wherry, E.J., Ha, S.J., Kaech, S.M., Haining, W.N., Sarkar, S., Kalia, V., Subramaniam, S., Blattman, J.N., Barber, D.L., and Ahmed, R. (2007). Molecular signature of CD8+ T cell exhaustion during chronic viral infection. Immunity *27*, 670–684.

Wu, C.-Y., Roybal, K.T., Puchner, E.M., Onuffer, J., and Lim, W.A. (2015). Remote control of therapeutic T cells through a small molecule-gated chimeric receptor. Science *350*, aab4077.

Zajc, C.U., Dobersberger, M., Schaffner, I., Mlynek, G., Pühringer, D., Salzer, B., Djinović-Carugo, K., Steinberger, P., de Sousa Linhares, A., Yang, N.J., et al. (2020). A conformation-specific ON-switch for controlling CAR T cells with an orally available drug. Proc. Natl. Acad. Sci. USA *117*, 14926–14935.

Zhang, C., Hua, R., Cui, Y., Wang, S., Yan, H., Li, D., Zhang, Y., Tu, Z., Hao, P., Chen, X., et al. (2017a). Comprehensive mapping of antigen specific T cell responses in hepatitis C virus infected patients with or without spontaneous viral clearance. PLoS One *12*, e0171217.

Zhang, Y., Zhang, X., Cheng, C., Mu, W., Liu, X., Li, N., Wei, X., Liu, X., Xia, C., and Wang, H. (2017b). CRISPR-Cas9 mediated LAG-3 disruption in CAR-T cells. Front. Med. *11*, 554–562.

Please cite this article in press as: Labanieh et al., Enhanced safety and efficacy of protease-regulated CAR-T cell receptors, Cell (2022), https://doi.org/10.1016/j.cell.2022.03.041

STAR★METHODS

KEY RESOURCES TABLE

REAGENT or RESOURCE	SOURCE	IDENTIFIER
Antibodies		
Anti-14G2A idiotype antibody (Clone 1A7)	National Cancer Institute	(Sen et al., 1998)
Anti-FMC63 idiotype antibody	Lawrence Cooper, MD Anderson Cancer Center	(Jena et al., 2013)
Anti-CD3 zeta antibody (clone 4A12-F6)	abcam	Cat# ab188850; RRID: AB_2910545
Anti-p44/42 MAPK (Erk1/2) Antibody	Cell Signaling Technology	Cat# 9102S; RRID: AB_330744
BV605 Mouse Anti-Human CD62L (Clone DREG-56)	BD	Cat# 562719; RRID: AB_2744441
BV711 Mouse Anti-Human CD45RA (Clone HI100)	BD	Cat# 563733; RRID: AB_2738392
BUV395 Mouse Anti-Human CD4 (Clone SK3)	BD	Cat# 563550; RRID: AB_2738273
BD Horizon™ BUV805 Mouse Anti-Human CD8 (Clone SK1)	BD	Cat# 612889; RRID: AB_2833078
Brilliant Violet 421™ anti-human CD69 (Clone FN50)	BioLegend	Cat# 310930; RRID: AB_2561909
FITC anti-human CD39 (Clone A1)	BioLegend	Cat# 328206; RRID: AB_940425)
Brilliant Violet 711™ anti-human TNF-α Antibody	BioLegend	Cat# 502940; RRID: AB_2563885
Brilliant Violet 605™ anti-human CD107a (LAMP-1) (Clone H4A3)	BioLegend	Cat# 328634; RRID: AB_2563851
Anti-ROR1 monoclonal antibody (Clone F)	This paper	N/A
anti-CD45 (Clone HI30), PerCP-Cyanine5.5	Thermo Fisher	Cat# 45-0459-42; RRID: AB_10717530
CD223 (LAG-3) Monoclonal Antibody (Clone 3DS223H), PE	Thermo Fisher	Cat# 12-2239-42; RRID: AB_2572597
CD279 (PD-1) Monoclonal Antibody (Clone eBioJ105 (J105))	Thermo Fisher	Cat# 25-2799-42; RRID: AB_10853804
Brilliant Violet 421™ anti-human CD69 (Clone FN50)	BioLegend	Cat# 310930; RRID: AB_2561909)
Anti-CD45RO (clone UCHL1)	Fluidigm	Cat# 3149001B; RRID: AB_2687851
Anti-OX-40 (clone ACT35)	Fluidigm	Cat# 3150023B; RRID: AB_2905646
Anti-TIM-3 (clone F38-2E2)	Fluidigm	Cat# 3153008B; RRID: AB_2687644)
Anti-TIGIT (MBSA43)	Fluidigm	Cat# 3154016B; RRID: AB_2888926
Anti-CTLA-4 (clone 14D3)	Fluidigm	Cat# 3161004B; RRID: AB_2687649
Anti-Human Foxp3 (clone PCH101)	Fluidigm	Cat# 3162011A; RRID: AB_2687650
Anti-BTLA (clone MIH26)	Fluidigm	Cat# 3163009B; RRID: AB_2910546
Anti-Human CD223/LAG-3 (Clone 11C3C65)	Fluidigm	Cat# 3165037C; RRID: AB_2810971
Anti-CCR7 (clone G043H7)	Fluidigm	Cat# 3167009A; RRID: AB_2858236
Anti-IL-7R (clone A019D5)	Fluidigm	Cat# 3168017B; RRID: AB_2756425
Anti-4-1BB (clone 4B4-1)	Fluidigm	Cat# 3158013B; RRID: AB_2888927
Anti-PD-1 (clone EH12.2H7)	Fluidigm	Cat# 3174020B; RRID: AB_2868402
Anti-CD27 (clone 323)	BioLegend	Cat# 302839; RRID: AB_2562817
Purified anti-human CD69 MaxPar® Ready (Clone FN50)	BioLegend	Cat# 310939; RRID: AB_2562827
Anti-CD62L (clone DREG-56)	BioLegend	Cat# 304835; RRID: AB_2563758
Purified anti-human CD38 Maxpar® Ready Antibody (Clone HIT2)	BioLegend	Cat# 303535; RRID: AB_2562819
Purified anti-human CD45RA MaxPar® Ready (Clone HI100)	BioLegend	Cat# 304143; RRID: AB_2562822
Purified anti-human CD122 (IL-2Rβ) MaxPar® Ready (Clone TU27)	BioLegend	Cat# 339015; RRID: AB_2563712
Anti-CD39 (clone A1)	BioLegend	Cat# 328221; RRID: AB_2563747

(*Continued on next page*)

Please cite this article in press as: Labanieh et al., Enhanced safety and efficacy of protease-regulated CAR-T cell receptors, Cell (2022), https://doi.org/10.1016/j.cell.2022.03.041

Continued

REAGENT or RESOURCE	SOURCE	IDENTIFIER
Anti-T-bet (clone 4B10)	BioLegend	Cat# 3160010B; RRID: AB_2810251
Anti-CD25 (clone M-A251)	BD	Cat# 555430; ;RRID: AB_395824
Biological samples		
Buffy coats from healthy human subjects	Stanford Blood Center	N/A
Chemicals, peptides, and recombinant proteins		
Recombinant Human ROR1 Fc Chimera Protein, CF	R&D Systems	9490-RO-050
Recombinant Human B7-H3 Fc Chimera Protein, CF	R&D Systems	1027-B3-100
Recombinant Human ErbB2/Her2 Fc Chimera Protein, CF	R&D Systems	1129-ER-050
Recombinant Human IL-2	Peprotech	200-02-1mg
Cultrex Basement Membrane Extract, PathClear	R&D Systems	3432-005-01
Grazoprevir	Acme Bioscience Inc	Custom service
Grazoprevir Potassium Salt	Acme Bioscience Inc	Custom service
Ritonavir, 98%	Fisher Scientific	AC461220010
RetroNectin® Recombinant Human Fibronectin Fragment	Takara	T100B
Lipofectamine™ 2000 Transfection Reagent	Thermo Fisher	11668500
eBioscience™ Monensin Solution (1000X)	Thermo Fisher	00-4505-51
D-Luciferin Firefly, potassium salt	Fisher Scientific	L82201G
Cisplatin	Fluidigm	201064
Fixable Viability Dye eFluor™ 450	Thermo Fisher	65-0863-18
DNA intercalator	Fluidigm	201191B
Critical commercial assays		
REAlease® CD4/CD8 (TIL) MicroBead Kit, human	Miltenyi Biotec	130-121-561
Intracellular Fixation & Permeabilization Buffer Set Kit	Thermo Fisher	88-8824-00
Human IFN-γ ELISA MAX™ Deluxe	BioLegend	430104
Human IL-2 ELISA MAX™ Deluxe	BioLegend	431804
RosetteSep™ Human T Cell Enrichment Cocktail	STEMCELL Technologies	15061
SepMate™-50 Tubes	STEMCELL Technologies	85450
DyLight™ 650 Microscale Antibody Labeling Kit	Thermo Fisher	84536
Quantum™ Simply Cellular® anti-Human IgG	Bangs Laboratories	816 A
CellTrace™ Violet Cell Proliferation Kit, for flow cytometry	Thermo Fisher	C34557
Nano-Glo Luciferase Assay	Promega	N1120
Cell-ID 20-Plex Pd Barcoding Kit	Fluidigm	201060
EQ Four Element Calibration Beads	Fluidigm	201078
Deposited data		
Raw and analyzed data	This paper	GSE192998
LCMV mouse model, effector and memory T cell RNA-seq datasets	(Wherry et al., 2007)	GSE9650
HA CAR-T-exhaustion model, HA and CD19 CAR-T cell RNA-seq datasets	(Lynn et al., 2019)	GSE136891
Experimental models: Cell lines		
Nalm6-GL	(Majzner et al., 2019)	N/A
Nalm6-B7H3	(Majzner et al., 2019)	N/A
143B-GL	(Lynn et al., 2019)	N/A
MED8A-GL	This paper	N/A
Nalm6- B7H3 High	(Majzner et al., 2019)	N/A
CHLA255-GL	(Majzner et al., 2020)	N/A

(*Continued on next page*)

Please cite this article in press as: Labanieh et al., Enhanced safety and efficacy of protease-regulated CAR-T cell receptors, Cell (2022), https://doi.org/10.1016/j.cell.2022.03.041

Continued

REAGENT or RESOURCE	SOURCE	IDENTIFIER
MG63.3	(Majzner et al., 2019)	N/A
NALM6 ROR1 LINES	This paper	N/A
293GP	National Cancer Institute, Surgery Branch	N/A
293T	National Cancer Institute, Surgery Branch	N/A
Expi294 cells	Thermo Fisher	A14526
Experimental models: Organisms/strains		
NSG mice (NOD.Cg-Prkdc^{scid} Il2rgt^{m1Wjl}/SzJ)	Jackson Laboratory	005557
Recombinant DNA		
MSGV1	(Lynn et al., 2019)	N/A
RD 114	(Lynn et al., 2019)	N/A
pMDLg/pRRE	(Lynn et al., 2019)	N/A
pRSV-Rev	(Lynn et al., 2019)	N/A
pMD2.G (VSVg)	(Lynn et al., 2019)	N/A
pGreenFire1-NF-κB	System Biosciences	TR012PA-1
NF-κB Antares-P2A-mNG	This paper	N/A
pCS6-ZF(VEGFA)-StaPL(AI)-YFP-VPR	Michael Lin Lab, Stanford University	(Jacobs et al., 2018)
Software and algorithms		
DESeq2	Bioconductor	bioconductor.org
Salmon	Salmon	salmon.readthedocs.io/en/latest/salmon.html
clusterProfiler	Bioconductor	bioconductor.org
Scanpy v.1.4.3	scanpy	scanpy.readthedocs.io/en/stable/
Seurat Package	Satija Lab	satijalab.org/seurat/
R Studio v1.2.5042	R Studio	Rstudio.com
Living Image v4.7.4	PerkinElmer	Perkinelmer.com
FlowJo 10.7.1	FlowJo	Flowjo.com
Graphpad Prism	GraphPad Software	graphpad.com/scientific-software/prism
SnapGene v5.2.3	SnapGene	snapgene.com
Cell Ranger	10x GENOMICS	10xgenomics.com
BD FACSDiva	BD Biosciences	bdbiosciences.com
Incucyte ZOOM software	Sartorius	essenbioscience.com
Other		
Alzet Osmotic Pump model 2002	ALZET Osmotic Pumps	0000296
Dynabeads™ Human T-Expander CD3/CD28	Thermo Fisher	11141D
Protein A Sepharose	Thermo Fisher	101041
Helios	Fluidigm	N/A
Kimtron IC-225	KIMTRON	N/A
IVIS Spectrum imaging system	PerkinElmer	N/A
gentleMACS™ Dissociator	Miltenyi Biotec	130-093-235
Incucyte Zoom	Sartorius	essenbioscience.com
BD LSRFortessa™ X-20	BD Biosciences	N/A

RESOURCE AVAILABILITY

Lead contact

Requests for reagents, resources, and further information should be directed to and will be fulfilled by the lead contact, Crystal L. Mackall (cmackall@stanford.edu).

Please cite this article in press as: Labanieh et al., Enhanced safety and efficacy of protease-regulated CAR-T cell receptors, Cell (2022), https://doi.org/10.1016/j.cell.2022.03.041

CellPress
OPEN ACCESS

Materials availability

All resources and materials reported in this paper will be shared by the lead contact upon request.

Data and code availability

The RNa-seq and scRNa-seq datasets generated during this study are available at GEO: GSE192998 [https://www.ncbi.nlm.nih.gov/geo/query/acc.cgi?acc=GSE192998]. Details of the analysis are provided in the STAR Methods section. Any additional questions should be directed to and will be fulfilled by the lead contact.

EXPERIEMENTAL MODEL AND SUBJECT DETAILS

Cell lines

The Nalm6 B-ALL cell line was provided by David Barrett (Children's Hospital of Philadelphia) and retrovirally transduced to express GFP and firefly luciferase (N6-GL). Nalm6-GL was transduced with cDNA encoding human B7-H3 (Nalm6-B7H3) or human ROR1 (Nalm6-ROR1), and single cell clones were isolated from the transduced populations. 143B osteosarcoma cells (ATCC) were retrovirally transduced with GFP and luciferase (143B-GL). CHLA-255 neuroblastoma line was provided by Robert Seeger (Children's Hospital Los Angeles) and retrovirally transduced with GFP and firefly luciferase (CHLA-255). MG63.3 was provided by Chand Khanna (National Cancer Institute, National Institutes of Health) and retrovirally transduced with GFP and firefly luciferase (MG63.3-GL). MED8A-GL was provided by S. Chesier (Stanford University, Stanford, CA). The 293GP retroviral packaging line was provided by the Surgery Branch (National Cancer Institute, National Institutes of Health). Nalm6, 143B, MG63.3, and CHLA-255 were cultured in RPMI-1640 (Gibco). MED8A and 293GP were cultured in DMEM (Gibco). Cell line culture media was supplemented with 10% FBS, 10mM HEPES, 2mM L-glutamine, 100 U/mL penicillin, and 100μg/mL streptomycin (Gibco), with the exception of MED8A which was cultured in an additional 10% FBS (completed DMEM at 20% FBS). STR DNA profiling of all cell lines was conducted once per year (Genetica Cell Line testing). All cell lines were routinely tested for mycoplasma. Cell lines were cultured at 37 °C in a 5% CO_2 environment.

Animal models

NSG mice (NOD.Cg-Prkdc^{scid} Il2rgt^{m1Wjl}/SzJ) were purchased from the Jackson Laboratory and bred in house under Stanford University APLAC-approved protocols. Healthy male and female mice were used for *in vivo* experiments between 6 and 10 weeks old at tumor engraftment and were drug naïve, and not involved in previous procedures. Mice were house in sterile cages in a barrier facility at Stanford University with a 12-hour light/dark cycle. Veterinary Services Center (VSC) staff at Stanford University monitored the mice daily and were euthanized when mice manifested persistent hunched posture, persistent scruffy coat, paralysis, impaired mobility, greater than 20% weight loss, if tumors significantly interfered with normal bodily functions, or if they exceeded limits designated in APLAC-approved protocols. Per recommendation by VSC staff, mice with morbidities were supported with 500μL subcutaneous saline, diet gel (DietGel® 76A, ClearH2O), and wet chow.

Source of primary human T cells

Buffy coats from healthy donors were purchased from the Stanford Blood Center under an IRB-exempt-protocol. Primary human T cells were purified by negative selection using the RosetteSep Human T cell Enrichment kit (Stem Cell Technologies) and SepMate-50 tubes. T cells were cryopreserved at 1-2x10^7 cells per mL in CryoStor CS10 cryopreservation media (Stem Cell Technologies) until use.

METHOD DETAILS

Viral vector construction

All retroviral constructs were cloned into the MSGV1 retroviral vector (Hughes et al., 2005). B7H3.BBz was generated by fusing, from N to C terminus, a human GM-CSF leader sequence, scFv derived from MGA271 in the VH-VL orientation and $(GGGS)_3$ linker sequence, CD8α hinge and transmembrane sequence, and human 4-1BB and CD3ζ intracellular signaling domains. Cis SNIP scFv was generated by inserting a cis protease control module comprised of an HA-tag, 4A-4B cleavage site (DEMEECSQH), NS4a cofactor domain, and NS3(ai) protease into the B7H3.BBz vector between the scFv and CD8α hinge domain (Jacobs et al., 2018). Cis SNIP BBz was generated by inserting the cis protease control module into the B7H3.BBz vector between the CD8α transmembrane domain and the 4-1BB signaling domain. Trans SNIP BBz was expressed in bicistronic format using B7H3.BBz as the base vector. Briefly, a linker sequence containing 4A-4B cleavage site was integrated between the CD8α transmembrane domain and the 4-1BB signaling domain. The stop codon in the CD3ζ was replaced with a sequence containing a porcine teschovirus-1 2A (P2A) ribosomal skipping sequence, TCR- β leader sequence, RQR8 detection module containing epitopes for Qbend10 and rituximab antibodies, CD8α hinge, CD8α transmembrane domain, CD8α intracellular anchor domain, linker sequence (GSSSGNSSGGS), NS4A cofactor domain and NS3(ai) protease (Philip et al., 2014). SNIP cut site 1 refers to the Trans SNIP BBz with the 4a-4b sequence. SNIP cut site 2 and 3 were generated by replacing the 4A-4B site in Trans SNIP BBz with a 5A-5B (EDVVPCSMGS) and 4B-5A site (ECTTPCSGSWL), respectively. For transmembrane matching experiments, the CD8 TM refers to the CD8α hinge

Please cite this article in press as: Labanieh et al., Enhanced safety and efficacy of protease-regulated CAR-T cell receptors, Cell (2022), https://doi.org/10.1016/j.cell.2022.03.041

and transmembrane, whereas the CD28 TM refers to the CD28 hinge and transmembrane domain, which were cloned into the Trans SNIP BBz vector. GD2.BBz, HER2.BBz, and CD19.BBz were generated by cloning scFvs derived from 14G2A, 4D5, and FMC63 antibodies, respectively into the B7H3.BBz vector. CD19.28z was generated by replacing the 4-1BB domain in CD19.BBz with the intracellular signaling domain of human CD28. ROR1(R11).IgG4.BBz was generated as previously described (Srivastava et al., 2019). ROR1(F).28z and ROR1(F).BBz were generated by replacing the FMC63 scFv with the clone F scFv in the CD19.28z and CD19.BBz vectors, respectively (Nathwani et al., 2019). The *in vivo* T cell activation reporter was constructed by cloning a sequence containing Antares-P2A-mNeonGreen (NF-κB Antares-P2A-mNG) into the pGreenFire1-NF-κB lentiviral vector (System Biosciences) under the NF-κB responsive promoter (Chu et al., 2016; Shaner et al., 2013).

Virus production

Retroviral supernatant was packaged using 293GP cells and the RD114 envelope plasmid. In brief, 11μg RD114 and 22μg of the corresponding MSGV1 transfer plasmid were delivered to 293GP cells grown on 150mm poly-D-lysine dishes (Corning) to 80% confluency by transient transfection with Lipofectamine 2000 (Thermo Fisher). Media was replenished every 24 hours. Virus production was performed side-by-side for comparable CAR constructs. Retroviral supernatant was harvested 48 and 72-hour post transfection. Supernatant from replicate dishes were pooled, centrifuged to deplete cell debris, and stored at -80C until use. Third-generation, self-inactivating lentiviral supernatant was similarly produced with 293T cells using 7μg pMD2.G (VSVg) envelope, 18μg pMDLg/pRRE (Gag/Pol), 18μg pRSV-Rev, and 20μg the corresponding transfer plasmids.

CAR-T manufacturing

At Day 0, primary human T cells were thawed and activated with anti-CD3/CD28 Human T-Expander Dynabeads (Thermo Fisher) at a 3:1 bead to cell ratio. On Day 2 virus coated culture plates were prepared on non TC-treated 12-well plates that had been pre-coated with RetroNectin (Takara Bio) according to the manufacturer's instructions, by incubating with 1mL of retroviral supernatant ($2x10^7$-$5x10^7$ TU/mL) and centrifugation at 3200 RPM, 32 °C for two hours. The supernatant was subsequently aspirated off of the wells and $0.5x10^6$ T cells were added in 1mL of T cell media comprised of: AIM V (Thermo Fisher), 5% fetal bovine serum (FBS), 100 U/mL penicillin (Gibco), 100 mg/mL streptomycin (Gibco), 2 mM L-glutamine (Gibco), 10 mM HEPES (Gibco), and 100 U/mL rhIL-2 (Peprotech). After addition of the T cells, the plates were gently spun down at 1200 RPM for 2 min then incubated for 24hrs at 37°C 5% CO_2. This transduction process was repeated at Day 3. Dynabeads were removed on Day 4 by magnetic separation. Cells were maintained between 0.4 - $2x10^6$ cells/mL and expanded until Day 10.

Grazoprevir/ritonavir preparation and administration

For *in vitro* experiments, grazoprevir (Acme Bioscience, custom synthesis) was reconstituted in DMSO to 1000x stock solution and frozen at -80°C. For *in vivo* experiments, grazoprevir potassium salt (Acme Bioscience, custom synthesis) was reconstituted to 60mg/mL in 100% PEG 300 (Rigaku) by incubation in a 37°C water bath and vortexing. Ritonavir (ACROS Organic), which was used as a pharmacokinetic enhancer due to the short plasma half-life of GPV in mice (FDA, 2016; Feng et al., 2019), was similarly reconstituted to 60mg/mL using a 1:1 solution of propylene glycol (MP Biomedicals) and ethanol. Osmotic pumps (Alzet, model 2002) with a 0.5μL/hr release rate were filled with the indicated concentration of grazoprevir/ritonavir according to the manufacturer's instructions and primed in DPBS at 37°C 24 hours prior to implantation. Pumps were subcutaneously implanted in the right flank of mice 24hr prior to T cell administration. Oral formulations were prepared at the indicated concentration in gavage diluent (70% (v/v) PEG 300, 5% (w/v) sucrose (Sigma), and 5% (v/v) DPBS (Gibco)), aliquoted, and stored at -80°C. Drug was delivered to mice by oral gavage in a total volume of 100μL using 20 gauge 30mm feeding tubes (Instech). For in vivo studies, pumps were implanted 24hr prior to T cell administration. Mice were dosed with 50mg/kg GPV+25mg/kg RTV 2-3 times per day unless otherwise indicated such as the modified drug dosing scheme in the ROR1 toxicity models, where no pumps were implanted and drug was dosed at 25 mg/kg GPV + 2.5mg/kg RTV by oral gavage once per day.

Incucyte tumor killing assays and cytokine analysis

$5x10^4$ GFP or RFP-labeled tumor cells were cocultured with $5x10^4$ GFP CAR-T cells in 200μL RPMI supplemented with 10% FBS, 10mM HEPES, 2mM L-glutamine, 100 U/mL penicillin, and 100μg/mL streptomycin. Triplicate wells were plated in 96-well flat-bottom plates for each condition. Tumor fluorescence was monitored every 2-3 hours with a 10x objective using the Incucyte Zoom system (Essen Bioscience), housed in a cell culture incubator at 37°C and 5% CO_2, set to take 4 images per well at each time point. Total integrated GFP or RFP intensity was quantified using the Zoom software (Essen Bioscience). Data were normalized to the first timepoint and plotted as fold change in tumor fluorescence over time. For cytokine secretion analysis, cocultures were setup as above except in 96-well round bottom plates. After approximately 24 hours, plates were spun down to pellet cells and 100uL of supernatant was harvested and stored at -80°C until analysis. IFNγ and IL-2 levels in coculture supernatants were quantified by ELISA (Human ELISA MAX Deluxe, Biolegend) according to the manufacturer's instructions. Negative cytokine values were set to 0. Coculture experiments were setup using day 10 T cells, with the exception of On/Off kinetics experiments in Figures 1G and S1F, which were setup on Day 14.

Please cite this article in press as: Labanieh et al., Enhanced safety and efficacy of protease-regulated CAR-T cell receptors, Cell (2022), https://doi.org/10.1016/j.cell.2022.03.041

Immunoblotting

Whole-cell protein lysates were obtained in non-denaturing buffer as previously described (Lynn et al., 2019). Protein concentrations were estimated by Bio-Rad colorimetric assay. Immunoblotting was performed by loading 10 μg of protein onto 7.5% PAGE gels followed by transfer to PVF membranes. Signals were detected by enhanced chemiluminescence (Pierce) or with the Odyssey imaging system. The CD3-zeta (4A12-F6) primary antibody was purchased from Abcam. Total ERK1/2 (#9102) and GAPDH (#97166) antibodies were purchased from Cell Signaling and used as loading control. Images were cropped to exclude non-relevant gel lanes.

Expression and purification of the anti-ROR1 Clone F antibody

Clone F anti-ROR1 antibodies were expressed in full length human IgG1 format. Heavy chain and light chain sequences were ordered as gblock gene fragments (IDT) and individually cloned into the cytomegalovirus-driven adenoviral shuttle vector pAdd2 using standard Gibson assembly. Cloned expression vectors were transfected into Expi293 cells (Thermo Fisher, A14526) in a 1:1 weight ratio of heavy chain to light chain and expressed according to manufacturer's protocol. Antibody was purified from the supernatant using protein A affinity chromatography (Protein A Sepharose, Thermo Fisher, 101041). The purified antibody was fluorescently labeled with the DyLight 650 Microscale Antibody Labeling Kit (Thermo Fisher).

Generation of N6-ROR1 single-cell clones

Human ROR1 (UniProt ID Q01973) was cloned into the MSGV1 vector and used to transduce N6-GL cells. Briefly, dilutions of hROR1 retroviral supernatant were prepared from 1 to 1:100 and used to coat RetroNectin plates as described above. $5x10^5$ N6-GL cells were transduced per well for 48 hours. Cells were expanded for seven days, stained for ROR1 expression using 3μg/mL clone F antibody conjugated with DyLight 650, then FACS-sorted into bins according to expression levels using a FACSAria II SORP. N6-ROR1 cells were expanded for seven more days before single-cell cloning by limiting dilution into 96-well plates. Wells that contained cells were grown to dense cultures prior to analysis of ROR1 expression levels and further expansion.

Flow cytometry

Recombinant B7H3-, HER2-, and human ROR1-Fc (R&D systems) were used to detection B7H3, HER2, and ROR1 surface CAR, respectively. Likewise, anti-FMC63 and anti-14g2a idiotype antibodies were used to detect CD19 and GD2 CAR, respectively. CAR detection reagents were fluorescently labeled with the DyLight 650 Microscale Antibody Labeling Kit (Thermo Fisher). Surface CAR was stained by incubation with 3 μg/mL CAR detection reagents for 30min at 4C. Quantification of B7H3 surface molecules on cancer lines was performed using the Quantum™ Simply Cellular® anti-Human IgG kit (Bangs Laboratories, Inc.). All antibodies and detection reagents used in this study are listed in the key resources table. Flow cytometry was performed on a BD Fortessa instrument.

Bioluminescence imaging

Mice were administered either 200μL of 15 μg/mL D-luciferin or a 1:40 dilution of Nano-Glo substrate (Promega, diluted in DPBS) by intraperitoneal injection for firefly luciferase and Antares imaging, respectively. Images were acquired on an IVIS imaging system 5 min after injection using 30 sec exposures and medium binning. If saturated pixels were detected in the image, an additional image was acquired using the auto-expose setting. Total flux was measured using Living Image software with a region of interest around the body of each mouse. Only non-saturated images were used for quantification of BLI. Mice were randomized prior to T cell administration to ensure uniform distribution of tumor burden between groups. At the end of the experiment, all images were collected into a single sequence on Living Image and set to the same luminescence scale.

Nalm6 leukemia models

Six to ten-week old NSG male or female mice were implanted with $1x10^6$ N6-B7H3, N6-GL, or N6-ROR1 cells by tail vein injection. CAR specificity, treatment doses and times for the specific model, and drug doses are indicated in the figure legends. Tumor progression was monitored by firefly luciferase BLI. Mice were euthanized according to the criteria described in the Animal Models section.

MED8A subcutaneous tumor model

$0.5x10^6$ MED8A-GL cells were prepared in a 1:1 mixture of DPBS and Cultrex Basement Membrane Extract (R&D Systems) and injected into the right flank of six to ten-week old NSG male or female in a 200μL volume. Five days later, SNIP B7H3.BBz CAR-T cells or untransduced (Mock) T cells were administered by tail vein injection. T cell treatment and drug doses are indicated in the figure legends. Tumor progression was monitored by firefly luciferase BLI. Mice were euthanized according to the criteria described in the Animal Models section.

MED8A medulloblastoma tumor model

Mice were anaesthetized with 2% isoflurane (Minrad International) in an induction chamber and maintained during surgery on the stereotactic frame (David Kopf Instruments) delivered through a nose adaptor. $0.12x10^6$ MED8A-GL medulloblastoma cells were injected at coordinates 2 mm posterior to lambda on midline and 2 mm deep into 6- to 10-week-old NSG mice using a blunt-ended

Please cite this article in press as: Labanieh et al., Enhanced safety and efficacy of protease-regulated CAR-T cell receptors, Cell (2022), https://doi.org/10.1016/j.cell.2022.03.041

needle (75N, 26s/2″/2, 5 μL; Hamilton Co.). Using a microinjection pump (UMP-3; World Precision Instruments), MED8A-GL cells were injected in a volume of 3 μL at 30 nL/s. After leaving the needle in place for 1-2 minutes, it was retracted at 3 mm/min. Fourteen days after tumor implantation and after confirmation of tumor formation by bioluminescence, mice were randomized and treated with $3x10^6$ SNIP or constitutive B7H3.BBz CAR-T cells or an equivalent number of Mock T cells intravenously by tail vein injection. One group of mice that received SNIP B7H3 CAR-T cells were implanted with osmotic pumps containing 54 mg/mL GPV and 6 mg/mL RTV on Day 13 post-tumor implantation and administered 50 mg/kg GPV and 25mg/kg RTV by oral gavage 1-2 times per day (SNIP ON) or given no drug (SNIP OFF). Tumor progression was monitored by firefly luciferase BLI. Mice were euthanized according to the criteria described in the Animal Models section.

CHLA-255 neuroblastoma renal capsule tumor model

Mice were anaesthetized with 2.5% isoflurane in an induction chamber and maintained during surgery delivered through a nose adaptor on a heated surgical board. $1x10^6$ CHLA255-GL cells in 100μL DPBS were surgically implanted into the renal capsule using a 30 gauge needle. Seven days after tumor implantation and after confirmation of tumor formation by bioluminescence, mice were randomized and treated with $10x10^6$ SNIP or constitutive GD2.BBz CAR-T cells or an equivalent number of Mock T cells intravenously by tail vein injection. One group of mice that received SNIP GD2.BBz CAR-T cells were implanted with osmotic pumps containing 54 mg/mL GPV and 6 mg/mL RTV on Day 6 post-tumor implantation and administered 50 mg/kg GPV and 25mg/kg RTV by oral gavage 1-2 times per day (SNIP ON) or given no drug (SNIP OFF). Tumor progression was monitored by firefly luciferase BLI. Mice were euthanized according to the criteria described in the Animal Models section.

MG63.3 osteosarcoma tumor model

$1x10^6$ MG63.3 cells in 100μL DPBS were injected into the tibia periosteum. Eighteen days after tumor implantation and after visual confirmation of tumor formation, mice were treated with $10x10^6$ SNIP or constitutive HER2.BBz CAR-T cells or an equivalent number of Mock T cells intravenously by tail vein injection. One group of mice that received SNIP HER2.BBz CAR-T cells were implanted with osmotic pumps containing 54 mg/mL GPV and 6 mg/mL RTV on Day 17 post-tumor implantation and administered 50 mg/kg GPV and 25mg/kg RTV by oral gavage 1-2 times per day (SNIP ON) or given no drug (SNIP OFF). Tumor progression was measured with digital calipers twice per week. Mice were euthanized according to the criteria described in the Animal Models section.

143B osteosarcoma tumor model and T cells isolation from spleens and tumors

$1x10^6$ 143B cells in 100μL DPBS were injected into the tibia periosteum. Four days after tumor implantation and after visual confirmation of tumor formation, mice were treated with $5x10^6$ SNIP or constitutive HER2.BBz CAR-T cells or an equivalent number of Mock T cells intravenously by tail vein injection. Mice that received SNIP HER2.BBz CAR-T cells were implanted with osmotic pumps containing 54 mg/mL GPV and 6 mg/mL RTV on Day 4 post-tumor implantation and administered 50 mg/kg GPV and 25mg/kg RTV by oral gavage 2 times per day (SNIP ON). Spleens and tumors were harvested at Day 15 post tumor implantation. Tumors were mechanically dissociated using a gentleMACS dissociator (Miltenyi). Single-cell suspensions were made by passing tumors and spleens through a 70μm cell strainer, depleting red blood cells by ACK lysis (Quality Biological Inc.), and further filtration through flow cytometry filter tubes with 35μm cell strainer caps (Falcon). T cells were purified by magnetic separation using the REAlease® CD4/CD8 (TIL) MicroBead Kit (Miltenyi) according to the manufacturer's instructions.

Immunophenotyping and intracellular cytokine staining of splenic T cells and TILs

Immunophenotyping of splenic T cells and TILs was performed with fluorochrome-conjugated antibodies. Intracellular staining was performed after fixation and permeabilization of T cells (Intracellular Fixation & Permeabilization Buffer Set Kit, eBioscience). Before intracellular cytokine staining, $0.1x10^6$ T cells were activated with plate-bounded HER2 Fc (coated at 5μg/ml) in the presence of monensin (eBioscience) for 12hrs at 37°C. Cells were analyzed with BD LSRFortessa flow cytometer (BD Biosciences). Data analysis was performed with FlowJo Mac version 10.7.1 (Tree Star).

Proliferation assay

T cells were labeled with 5μM CTV (CellTrace Violet Cell Proliferation Kit, Invitrogen) at 37°C for 5 min followed by addition of ice-cold PBS 2% FBS to quench the reaction. Next, cells were washed and resuspended in complete RPMI 1640. $2x10^4$ cells were plated onto HER2 Fc-coated plate (coated at 5μg/ml). After 96hrs, CTV dilution was assessed by flow cytometry.

Single-cell analysis of CAR TILs

TILs from the 143B osteosarcoma model described above were purified from tumors 10 days after T cell administration using the REAlease® CD4/CD8 (TIL) MicroBead Kit (Miltenyi) according to the manufacturer's instructions and sent to the Stanford Functional Genomics facility for single-cell RNAseq library preparation using the Chromium Single Cell 3' Solution v3 platform (10x GENOMICS). Libraries were sent to Novogene for sequencing on a NovoSeq S4 lane (PE150) with >53,000 reads per cell. Reads were aligned and quantified with Cell Ranger (10x GENOMICS) using the standard workflow, with the exception that the reference transcriptome (GRCh38-and-mm10) was modified to include the 3' UTR and LTR of the MSGV1 vector, which allowed for gating on CAR^+ T cells. The Cell Ranger output was imported into R using the Seurat package. The following filters were applied using the subset function to select for live human single CAR-T cells: nFeature_RNA > 1500 & nFeature_RNA < 4200; percent mitochondrial reads < 12.5% & > 3.5%; percent mouse reads < 1.5%; percent CD3D > 0.01%; percent heat shock proteins < 0.75%, percent CAR reads > 0.005%, and percent mouse mitochondrial reads < 0.04%. The data matrix was scaled and transformed with the

Please cite this article in press as: Labanieh et al., Enhanced safety and efficacy of protease-regulated CAR-T cell receptors, Cell (2022), https://doi.org/10.1016/j.cell.2022.03.041

SCTransform pipeline (Hafemeister and Satija, 2019). Differential expression analysis, clustering, UMAP dimensionality reduction and cell-cycle analysis were performed on the resulting data matrix using the Seurat package (Hafemeister and Satija, 2019). We used the standard cell cycle scoring workflow based on genes from Tirosh et al. to categorize each cell based on a G2M and S gene expression score. Cells that do not express G2M or S genes are assumed non-cycling and were assigned to the G1 category (Tirosh et al., 2016).

CyTOF staining, normalization, and debarcoding

1-2 x10^6 cells were harvested from cell culture, washed 2x in PBS (10x stock, Rockland), and stained for viability with 250nM cisplatin (FLUIDIGM). The cisplatin reaction was quenched after a 3 minute incubation at room temperature with cell staining media (CSM, 1x PBS with.02% sodium azide and 0.05% BSA). Cells were centrifuged then resuspended in fixation solution containing 1.6% paraformaldehyde (PFA) for 10 minutes at room temperature. Subsequently, cells were centrifuged, resuspended in 150μL CryoStor, flash frozen, then stored at -80°C. For analysis, cells were thawed, washed in 5mL CSM, then barcoded and pooled with the Cell-ID™ 20-Plex Pd Barcoding Kit (FLUIDIGM) according to the manufacturer's instructions. CyTOF antibodies (see key resources table) were added to the barcoded sample, incubated on ice for 1 hr. Washed 3X with CSM, then resuspended in Ir-Intercalator (500μm iridium intercalator +1% PFA+ 1X PBS). Before acquisition cells were washed 1X with CSM and 3 times with ddH2O. After 2 water washes, cells were resuspended with 1x EQ™ Four Element Calibration Beads (FLUIDIGM) and acquired on a Helios mass cytometer (FLUIDIGM). After acquisition, data was normalized using MATLAB-based algorithm (Finck et al., 2013) and debarcoded using the MATLAB Single Cell Debarcoder tool.

CyTOF data analysis

Data collected in.fcs file format were analyzed on OMIQ platform (www.omiq.ai). To avoid debris and doublets, our gating scheme excluded calibration beads, aggregates using DNA signal and event length (Mei et al., 2015). We applied opt-SNE (Belkina et al., 2019) to each sample cohort, using 22 markers and the default settings for number iterations, perplexity and theta. We used equal subsampling of 6,500 events of total CAR+CD4+ or CD8+ T cells per sample. The following differentially expressed markers were used for opt-SNE: CD25, CD27, CD69, CD622L, CD45RO, OX-40, CD38, TIM3, TIGIT, Tbet, CTLA4, Foxp3, CD272, CD39, Lag3, CCR7, CD127, CD45RA, CD122, 41BB, and PD1.

Bulk RNAseq analysis of T cells

Constitutive or SNIP HER2.BBz, B7H3.BBz, and GD2.BBz CAR-T cell were manufactured from healthy donor T cells as described above. SNIP CAR-T cells were cultured in the absence of drug (SNIP OFF). RNA was extracted from Day 10 in vitro T cells using the RNeasy Plus Mini Kit (Qiagen) and send to NovoGene for library preparation, PE150 sequencing with a minimum of 6G raw output per sample, and demultiplexing. Reads were pseudo-aligned using Salmon (Patro et al., 2017). Differential gene expression analysis was performed with the R package DESeq2. All three CARs (HER2, B7H3, and GD2) were grouped for the analysis.

Gene set enrichment analysis (GSEA) was performed using the GSEA software (Broad Institute) as described (Mootha et al., 2003; Subramanian et al., 2005) using publicly available data sets GSE9650 and Good et al. (2021), GSEA analysis of HA GD2 exhausted CAR T cell signature was performed as previously described (Good et al., 2021) (PMID: 34861191) with slight modifications. We merged CD4 and CD8 populations and generated a signature of n=99 genes upregulated in HA-GD2 and a signature of n=101 genes upregulated in CD19 CAR expressing cells.

Analysis of ROR1 expression in human and mouse lung single-cell RNA-sequencing data

Single-cell RNA sequencing datasets for human lung (Travaglini et al., 2020), liver (MacParland et al., 2018), kidney (Stewart et al., 2019), and spleen (Madissoon et al., 2019) were downloaded as cell by gene counts tables. Mouse liver, kidney, and spleen smart-seq datasets were accessed from the Tabula Muris cell atlas (Tabula Muris Consortium et al., 2018) and the mouse lung data was accessed from the Raredon et al. dataset (Raredon et al., 2019). The cell by gene counts tables were processed using Scanpy v.1.4.3. Low quality cells were first excluded based on the following criteria: excluding cells with fewer than 250 genes, or 500 counts, or more than 25% mitochondrial reads. The remaining cells were depth-normalized to a total of 10,000 reads per cell. The depth-normalized gene expression values were then log-transformed with a pseudocount of 1. sc.pp.high_variable_genes was used to identify the top 2000 variable genes, and effects associated with the number of genes per cell were regressed out. Data was scaled with a max value of 10, and PCA was performed with default settings. Leiden clustering was performed to identify clusters of related cells. Gene expression values were visualized as log-transformed counts, using markers for known cell types identified from the literature. Violin plots were generated by sampling 500 cells from each dataset and plotting ROR1 expression for all cells and the cluster with the highest mean expression of ROR1.

ROR1 toxicity model

ROR1 CAR vectors were made as described in the viral vector construction section. Six to ten-week old NSG male or female mice were treated with the ROR1 CAR-T or mock T cells at the dose indicated in the figure legends by tail vein injection. To examine if radiation was required to induce toxicity, one group of mice that received ROR1(F).28z CAR-T cells was preconditioned with 2.2 Gy using a Kimtron IC-225 irradiator 5 hours prior to T cell administration. Mice in ROR1(F).28z and SNIP ROR1(F).28z ON (High GPV) groups experienced rapid onset of toxicity (within 24-48 hours) observed clinically as hunched posture,scruffy coat, slow movement, dehydration, and weight loss. Treatment-related toxicity was monitored by weight change, which was measured prior to T cell administration and 1-2x per week thereafter. %weight change was calculated according to $\%\ weight\ change = ((weight\ at\ time\ x)/(initial\ weight) - 1)x100$. Mice died from toxicity or were euthanized if they reached 20% weight loss or showed

Please cite this article in press as: Labanieh et al., Enhanced safety and efficacy of protease-regulated CAR-T cell receptors, Cell (2022), https://doi.org/10.1016/j.cell.2022.03.041

clinical signs of severe toxicity, as described in the Animal Models section. Mice treated with SNIP ROR1(F).28z CAR-T cells were administered GPV/RTV as indicated in the figure legends. For tumor-bearing ROR1 toxicity models, $1x10^6$ Nalm6-ROR1 leukemia cells were engrafted in NSG mice by tail vein injection 24 hours prior to T cell administration. The specific single cell clones used for in vivo experiments are C5 in Figures 7B–7D, and C1 and C3 for ROR1Low and ROR1Med, respectively, in Figures S7E and S7F. Tumor progression was monitored by firefly luciferase BLI.

Histological analysis of mouse tissues

Lungs and livers of CAR-T-treated mice were harvested, fixed by immersion in 10% neutral buffered formalin, routinely processed, embedded in paraffin, and stained with hematoxylin and eosin (H&E). Paraffin tissue blocks were sent to MD Biosciences (Oakdale, Minnesota) for CD3 immunohistochemistry. The assay was run on the Ventana Discovery Ultra. Slides were deparaffinized and then underwent retrieval at 95°C with CC1. Then Inhibitor CM was first applied followed by prediluted anti-CD3 antibody (clone 2GV6) for 24 minutes at 37°C. Chromogenic staining was generated via OmniMap anti-Rb HRP secondary application and Diaminobenzidine (DAB) reagents. Hematoxylin II and Bluing reagents were used for counterstaining. Slides were cover slipped with Leica Micromount Media.

QUANTIFICATION AND STATISTICAL ANALYSIS

For *in vivo* tumor-growth curves, significance was computed at the indicated timepoint on the plot by unpaired two-tailed t test comparing the constitutive group with the SNIP ON group. Significance for survival data was calculated using the log-rank Mantel–Cox test. Statistical analysis on flow cytometry quantification was computed by unpaired two-tailed t test comparing the indicated groups, unless otherwise indicated. All statistical tests were performed on GraphPad Prism 8. Asterisks denoting statistical significance are in Graphpad Prism style with one, two, three, or four asterisks representing P values less than 0.05, 0.01, 0.001, and 0.0001, respectively.

CellPress
OPEN ACCESS

Supplemental figures

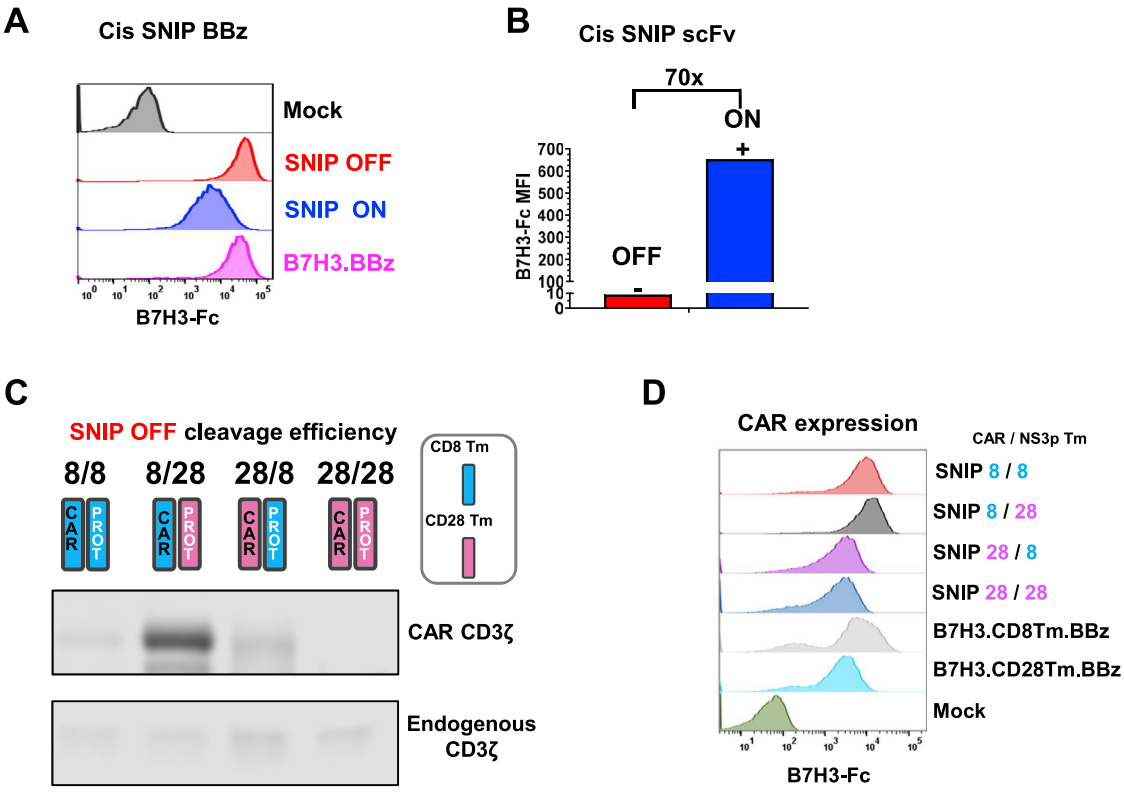

(legend on next page)

Figure S1. Characterization of anti-B7H3 SNIP CAR-T cells, related to Figure 1

(A and B) Flow cytometry of surface B7H3 CAR by staining with 3 μg/mL B7H3-Fc on day 10 (A) *cis* SNIP BBz and (B) *cis* SNIP scFv CAR-T cells ±3 μM GPV.

(C) CAR-CD3ζ immunoblots of protein lysates from anti-B7H3 SNIP BBz CAR-T cells with various combinations of CD8α and CD28 Tm for the CAR and protease modules in the absence of drug (SNIP OFF) demonstrates that the matched 8/8 and 28/28 Tm configurations result in efficient cleavage of CAR molecules. The image was cropped to exclude nonrelevant gel lanes.

(D) B7H3 CAR expression of D10 *trans* SNIP BBz CAR-T cells with various transmembrane domains stained with 3 μg/mL B7H3-Fc. SNIP groups were incubated with 1 μM GPV for 96 h.

(E) Quantification of surface expression of B7H3 CAR on D10 T cells stained with 3 μg/mL B7H3-Fc. SNIP ON groups were incubated with 1 μM GPV for 24 h. Data are mean ± SEM from three different donors. p values were determined by unpaired two-tailed t tests, ns $p > 0.05$.

(F) Cytokine secretion of day 14 anti-B7H3 SNIP CAR-T cells against GFP-labeled N6-B7H3 leukemia cells at a 1:1 effector:target ratio incubated in (left panel, ON kinetics) or washed out of (right panel, OFF kinetics) 3 μM GPV for the indicated amount of time prior to the coculture. GPV was included in the coculture period for ON kinetics and excluded from the coculture period for OFF kinetics. For OFF kinetics, GPV was added at day 10 then removed for the indicated amount of time prior to the coculture. Coculture supernatant was harvested after 24 h and was then analyzed for IFNγ and IL-2 by ELISA. Mock, no drug, and B7H3.BBz are shared controls and duplicated between the ON and OFF kinetics (also in Figure 1G). Data are mean ± SEM.

In (A), B7H3.BBz and Mock are shared controls for CAR expression and duplicated in the plot in Figure 1B. In (B), median fluorescence intensities (MFIs) were calculated from the data on Figure 1B. In (A) and (B), CAR expression was measured on day 10 B7H3 CAR-T cells in the presence (SNIP ON) or absence (SNIP OFF) of 3 μM GPV for 96 h. In (A)–(D) and (F), reproducible in two independent experiments with different donors.

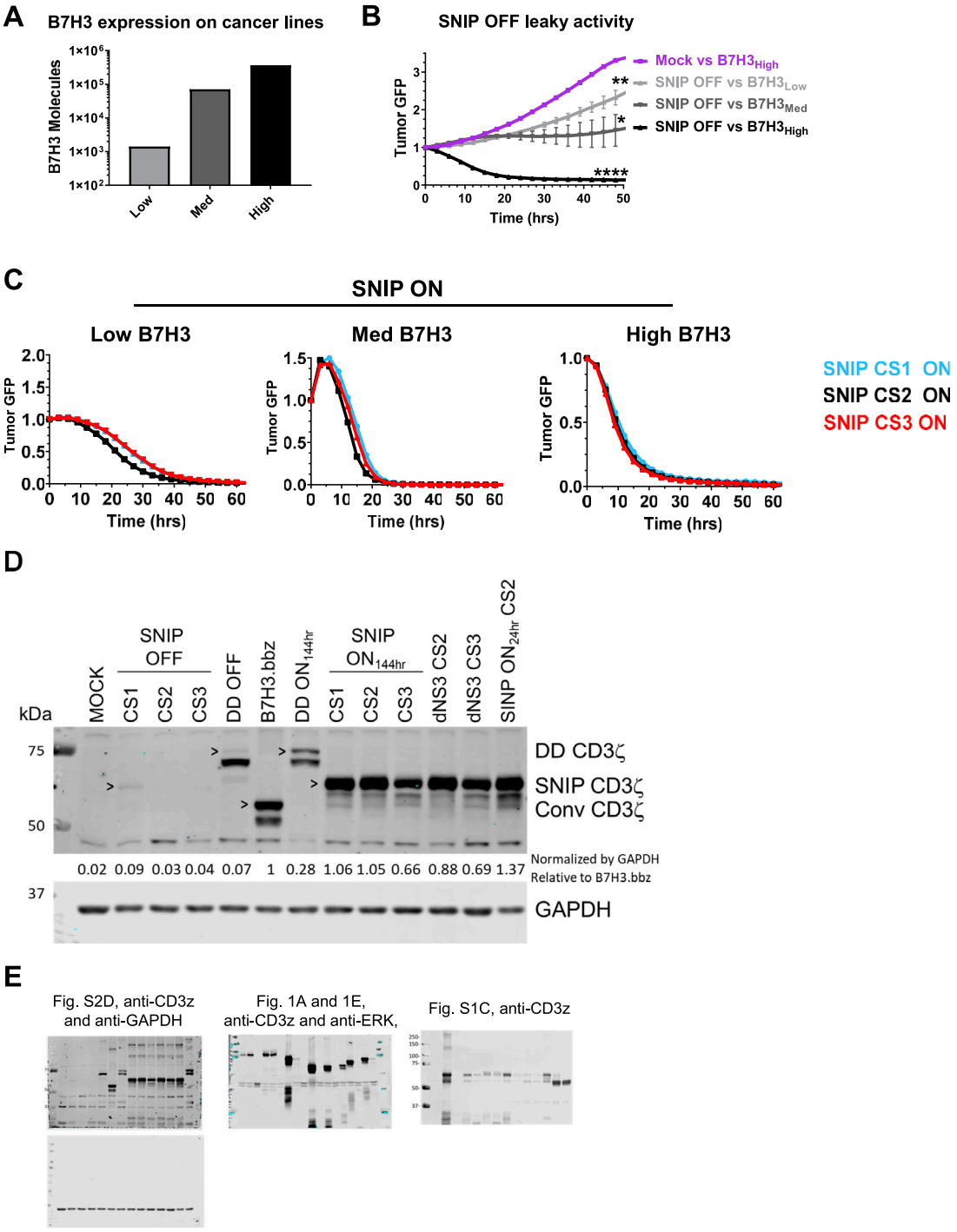

Figure S2. Evaluation of substituted SNIP cleavage sites against tumor lines with various antigen densities, related to Figure 2

(A) Surface B7H3 expression on low, medium, and high B7H3-expressing cancer lines, as determined by staining with 3 μg/mL anti-B7H3 antibody and flow cytometric analysis. Quantification of B7H3 surface molecules was performed using the Quantum Simply Cellular quantification kit.

(B) Leaky cytotoxic activity of SNIP B7H3.BBz CAR-T cells is increased with higher antigen density on target lines. Data are mean ± SEM. Statistical significance was computed by comparing each SNIP OFF against Mock at the final time point by unpaired two-tailed t tests, *$p \leq 0.05$, **$p \leq 0.01$, ****$p \leq 0.0001$.

(C) Substituted SNIP cleavage sites maintain antitumor activity in the ON state. Experiments were setup as in Figure 2E, but CAR-T cells were incubated with 3 μM GPV 24 h prior to and during the coculture. Data are mean ± SEM.

(D) CAR-CD3ζ immunoblots of protein lysates from various day 10 B7H3.BBz CAR-T cells. SNIP and DD ON groups were incubated in 1 μM GPV or TMP, respectively, for the indicated amount of time. dNS3, CS, and Conv indicate SNIP dead NS3 protease control, cleavage site, and conventional B7H3.BBz CAR,

(legend continued on next page)

respectively. GAPDH serves as a loading control. Quantification of western blot bands was performed by densitometric analysis and is indicated below the blot. The samples were normalized to GAPDH then expressed relative to the conventional CAR control. The image was cropped to exclude nonrelevant gel lanes. (E) Uncropped immunoblot gels shown in this study.

In (A)–(C), low, med, and high B7H3 indicate N6-B7H3, D425, and N6-B7H3$_{Hi}$ tumor lines, respectively. Data are mean ± SEM of triplicate wells. In (A)–(C), reproducible in three independent experiments with different donors.

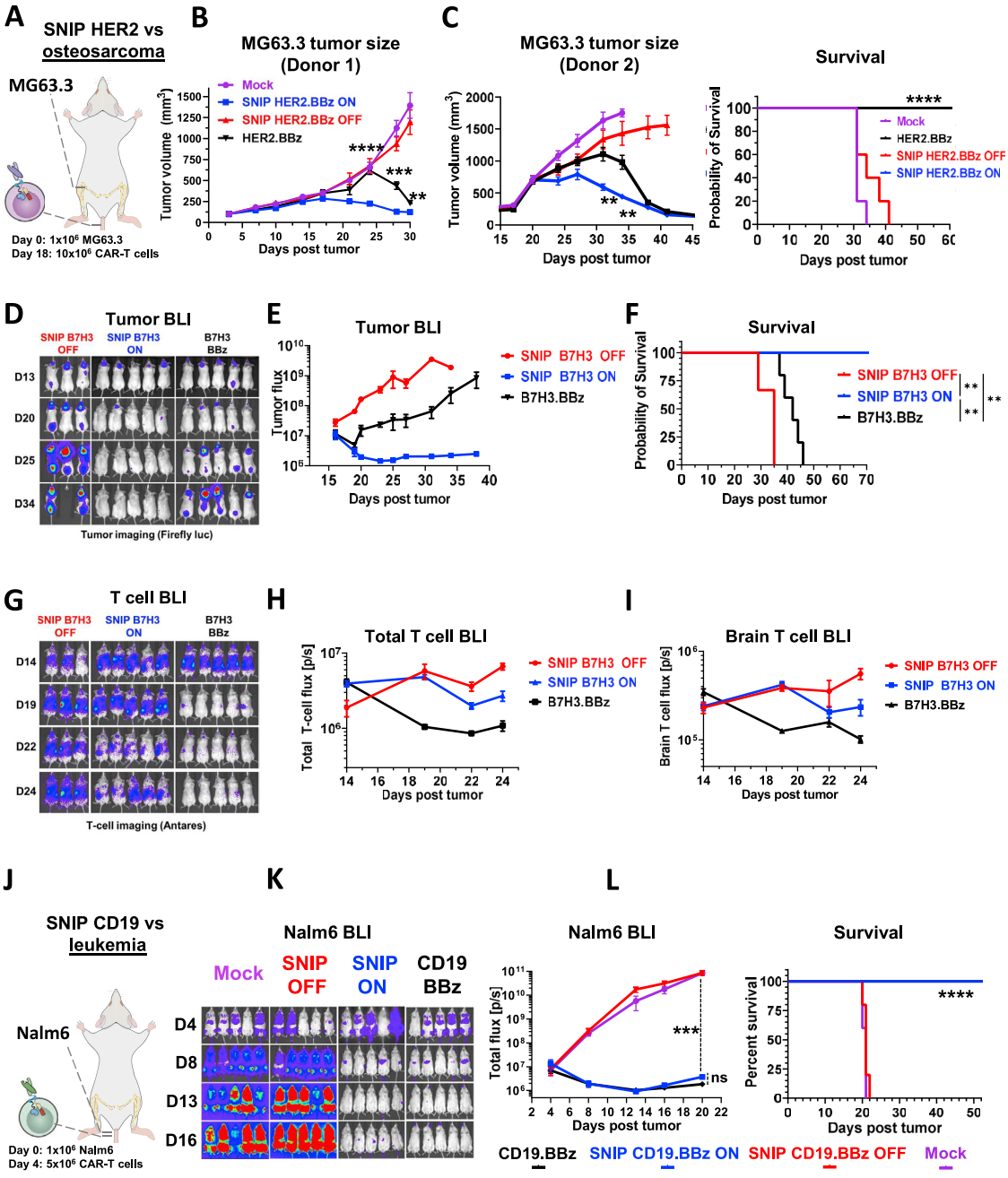

Figure S3. Activity and expansion of SNIP CAR-T cells *in vivo*, related to Figure 3

(A) Schematic of the MG63.3 osteosarcoma tumor model using HER2-specific CARs.

(B and C) Tumor progression in the 143B osteosarcoma was monitored by tumor volume measurements for (B) donor 1 and (C) donor 2 (left) and survival curves in the 143B model from donor 2 (right).

(D) NSG mice were injected with 0.12 × 10^6 MED8A cells in the cerebellum and were then treated with 8 × 10^6 SNIP B7H3.BBz CAR or Mock T cells 14 days later via tail vein injection. Tumor progression of MED8A was monitored by firefly luciferase BLI.

(E) Quantification of MED8A medulloblastoma BLI.

(F) Survival curves of mice in the MED8A medulloblastoma model.

(G) T cell expansion was monitored by Antares BLI.

(H) Quantification of T cell Antares BLI on the whole mouse.

(I) Quantification of T cell Antares BLI on a region of interest around the head of the mouse.

(J) Schematic of the CD19 Nalm6 leukemia model. 1 × 10^6 Nalm6 leukemia cells were engrafted by tail vein of NSG mice. 4 days later, 5 × 10^6 SNIP CD19 CAR, constitutive CD19.BBz CAR, or untransduced (Mock) T cells were administered by tail vein injection.

(legend continued on next page)

(K) Tumor progression was monitored by bioluminescence imaging. All images were set to the same scale.
(L) Quantification of CD19 leukemia bioluminescence imaging (left) and survival curves of mice in the Nalm6 leukemia model (right). BLI quantification data are mean ± SEM of n = 5 mice in each group. p values were determined by unpaired two-tailed t tests at the final time point. Survival curves were compared by the log-rank Mantel-Cox test. Reproducible in two independent experiments with different donors.
In (A)–(L), mice that received SNIP ON CAR-T cells were implanted with osmotic pumps containing 54 mg/mL GPV and 6 mg/mL RTV and administered 50 mg/kg GPV + 25 mg/kg RTV by oral gavage 2 times per day in (A)–(I) and 1−2 per day in (J)–(L), whereas mice that received SNIP OFF CAR-T cells were not administered GPV. All CAR-T cells were manufactured for 10 days in the absence of GPV. Data are mean ± SEM. Survival curves were compared by the log-rank Mantel-Cox test. Statistical analysis of tumor burden was performed at the indicated time point by unpaired two-tailed t tests, ns $p > 0.05$, ** $p \leq 0.01$, *** $p \leq 0.001$, **** $p \leq 0.0001$.

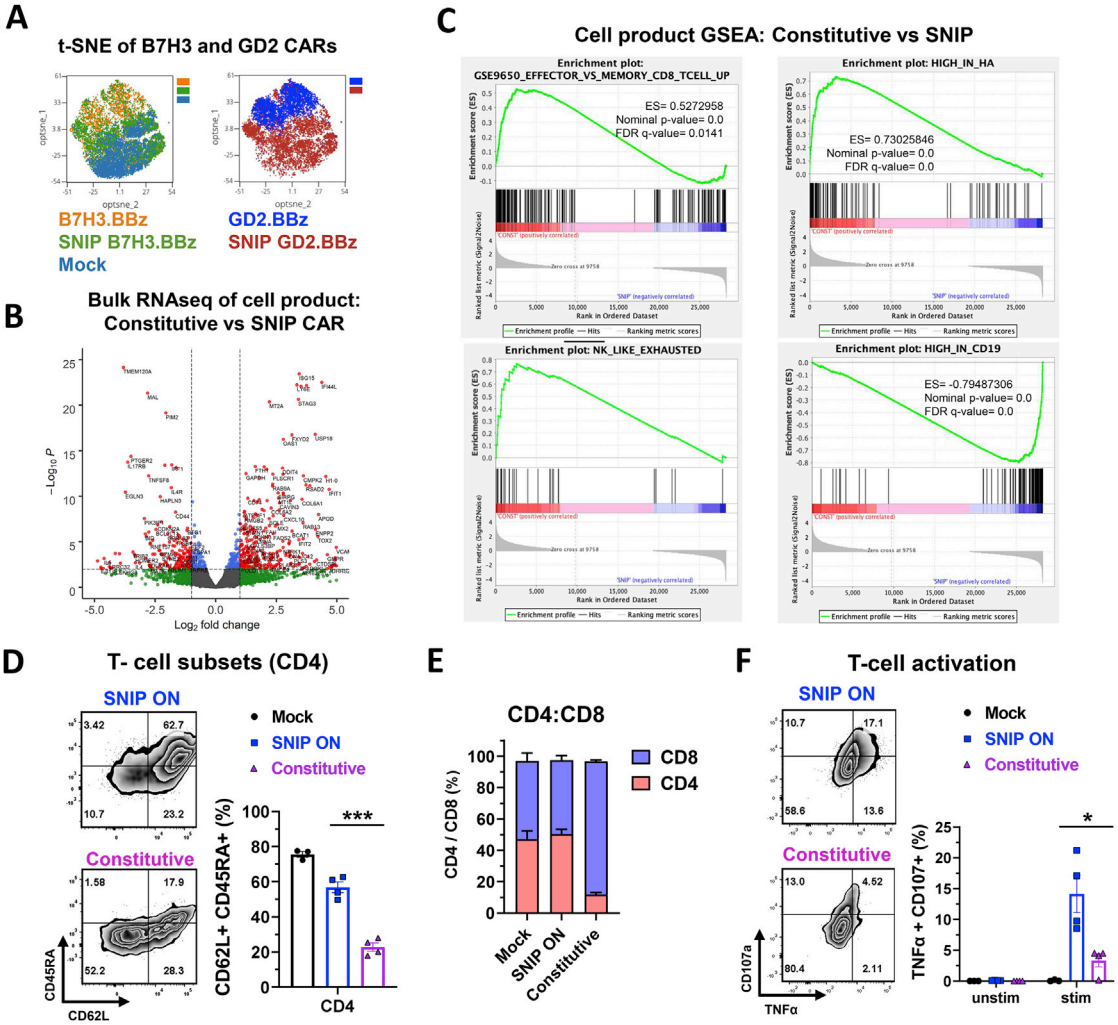

Figure S4. SNIP CAR-T cells have distinct RNA and protein expression profiles during the *in vitro* expansion period and increased functionality *ex vivo*, related to Figure 4

(A) Mass cytometry and tSNE analysis, run together with samples in Figure 4A, of B7H3 and GD2 CAR-T cells demonstrates differential clustering and colocalization of SNIP CAR with Mock T cells compared with constitutive CARs.

(B) Volcano plot from differential gene expression analysis comparing constitutive CAR with SNIP CAR-T cells.

(C) GSEA analysis of unstimulated constitutive and SNIP RNA-seq samples with genes upregulated in effector versus memory T cells (top left, GSE9650 [Wherry et al., 2007]), an exhaustion signature from Good et al. (2021) (bottom left), genes upregulated in HA-GD2 (top right) and CD19 (bottom left) CAR-T cells from Lynn et al. (2019).

(D) Representative flow plots showing surface expression of CD45RA and CD62L on splenic $CD4^+$ HER2 CAR-T cells that distinguish T memory stem cells (T_{SCM}, $CD45RA^+$ $CD62L^+$), central memory cells ($CD45RA^-$ $CD62L^+$), and effector memory cells ($CD45RA^-$ $CD62L^-$) (left), and quantification of T_{SCM} subsets on splenic CAR-T cells reveals an increased proportion of SNIP CAR-T compared with constitutive CAR-T cells (right).

(E) Increased $CD4^+$:$CD8^+$ ratio in SNIP versus constitutive splenic CAR-T cells.

(F) Intracellular cytokine staining of TNFα and CD107a of stimulated splenic CAR-T cells demonstrates enhanced cytokine secretion of SNIP CAR-T cells.

In (A)–(C), constitutive and SNIP HER2.BBz, B7H.BBz, and GD2.BBz CAR-T cells were harvested at day 10 postbead activation for RNA-seq and CyTOF analysis. SNIP CAR-T cells were cultured in the absence of drug (SNIP OFF). In (D)–(F), flow cytometry dot plots are of representative mice. Bar graph data are mean of individual mice ± SEM of each group. p values were determined by unpaired two-tailed t tests, *$p \leq 0.05$, ***$p \leq 0.001$. In (E), statistical significance was determined by comparing %CD8 of the SNIP ON and constitutive groups.

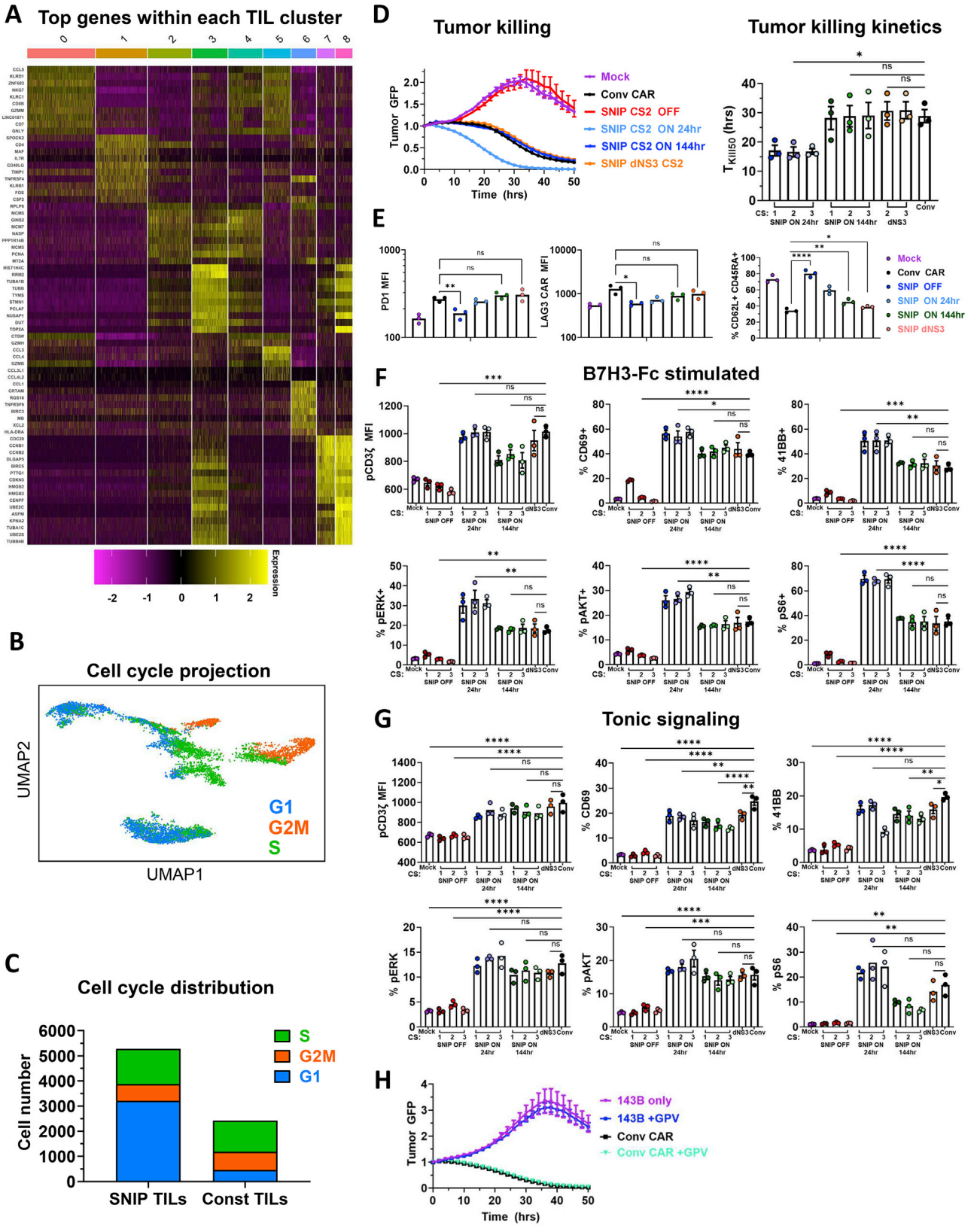

(legend on next page)

Figure S5. Phenotypic and functional attributes of SNIP CAR-T cells, related to Figures 4 and 5

(A) Single-cell heatmap showing the top 10 genes of each cluster in Figure 5A.

(B) Cell cycle analysis of single cells overlaid on UMAP plot.

(C) Distribution of cells among S, G2M, and G1 phase of the cell cycle. A greater proportion of cells in G1 phase were found in SNIP CAR-T compared with constitutive CAR-T cells. Cell cycle analysis was performed using the CellCycleScoring function of the Seurat package.

(D) Tumor killing curves of various D10 B7H3.BBz CAR-T cells cultured with GFP-labeled 143B osteosarcoma cells (left) and quantification of the T_{Kill50} parameter or the time point at which the GFP signal reaches less than 50% (right). T_{Kill50} data are mean ± SEM of three donors. p values determined by unpaired two-tailed t tests for CS2 constructs, ns $p > 0.05$, *$p \leq 0.05$.

(E) Quantification of PD1 MFI, LAG3 MFI, and %CD62L+CD45RA on D10 B7H3.BBz CAR-T cells. Data are mean ± SEM of three donors. p values determined by unpaired two-tailed t tests, ns $p > 0.05$, *$p \leq 0.05$, **$p \leq 0.01$, ****$p \leq 0.0001$.

(F) Quantification of expression of various phosphomarkers and activation markers from D10 B7H3.BBzCAR-T cells stimulated with 3 μg/mL plate bound B7H3-Fc for 16 h. Data are mean ± SEM of three donors. p values were determined by ordinary one-way ANOVA comparing CS2 samples with conventional CAR, ns $p > 0.05$, *$p \leq 0.05$, **$p \leq 0.01$, ***$p \leq 0.001$, ****$p \leq 0.0001$. Phosphorylation of proteins downstream of the CAR revealed no significant differences between SNIP ON 144 h or dNS3 compared with constitutive B7H3.BBz CAR-T cells, whereas we observed a marked increase of %CD69+, %41BB+, %pERK+, pAKT+, and % pS6 on rested SNIP (ON 24 h) CAR-T cells.

(G) The same analysis as in (F) without B7H3-Fc stimulation.

(H) Proliferation of 143B cells under the indicated conditions. +GPV indicates incubation with 3 μM GPV. Representative plot shown, reproducible in three different donors. In (D)–(G), SNIP ON groups were incubated in 1 μM GPV for the indicated amount of time. dNS3, CS, and Conv indicate SNIP dead NS3 protease control, cleavage site, and conventional B7H3.BBz CAR, respectively. Data are mean ± SEM from three donors. In (F) and (G), Mock is a shared control and duplicated between corresponding plots.

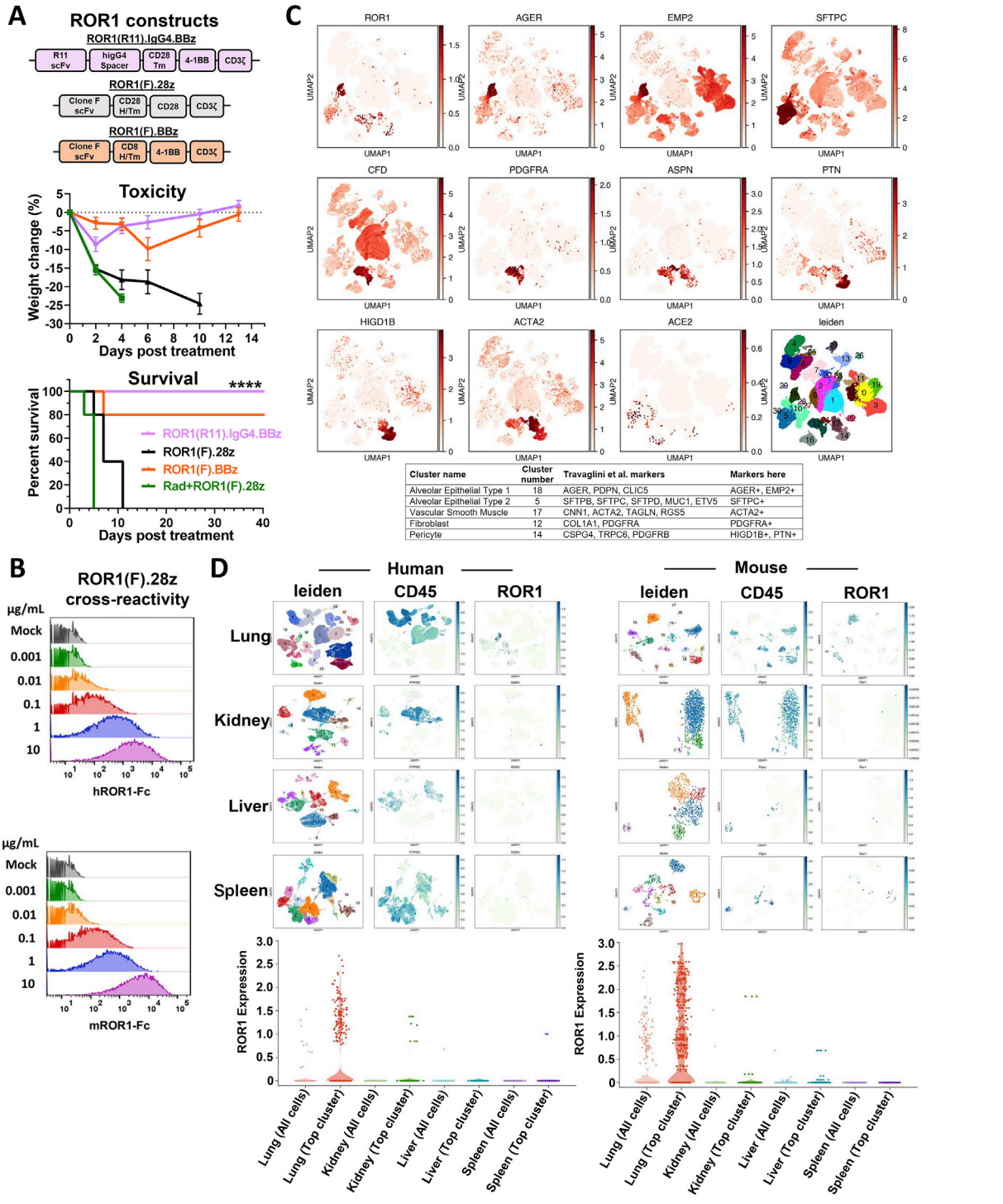

Figure S6. Clone F-based ROR1.28z CAR-T cells induce lethal on-target off-tumor toxicity in mice without preconditioning and identification of ROR1 expression in human and mouse scRNA-seq data sets, related to Figure 6

(A) Schematic of ROR1 CAR constructs (top). Nontumor-bearing NSG mice were engrafted with 8×10^6 ROR1 CAR-T cells. One group of mice that received ROR1(F).28z CAR-T cells were preconditioned by irradiation (Rad) with 2.2 Gy 5 h prior to T cell administration. Treatment-related toxicity was monitored by weight change (middle). Survival curves for nontumor-bearing mice treated with ROR1 CAR-T cells (bottom). Mice treated with ROR1(F).28z CAR-T cells exhibited rapid weight loss and succumbed to toxicity without preconditioning. Weight change data are mean ± SEM of n = 5 mice in each group. Survival curves were compared by the log-rank Mantel-Cox test, ****$p \leq 0.0001$.

(B) Staining of ROR1(F).28z CAR-T cells with human and mouse ROR1-Fc at the indicated concentration.

(legend continued on next page)

(C) Human lung single-cell data set from Travaglini et al. showing ROR1 expression most prominently on alveolar type I cells (AGER+ and EMP2+) and to a lesser extent alveolar type II cells (SFTPC+), adventitial fibroblasts and alveolar fibroblasts (PDGFRA+), pericytes (HIGD1B+ and PTN+), and vascular smooth muscle cells (ACTA2 high). Markers used to identify cells are indicated below the UMAP plot (Travaglini et al., 2020).
(D) Human (left) and mouse (right) ROR1 expression analyzed from single-cell RNA data sets. Violin plots (bottom) were generated by sampling 500 cells within each data set and plotting ROR1 expression for all cells and the cluster with the highest mean expression of ROR1. This analysis revealed that the lungs are the most prominent site of ROR1 expression in these data sets.
See STAR Methods for further details.

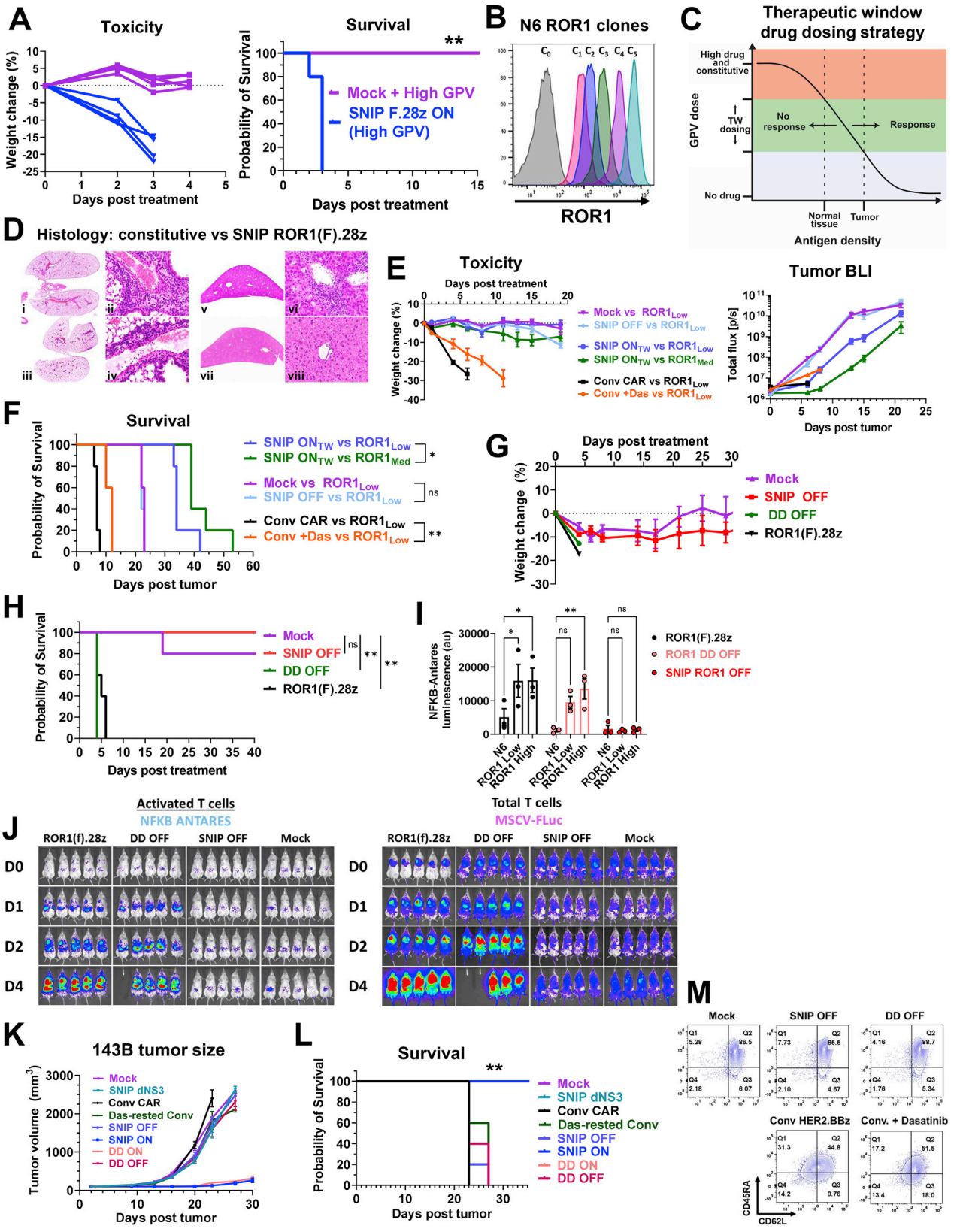

(legend on next page)

Figure S7. Lethal toxicity is induced with high GPV dosing but averted with modified drug dosing in mice treated with SNIP ROR1(F).28z CAR-T cells and comparison of SNIP with other drug-regulated CAR systems, related to Figure 7

(A) 1 × 10^6 Nalm6-ROR1 leukemia cells were engrafted in NSG mice by tail vein injection. 1 day later, 10 × 10^6 SNIP ROR1(F).28z CAR or Mock T cells were administered by tail vein injection. Mice in the SNIP group were implanted with osmotic pumps containing 54 mg/mL GPV and 6 mg/mL RTV. All mice were administered 50 mg/kg GPV and 25 mg/kg RTV by oral gavage 3 times per day (high GPV). Treatment-related toxicity was monitored by weight change (left), which shows that SNIP ROR1(F).28z CAR-T cells induce rapid onset toxicity, comparable with constitutive ROR1(F).28z CAR-T cells (see Figure 7B) with high GPV dosing. Survival curves were compared by the log-rank Mantel-Cox test (right).

(B) ROR1 surface expression of Nalm6-ROR1 single-cell clones stained with 3 μg/mL Clone F antibody.

(C) Schematic of the therapeutic window (TW) drug dosing strategy to selectively target tumor cells while sparing healthy tissue. The black curve represents the threshold for activity (i.e., given a specific level of GPV, antigen density needs to the right of the threshold for activity). At the depicted antigen densities for normal and tumor tissue, the orange region denotes an "effective" but toxic regimen, the green region denotes a safe and effective regimen, and the gray region denotes a nontoxic, noneffective regimen.

(D) Histological analysis of organs from mice in the therapeutic window experiment in Figure 7. Lungs (Di–Div) and livers (Dv–Dviii) from ROR1(F).28z (Di, Dii, Dv, and Dvi) and SNIP ROR1(F).28z ON_{TW} (Diii, Div, Dvii, and Dviii) CAR-T cell-treated animals were harvested, fixed by immersion in 10% neutral buffered formalin, routinely processed, embedded in paraffin, and stained with hematoxylin and eosin (H&E). In the lungs of ROR1(F).28z CAR-T cell-treated animals (Di and Dii), there were dense cellular cuffs surrounding blood vessels and bronchioles, but these were less prominent in SNIP ROR1(F).28z ON_{TW} CAR-T cell-treated animals (Diii and Div). Similarly, the livers of ROR1(F).28z CAR-T cell-treated animals (Dv and Dvi) had dense cellular aggregates around portal regions and surrounding bile ducts, as well as areas of tissue necrosis, whereas the livers of SNIP ROR1(F).28z ON_{TW} CAR-T cell-treated animals (Dvii and Dviii) had no obvious tissue pathology. Hematoxylin and eosin (H&E) stained sections. Magnification: Di and Diii = 1.25×; Dv and Dvii = 2×; Dii, Div, Dvi, and Dviii = 40×.

(E) 1 × 10^6 Nalm6-$ROR1_{Low}$ or $ROR1_{High}$ leukemia cells were engrafted in NSG mice by tail vein injection. 1 day later, 10 × 10^6 SNIP CAR, conventional ROR1(F).28z CAR, or Mock T cells were administered by tail vein injection. Mice in the SNIP ON_{TW} group were given 25 mg/kg GPV and 2.5 mg/kg RTV by oral gavage once per day. Mice in the +Das group were given 50 mg/kg dasatinib twice per day by oral gavage. Treatment-related toxicities were monitored by weight change (left). Tumor progression was monitored by bioluminescence imaging (right). Data are mean ± SEM.

(F) Survival curves for the mice in (E).

(G) Nontumor-bearing mice were irradiated with 2.2 Gy and then infused with 10 × 10^6 CAR-T cells by tail vein injection. SNIP- and DD CAR-T-treated mice were not dosed with GPV or TMP (i.e., OFF state). Treatment-related toxicities were monitored by weight change. Data are mean ± SEM.

(H) Survival curves for the mice in (G).

(I) Antares induction after simulation with Nalm6 ROR1+ or ROR1− cell lines. Antares bioluminescence was detected 16 h later using the NanoGlo substrate. Data are mean ± SEM of three donors. p values determined by unpaired two-tailed t tests, ns $p > 0.05$, *$p \leq 0.05$, **$p \leq 0.01$.

(J) Activated T cells (left) were monitored using the NF-κB-Antares reporter. Total T cells (right) were monitored using a constitutively expressed firefly luciferase.

(K) NSG mice were injected with 1 × 10^6 143B cells in the tibia periosteum and were then treated with 4 × 10^6 of the indicated HER2.BBz CAR-T cells 4 days later. Tumor progression was monitored by volume measurements. All SNIP and DD cells were manufactured in the absence of GPV or TMP (OFF state). After infusion into mice, SNIP ON and DD ON were implanted with osmotic pumps (see STAR Methods) and dosed with SNIP drug (50 mg/kg GPV + 25 mg/kg RTV) and DD drug (50 mg/kg TMP), respectively, 2 times per day by oral gavage. Mice in the Das-rested Conv. group were treated with conventional HER2.BBz CAR-T cells manufactured in the presence of 1 μM dasatinib (OFF state) beginning at day 5 postactivation and were not given additional drug after infusion into mice. Data are mean ± SEM.

(L) Survival curves of mice in (K).

(M) Flow plots from day 10 preinfusion HER2.BBz CAR-T cells used in (K) and (L) showing expressions of CD45RA and CD62L. Reproducible in three independent experiments using different donors.

In (A), (F), (H), and (L), survival curves were compared by the log-rank Mantel-Cox test, ns $p > 0.05$, *$p \leq 0.05$, **$p \leq 0.01$.